

MACKAY SCHOOL OF MINES  
UNIVERSITY OF NEVADA, RENO

✓  
Reconnaissance Geologic Mapping of a Heavily-Forested  
Shield Area (Guiana Shield, Northwestern Brazil)

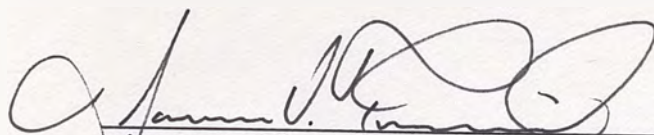
A dissertation submitted to the faculty of the  
Department of Geological Sciences, in partial  
fulfillment of the requirements for the degree of  
Doctor of Philosophy in Geophysics.

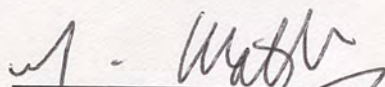
by

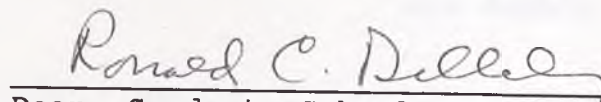
Fernando Pellon de Miranda

|||  
November, 1990

The dissertation of Fernando Pellon de Miranda is approved:

  
Dissertation Advisor

  
Department Chair

  
Dean, Graduate School

University of Nevada, Reno

November 1990

© 1990

Fernando Pellon de Miranda

All Rights Reserved

## ACKNOWLEDGMENTS

I would like to acknowledge and thank my advisory-committee members, Dr. James T. Yarnall, Chairman, Dr. James A. Carr, Dr. David A. Hunt, Dr. Christopher B. Elvidge, Dr. Lawrence F. Larson, and Dr. Paul F. Swiler, for all the assistance and guidance they have given me during my stay at the Mackay School of Mines. Dr. John B. Ford (SRI) kindly provided the SIR-2 digital image used for this study. The meteorologic data were graciously provided by Dr. Eduardo M. Villacelme (CERN). Ross E. McChaffer and Dr. Lindrich Gabel contributed their knowledge during the atmospheric data processing and gave me access to software and computer facilities.

This dissertation is dedicated to Lili Rose.

John A. MacDonnell shared with me the meteorological data and the meteorological classifier (MTC) software and made excellent suggestions during the processing of SIR-2 data. I am also grateful to Charles Sabine, Dr. Nancy M. Milton, and William R. Ayers for their valuable cooperation during the dissertation process. Many colleagues from Brazil were always instrumental in sending me data from the study area: Dr. Wang Hong Xiang, Claudio Corina de Lima, Francisco M. S. de Souza, Ana Maria P. Mizutaki, and Dr. Marco Polo P. de Vas Faria (all from Petropolis), Dr. Celso C. C. Tassinari (IBR), and Dr. Renato Schneider Santos (CERN). Candace Barnett was of great help typing and proofing the final

## ACKNOWLEDGEMENTS

I would like to acknowledge and thank my Advisory-Examining Committee, Dr. James V. Taranik, Chairman, Dr. James R. Carr, Dr. David A. Mouat, Dr. Christopher D. Elvidge, Dr. Lawrence T. Larson, and Dr. Paul T. Tueller, for all the assistance and guidance they have given me during my stay at the Mackay School of Mines. Dr. John P. Ford (JPL) kindly provided the SIR-B digital image used for this study. The aeromagnetic data were graciously provided by Dr. Ricardo M. Vasconcellos (CPRM). Anne E. McCafferty and Dr. Lindrith Cordell contributed their knowledge during the aeromagnetic data processing and gave me access to software and computer facilities at the USGS Branch of Geophysics, Denver. John A. MacDonald shared with me the semivariogram textural classifier (STC) software and made excellent suggestions during the processing of SIR-B data. I am also grateful to Charles Sabine, Dr. Nancy M. Milton, and William H. Aymard for their valuable cooperation during the dissertation process. Many colleagues from Brazil were always instrumental in sending me data from the study area: Dr. Chang Hung Kiang, Claudio Coelho de Lima, Francisco M. B. da Cunha, Ana Maria P. Misuzaki, and Dr. Marco Polo P. da Boa Hora (all from Petrobras), Dr. Colombo C. G. Tassinari (USP), and Dr. Orestes Schneider Santos (CPRM). Candace Bennett was of great help typing and proofing the final

draft. This research was fully supported by Petrobras (Petroleo Brasileiro S/A). I am extremely grateful for such an opportunity of professional advancement.

## ABSTRACT

The part of the Guiana Shield situated in northwestern Brazil is one of the least geologically known regions of the country. It is characterized by a complex association of gneissic and granitoid rocks of middle Proterozoic age (Guianense Complex), which are not individually recognized as distinct units in the geologic map published by the RADAMBRASIL Project at 1:1,000,000 scale. The area is completely covered by rainforest. Lithologic contacts and geologic structures have no obvious geomorphic expression.

In 1984, the Shuttle Imaging Radar-B (SIR-B) acquired digital data over the Guiana Shield. This L-band, HH polarization synthetic aperture radar system operated at a fixed incidence angle of 35.7 degrees on flat terrain. The semivariogram textural classifier (STC) was employed to discriminate and map flooded vegetation and water, which were considered the key cover types for the recognition of subtle topographic relief (up to 8.0 meters) in the study area. Linearly arranged floodplains were interpreted as linear geomorphic features. In addition, tonal linear features were identified on the SIR-B image using a contrast stretching technique (trackball linear mapping; TLM). A final map was developed including both STC-mapped and TLM-enhanced linear features, in order to display landscape

patterns indicative of subtle structural discontinuities in the crystalline terranes of the Guiana Shield.

The digital aeromagnetic data used in this research were obtained in 1987. Measurements were made using a proton-precession magnetometer with sensitivity of 1.0 nanoTesla (nT). Flight-lines were flown north-south at a 2.0-km spacing; tie-lines were flown east-west at a 20.0-km spacing. The survey was performed in a draped mode 150 m above relatively flat terrain. The following products were derived as a result of digital data manipulation: (1) a grey-scale image of the reduced-to-pole magnetic anomalies, in order to highlight zones of distinct magnetic signature; (2) a terrace-magnetization map that delineates induced magnetization boundaries and theoretically outlines geologic structures and varying magnetic terranes; (3) a map showing the location of maximum values of the horizontal component of the pseudogravity gradient (boundary lines) that represent abrupt lateral changes in magnetization that are interpreted as steep structural or lithologic contacts.

Comparison of the magnetic and remote sensing results with the geologic data acquired in the field by the RADAMBRASIL Project allowed broad terrane categories in the study site to be delineated for the first time: (1) areas characterized by intermediate brightness levels on the grey-scale magnetic image and by low to intermediate



magnetization values on the terrace map ( $-0.00018 \text{ emu.cm}^{-3}$  to  $0.00090 \text{ emu.cm}^{-3}$ ) correspond to migmatites and metamorphic rocks devoid of muscovite with Rb-Sr radiometric age of  $1640 \pm 26 \text{ m.y.}$  and mantle derivation ( $I.R. = 0.703 \pm 0.001$ ); (2) areas characterized by very bright signatures on the grey-scale magnetic image and by high terrace-magnetization values (greater than  $0.00090 \text{ emu.cm}^{-3}$ ) correspond to granitoids devoid of muscovite of unknown age cutting the mantle-derived migmatites and metamorphic rocks. Geologic faults with both topographic and magnetic expression were identified in the study area through the comparison of SIR-B linear features, terrace map, and magnetization boundary lines.

## TABLE OF CONTENTS

	<u>Page</u>
CHAPTER I. INTRODUCTION AND OBJECTIVES . . . . .	1
STATEMENT OF PROBLEM . . . . .	1
GENERAL EXPERIMENTAL APPROACH . . . . .	4
MAJOR SCIENCE QUESTIONS ADDRESSED . . . . .	5
STUDY AREA . . . . .	7
RATIONALE FOR SELECTION . . . . .	7
CLIMATE . . . . .	9
PEDOLOGY . . . . .	10
VEGETATION . . . . .	12
GEOMORPHOLOGY . . . . .	15
CHAPTER II. PREVIOUS GEOLOGIC INFORMATION . . . . .	18
GEOTECTONIC OUTLINE OF THE AMAZONIAN CRATON . . . . .	18
REGIONAL GEOLOGY OF NORTHWESTERN BRAZIL . . . . .	22
GEOLOGIC INFORMATION AVAILABLE IN THE STUDY AREA . . . . .	26
CHAPTER III. METHODOLOGY . . . . .	34
REVIEW OF PREVIOUS GEOLOGIC INTERPRETATIONS OF SPACEBORNE RADAR IMAGES IN HEAVILY-FORESTED REGIONS . . . . .	34
SEASAT . . . . .	35
SHUTTLE IMAGING RADAR . . . . .	36

## TABLE OF CONTENTS

	<u>Page</u>
VEGETATION DISCRIMINATION IN SPACEBORNE RADAR IMAGES OF RAINFOREST AREAS USING THE SEMIVARIOGRAM TEXTURAL CLASSIFIER (STC) . . .	44
REVIEW OF IDENTIFICATION OF GEOLOGIC FEATURES IN CRYSTALLINE BASEMENT TERRANES USING GREY- SCALE AEROMAGNETIC IMAGES . . . . .	60
REVIEW OF DELINEATION OF MAGNETIZATION UNITS IN CRYSTALLINE BASEMENT TERRANES USING A TERRACING OPERATOR . . . . .	62
ANALYSIS AND INTEGRATION OF SPACEBORNE RADAR AND AEROMAGNETIC DATA: SUMMARY OF PROCEDURES . .	65
CHAPTER IV. SPACEBORNE RADAR ANALYSIS . . . . .	63
CHARACTERISTICS OF SIR-B DATA . . . . .	63
DISCRIMINATION OF VEGETATION TYPES AND WATER BODIES USING THE SEMIVARIOGRAM TEXTURAL CLASSIFIER (STC)	67
IDENTIFICATION OF TONAL LINEAR FEATURES USING A CONTRAST STRETCHING TECHNIQUE . . . . .	88
DEVELOPMENT OF A MAP OF SIR-B LINEAR FEATURES . .	92
CHAPTER V. AEROMAGNETIC ANALYSIS . . . . .	101
CHARACTERISTICS OF THE DIGITAL AEROMAGNETIC DATA	101
PRODUCTION OF A GREY-SCALE AEROMAGNETIC IMAGE .	109
DEVELOPMENT OF A TERRACE-MAGNETIZATION MAP OF THE GUIANA SHIELD AEROMAGNETIC DATA . . . . .	113

## TABLE OF CONTENTS

	<u>Page</u>
CHAPTER VI. RECONNAISSANCE GEOLOGIC MAP DERIVED FROM SPACEBORNE RADAR AND AEROMAGNETIC INFORMATION	136
COMPARISON OF SIR-B LINEAR FEATURES WITH THE TERRACE MAP AND MAGNETIZATION BOUNDARY LINES	136
COMPARISON OF TERRACE-MAGNETIZATION UNITS WITH GEOLOGIC DATA ACQUIRED IN THE FIELD BY THE RADAMBRASIL PROJECT . . . . .	141
DEVELOPMENT OF A RECONNAISSANCE GEOLOGIC MAP . .	147
CHAPTER VII. SUMMARY AND CONCLUSIONS . . . . .	153
RESULTS OBTAINED WITH THE ANALYSIS OF SPACEBORNE RADAR (SIR-B) DATA . . . . .	153
RESULTS OBTAINED WITH THE ANALYSIS OF AEROMAGNETIC DATA . . . . .	157
IMPLICATIONS FOR RECONNAISSANCE GEOLOGIC MAPPING IN THE GUIANA SHIELD AND CONTRIBUTION TO THE GEOLOGIC KNOWLEDGE OF NORTHWESTERN BRAZIL .	162
REFERENCES . . . . .	167

## PLATES

- Plate 1. Reduced-to-the-pole magnetic anomalies shown in grey-scale image format. Magnetic lows are dark; magnetic highs are bright. Magnetic patterns: a, b, c, and d. Artifacts: e (spots), f (flight-lines), and g (tie-lines). See text for explanation about 1 and 2.

## TABLE OF FIGURES

	<u>Page</u>
Figure 1. Location map of the study area. . . . .	8
Figure 2. Soil map (after Roessing et al., 1976) . . .	11
Figure 3. Phytoecological map (after Silva et al., 1976) . . . . .	14
Figure 4. Geomorphological map (modified after Nascimento and Prates, 1976) . . . . .	17
Figure 5. The Amazonian Craton (after Teixeira et al., 1989). The Guaporé Shield belongs to the Central Brazil Shield. . . . .	19
Figure 6. Geotectonic outline of the Amazonian Craton (after Teixeira et al., 1989). Key: 1- Phanerozoic sediments; 2-Sunsas mobile belt (1.1-0.90 b.y.); 3-Rondonian mobile belt (1.45-1.25 b.y.); 4-Rio Negro-Juruena mobile belt (1.75-1.5 b.y.); 5-Proterozoic platform covers (1.9-1.5 b.y.); 6-Maroni-Itacaiunas mobile belt (2.25-1.9 b.y.); 7-Central Amazonian Province ( 2.5 b.y.); 8-transition zone between belts; 9-approximate contacts between belts; 10-national boundaries. . . . .	20
Figure 7. Tectonic relationship between the Rondonian mobile belt (1.45-1.25 b.y.) and the two-mica granitoids of the Rio Negro-Juruena Province (simplified from Tassinari, 1981). . . . .	27
Figure 8. Basement geology of northwestern Brazil (simplified from Pinheiro et al., 1976). . .	29
Figure 9. Spherical model of semivariogram. . . . .	47

## TABLE OF FIGURES

	<u>Page</u>	
Figure 10.	Horizontal semivariogram at the level of the variance. It is produced by a data set having no spatial autocorrelation. . . . .	48
Figure 11.	Horizontal striped image (mean = 127.50; variance = 16289.91; size = 22 by 22 pixels). . . . .	49
Figure 12.	Randomized horizontal striped image (mean = 127.50; variance = 16289.91; size = 22 by 22 pixels). . . . .	50
Figure 13.	Semivariogram behavior (a) of a horizontal striped image and (b) of a spatially randomized image. Straight lines in both diagrams show variance of data sets. . . . .	51
Figure 14.	Surface units mapped from SIR-B image of coastal lowlands, Borneo. After Ford and Casey (1988). . . . .	53
Figure 15.	Training masks for water (1), tidal forest (2), coastal lowland forest (3), and swamp (4). After Miranda et al. (1990). . . . .	55
Figure 16.	Borneo image: decision boundaries for parallelepiped classification (multiplier = 2.00). After Miranda et al. (1990). . . . .	57
Figure 17.	Borneo image: classification result. Water = blue, tidal forest = green, coastal lowland forest = yellow, swamp = red. After Miranda et al. (1990). . . . .	59
Figure 18.	SIR-B image of the study area, Guiana Shield, Brazil (data take MC 118.30; portion of scene 107). Raw data. Image size is 1862 by 2268 pixels. W=water; O = open vegetation; D = dense vegetation, and F = flooded vegetation. . . . .	69

## TABLE OF FIGURES

	<u>Page</u>	
Figure 19.	Idealized profile showing the control of topography on the distribution of open, dense and flooded vegetation (modified after Silva et al., 1976). . . . .	74
Figure 20.	RADAMBRASIL X-band image showing the confluence of Piraiauara and Içana Rivers. . . . .	76
Figure 21.	Training masks for water (1), open vegetation (2), dense vegetation (3), and flooded vegetation (4). Training masks are 22 by 22 pixels large. Image size is 480 by 512 pixels. See Figure 22 for location. . . . .	78
Figure 22.	Location map of the SIR-B subscene where training masks were selected. . . . .	79
Figure 23.	Histograms and DN statistics of Guiana Shield training masks. . . . .	80
Figure 24.	Semivariograms of Guiana Shield training masks. . . . .	81
Figure 25.	Guiana Shield image: decision boundaries for parallelepiped classification (multiplier = 1.00). . . . .	85
Figure 26.	Guiana Shield: classification results including all classes. Image size is 480 by 512 pixels (for location see Figure 22). Water = dark blue; open vegetation = light blue; dense vegetation = yellow, flooded vegetation = red. See text for explanation about A, B, C, D, and E . . . . .	87

## TABLE OF FIGURES

	<u>Page</u>	
Figure 27.	Guiana Shield: classification results including only two classes (water and flooded vegetation). Image size is 1862 by 2268 pixels. Water = blue; flooded vegetation = red. See text for explanation about A and B. . . . .	90
Figure 28.	Linear geomorphic features defined on the basis of the spatial distribution of flooded vegetation. . . . .	92
Figure 29.	SIR-B contrast-stretched image using TLM (trackball linear mapping). . . . .	95
Figure 30.	Tonal linear features identified on X-band RADAMBRASIL SLAR images. . . . .	98
Figure 31.	Map of SIR-B linear features. . . . .	99
Figure 32.	Magnetic anomaly map (Guiana Shield). Contour interval is 100 nT. Hachures indicate areas of magnetic lows. . . . .	107
Figure 33.	Location map of the aeromagnetic data set. . . . .	108
Figure 34.	Second-order polynomial regional surface removed from the gridded magnetic anomaly data. Contour interval is 100 nT. . . . .	115
Figure 35.	Color-shaded relief map of the second-order residual magnetic field. Illumination is from north. Color level interval is 20 nT. . . . .	116
Figure 36.	Color shaded relief map of the filtered second-order residual magnetic field (filtered wavelengths: less than 3.0 km). Illumination is from north. Color level interval is 20 nT. . . . .	118



## TABLE OF FIGURES

	<u>Page</u>	
Figure 37.	Horizontal gradient of the pseudogravity transform of the filtered second-order residual magnetic field. Color levels represent the magnitude of the gradient. . . . .	120
Figure 38.	Magnetization boundary lines (maximum values of the horizontal gradient of the pseudogravity transform of the filtered second-order residual magnetic field). They are interpreted as magnetization boundaries at steep structural or lithologic contacts. . . . .	121
Figure 39.	Terraced pseudogravity transform of the filtered second-order residual magnetic field rescaled to cgs units of magnetization ( $\text{emu.cm}^{-3}$ ). This is the first magnetization function estimate. Color level interval is $0.00018 \text{ emu.cm}^{-3}$ . . . . .	123
Figure 40.	Color shaded relief map of the magnetic field calculated from the first magnetization function estimate. Illumination is from north. Color level interval is 20 nT. . . . .	124
Figure 41.	Magnetic field error due to the first magnetization function (Figure 36 minus Figure 40). Color shaded relief map. Illumination is from north. Color level interval is 20 nT. . . . .	126
Figure 42.	Second magnetization function estimate (terrace-magnetization map). Color level interval is $0.00018 \text{ emu.cm}^{-3}$ . Magnetic patterns identified on the grey-scale magnetic image (a, b, c, and d; Plate 1) are located for comparison. See text for explanation about 1, 2 and 3. . . . .	127

## TABLE OF FIGURES

	<u>Page</u>
Figure 43. Color shaded relief map of the magnetic field calculated from the second magnetization function estimate. Illumination is from north. Color level interval is 20 nT. . . . .	129
Figure 44. Magnetic field error due to the second magnetization function (Figure 36 minus Figure 43). Color shaded relief map. Illumination is from north. Color level interval is 20 nT. . . . .	130
Figure 45. Map of magnetization units. Boundary lines of Figure 38 are superimposed for comparison. . . . .	133
Figure 46. SIR-B linear features and magnetization boundary lines overlaid to the terrace-magnetization map of the study area .	139
Figure 47. Terrace-magnetization units and magnetization boundary lines overlaid to the terrace-magnetization map of the area depicted in Figure 8 . . . . .	142
Figure 48. Reconnaissance geologic map of crystalline basement terranes in the study area. . . . .	148
Figure 49. Schematic geologic cross section. . .	149

## TABLES

Table 1. Borneo image: statistical moments for water and vegetation training masks . . . . .	56
Table 2. SIR-B data characteristics in the study area. . . . .	70
Table 3. Decision boundaries (Guiana Shield) . . . . .	84

## CHAPTER I

## INTRODUCTION AND OBJECTIVES

This dissertation documents the result of a reconnaissance geologic mapping carried out in the Guiana Shield using digital aeromagnetic and spaceborne radar data. Its objective is to demonstrate that the integrated analysis of these data facilitate the development of geologic information on subtle geologic features in heavily forested and deeply dissected crystalline terranes of Precambrian age.

## STATEMENT OF PROBLEM

Notwithstanding the great contribution made by the RADAMBRASIL Project in the 1970s, geologic knowledge of the Guiana Shield is still incomplete. Detailed studies are only available in areas where exploration for mineral deposits has been performed. The Guiana Shield is host to important reserves of gold, aluminum, diamond, rare earth elements and manganese.

The portion of the Guiana Shield situated in northwestern Brazil is one of the least geologically known regions of the country. The study area was selected for investigation because it is characterized by a complex association of gneissic and granitoid rocks of middle Proterozoic age (Guianense Complex), which are not

individually recognized as distinct units in the RADAMBRASIL map. The area under investigation is devoid of significant rock exposures due to dense vegetation and thick soil cover. The topography has less than 20 m of relief over 10's of kilometers. Geologic structures and boundaries between different lithologic units have little apparent geomorphic expression.

Reconnaissance geologic mapping is usually the first step of mineral exploration projects in tropical, remote regions of South America. The objective of such an enterprise is to find out as much as possible about the geology of an unknown area as quickly as possible (Barnes, 1981). Scales are generally 1:250,000 or less. Some reconnaissance maps are mostly based on photogeology, with only a minimum amount of work done on the ground to identify rock types (e.g., RADAMBRASIL Project). However, a reconnaissance geologic map is more reliable when it incorporates information derived from regional aerogeophysical surveys. This is particularly true in rainforest-covered areas such as the Guiana Shield.

Spaceborne radar images are considered to be a valuable data set for geologic mapping in cloud-covered, heavily forested tropical regions. They are quite sensitive to surface slope, surface roughness, and the presence of water. They also have the capability of penetrating clouds. In

this study, images obtained by the shuttle imaging radar system SIR-B were used for discrimination of vegetation types and delineation of geologic structures.

The Brazilian portion of the Guiana Shield is extensively covered by aeromagnetic surveys. Therefore, part of this research is devoted to the analysis of such geophysical data. The data analysis delineated magnetization domains that may be associated with lithologic units of the Precambrian crystalline basement.

In order to derive a reliable geologic map from the combined radar and aeromagnetic information it is necessary:

- (1) to understand the connection between vegetation, topography and geologic structure in highly dissected, densely vegetated Precambrian crystalline terranes;
- (2) to devise an image classification technique for SIR-B data of the Guiana Shield that will display landscape features of geologic importance;
- (3) to interpret and display aeromagnetic data to facilitate extraction of useful geologic information;
- (4) to incorporate the already existing geologic information in the final interpretation result.

## GENERAL EXPERIMENTAL APPROACH

A methodology consisting of three components is pursued:

### Remote Sensing Component: Digital SIR-B Data

- a. Development of a strategy for discrimination of vegetation types and water bodies (rivers) using a semivariogram-based supervised classification algorithm.
- b. Identification of linear geomorphic features based on the spatial distribution of cover types (e.g., areas of flooded vegetation).
- c. Identification of tonal linear features using a contrast stretching technique.
- d. Development of a map of SIR-B linear features.

### Geophysical Component: Digital Aeromagnetic Data

- a. Generation of a grey-scale image of reduced-to-pole magnetic anomalies.
- b. Development of a map showing the terraced pseudogravity transform (rescaled to units of magnetization) of the second order residual magnetic field. Magnetization units are separated by sharp boundaries. Minor within-unit variation is neglected.

- c. Identification of maxima of the amplitude of the horizontal component of the pseudogravity gradient (boundary lines). They are supposed to represent magnetization boundaries at steep structural or lithologic contacts.
- d. Development of a map of boundary lines and magnetization units within the crystalline basement.

#### Data Integration and Analysis Component

- a. Superposition of maps derived from radar and aeromagnetic information. Areas of agreement are interpreted as geologic structures with geomorphic expression. Magnetization units are associated with Precambrian lithologic units.
- b. Comparison of final results with the geologic data acquired by the RADAMBRASIL Project (field descriptions of lithology and structure, Rb-Sr isochronic ages obtained for several rock samples).

#### MAJOR SCIENCE QUESTIONS ADDRESSED

The following major science questions are addressed by this study:

- (1) Is geologic mapping a feasible task in a relatively low relief, heavily-forested shield area devoid of significant rock exposures?

- (2) Can the middle Proterozoic gneissic and granitoid rocks of the Guianense Complex be individually recognized as distinct geologic units?
- (3) What is the connection between vegetation, topography and geologic structure in the deeply eroded crystalline terranes of the Guiana Shield?
- (4) What image processing technique should be applied to SIR-B data in order to discriminate vegetation types in a tropical environment?
- (5) Is it possible to map linear geomorphic features by observing the spatial distribution of cover types (water and flooded vegetation) on SIR-B images?
- (6) Can digital aeromagnetic data be used to outline lithologic units and geologic structures in the Guiana Shield?
- (7) Is the emerging picture of the magnetic basement structure consistent with the geomorphic framework obtained with SIR-B data?
- (8) Is the reconnaissance geologic map derived from the combination of radar and aeromagnetic data consistent with the information collected in the field by the RADAMBRASIL Project?





## STUDY AREA

### RATIONALE FOR SELECTION

The site selected for investigation embraces the confluence of the Içana and Piraiauara rivers (Figure 1). It covers an area of approximately 658 square kilometers (23.5 km by 28.0 km). It corresponds to a SIR-B subscene comprising 1862 x 2268 pixels. This region presents serious hindrances for geologic studies, such as:

- (1) the scale of the only available geologic map is 1:1,000,000;
- (2) dense vegetation and thick soil cover (the area is devoid of significant rock exposures);
- (3) precarious accessibility (field checking is performed almost exclusively along rivers);
- (4) flat topography (lithologic boundaries and geologic structures have no evident geomorphic expression);
- (5) almost perennial cloud cover (there are no cloud-free standard remote sensing products for extended areas in the visible and infra-red regions of the electromagnetic spectrum).

However, the crystalline igneous and metamorphic terranes occurring in this area are representative of a geologic scenario that prevails throughout most of the Brazilian portion of the Guiana Shield. In a rainforest

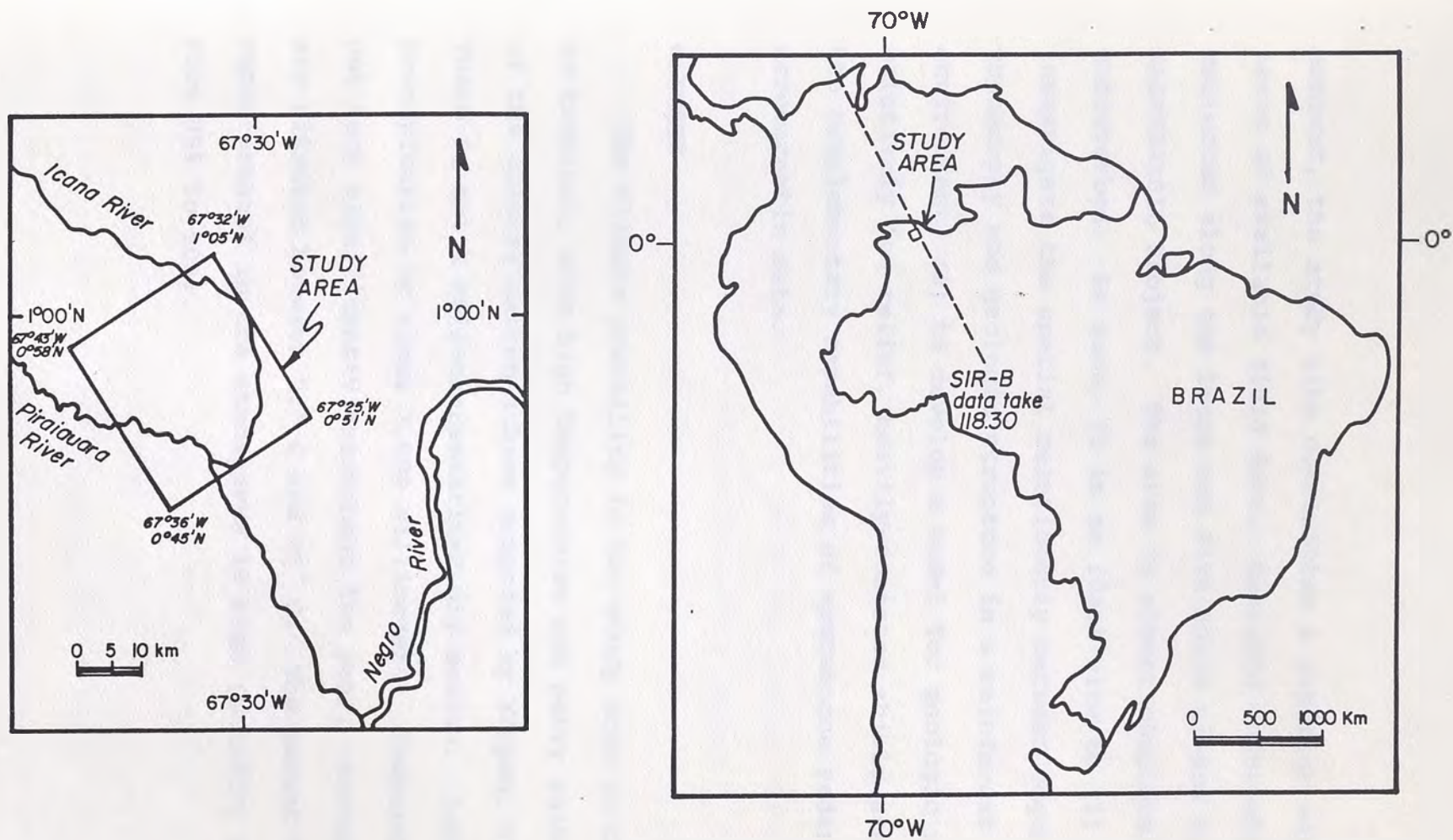


Figure 1. Location map of the study area.

context, the study site constitutes a superior setting in terms of available field data. Geologic information was collected along the Içana and Piraiauara rivers by the RADAMBRASIL Project. The area is almost completely undisturbed. As such, it is an ideal site to (1) investigate the spatial relationship between vegetation, topography and geologic structure in a rainforest environment; (2) to develop a model for geologic mapping of relatively low relief, heavily-forested shield areas using the complementary capabilities of spaceborne radar and aeromagnetic data.

#### CLIMATE

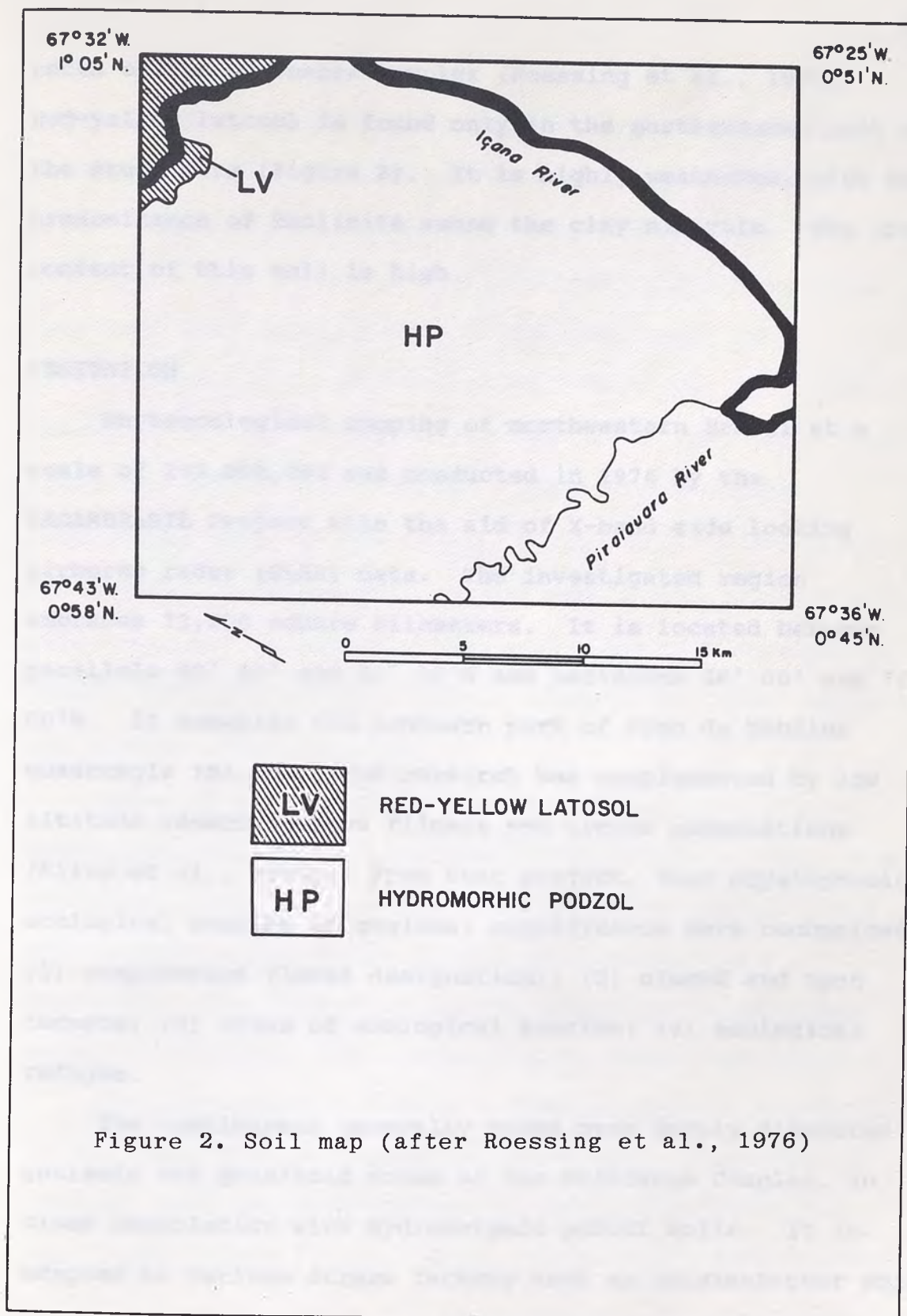
The climate prevailing in the study area is classified as tropical, with high temperatures and heavy rains (Af type of the classification scheme proposed by Köppen, 1948). There is not a well-characterized dry season. Annual precipitation is about 3,000 millimeters. Temperatures do not vary significantly throughout the year. Average values are situated between 24° C and 26° C. The amount of water vapor present in the atmosphere is high (humidity ranges from 85% to 90%).

## PEDOLOGY

Most soils of the Brazilian rainforest have low potential for supplying nutrients such as calcium and potassium to plants. This fact is due to the occurrence of intense weathering and leaching processes caused by high temperatures and heavy rains (Jordan, in Prance and Lovejoy, 1985). Despite the inability of the soil to retain and supply nutrients, the survival of the undisturbed forest is not endangered. This happens because rainforest tree species are adapted to the highly leached and weathered soils of the region. High concentrations of roots near the soil surface increase the efficiency with which nutrients are cycled from decomposing organic matter. In this tight recycling system, fewer nutrients can be leached beneath the rooting zone and lost from the ecosystem.

High annual rainfall is also responsible for the occurrence of widespread podzolization in northwestern Brazil (Silva et al., 1976). In such a process, a soil becomes more acid owing to depletion of bases. It also develops surface layers that are leached of clay, and presents illuvial B horizons (Bates and Jackson, 1987).

In the study area, the hydromorphic podzol is by far the most important soil type (Figure 2). It exists in places where the bedrock is many meters deep. It is composed mostly of coarse sand derived from the crystalline



rocks of the Guianense Complex (Roessing et al., 1976). Red-yellow latosol is found only in the northernmost part of the study site (Figure 2). It is highly weathered, with the predominance of kaolinite among the clay minerals. The iron content of this soil is high.

#### VEGETATION

Phytoecological mapping of northwestern Brazil at a scale of 1:1,000,000 was conducted in 1976 by the RADAMBRASIL Project with the aid of X-band side looking airborne radar (SLAR) data. The investigated region embraces 73,200 square kilometers. It is located between parallels 00° 00' and 02° 00'N and meridians 66° 00' and 70° 00'W. It occupies the southern part of Pico da Neblina quadrangle (NA.19). The research was complemented by low altitude reconnaissance flights and ground observations (Silva et al., 1976). From that project, four physiognomic-ecological domains of regional significance were recognized: (1) campinarana (local designation); (2) closed and open forests; (3) areas of ecological tension; (4) ecological refuges.

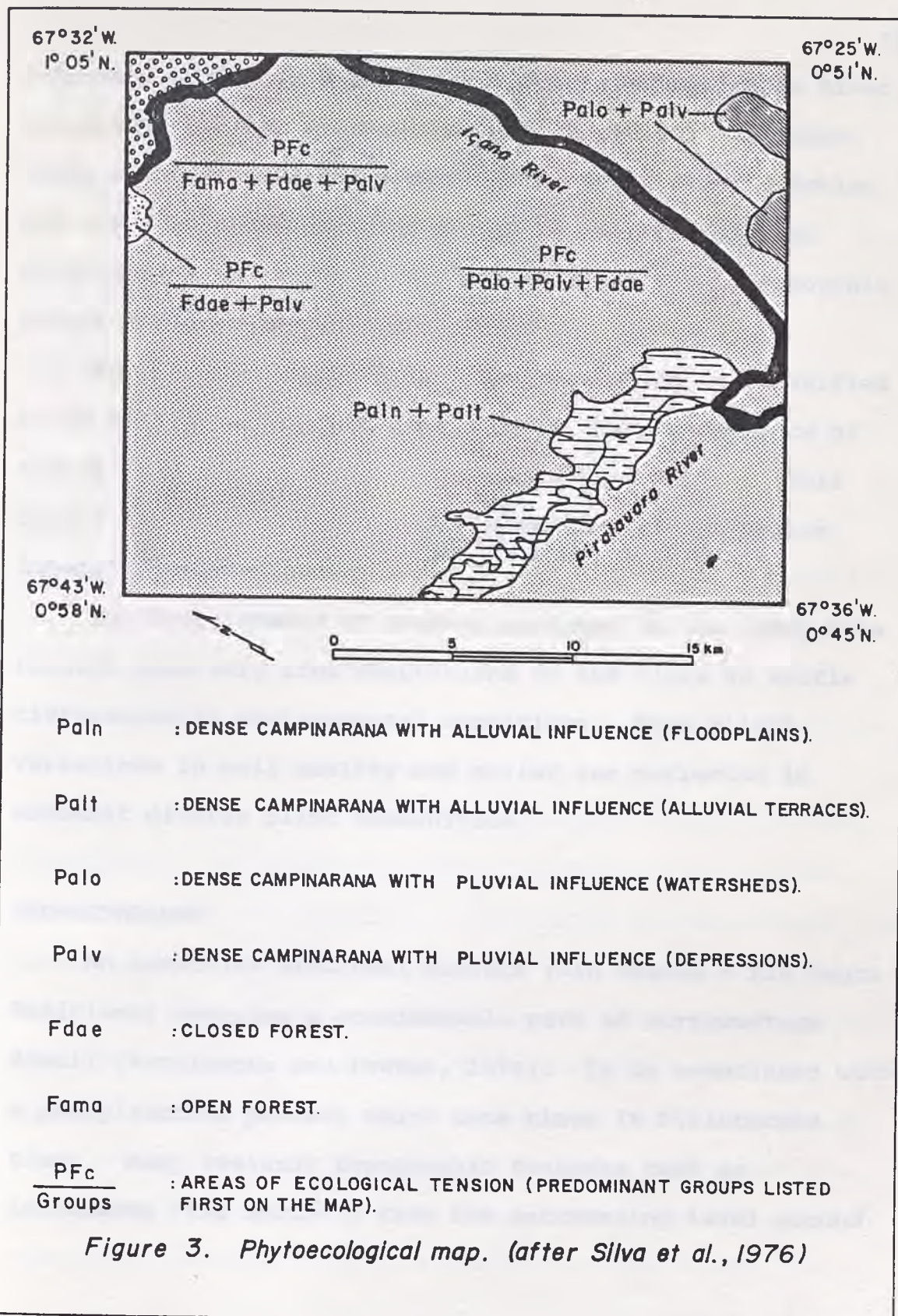
The campinarana generally grows over deeply dissected gneissic and granitoid rocks of the Guianense Complex, in close association with hydromorphic podzol soils. It is adapted to various stress factors such as nutrient-poor soil

and seasonal flooding. In watershed areas, there is a predominance of tamaquaré (*Caraipa sp* and *Clusia sp*). Buriti palms (*Mauritia flexuosa*) are common along floodplains.

The closed forest is distinguished by the occurrence of very tall trees arising from an uniform canopy (which is 25 to 35 meters high). The following species are very common: iebaro or iacano (*Eperua spp*), seringarana (*Mabea Taquali*), japurá (*Erisma sp*), cabari (*Clathrotropsis sp*), cedrorana (*Cedrelinga catanaeformis*), uacu (*Monopterix uacu*), matuti-duro (*Swartzia racemosa*) and cunuri (*Cunuria crassipes*). In the open forest, clusters of palm trees are widespread. The most important species are babaçu (*Orbygnia cf. racemosa*), patauá (*Oenocarpus sp*), açai (*Euterpe sp*) and paxiúba (*Iriartea ventricosa*).

Areas of ecological tension are characterized by a gradational change from campinarana to forest or vice versa. Ecological refuges are found in mountainous regions (1000 to 3000 meters) close to the border with Colombia and Venezuela. The vegetation in this physiognomic-ecological domain is predominantly constituted by bushes and herbs.

As illustrated in Figure 3, the majority of vegetation in the study site is classified as an area of ecological tension, with the predominance of campinarana (Palo and Palv) over closed forest (Fdae). Campinarana with pluvial





influence (Paln and Palt) occurs along the Piraiauara River. Restricted patches of campinarana with pluvial influence (Palo and Palv) are found east of the Içana River. Notice the close relationship that exists between the spatial distribution of campinarana-dominant areas and hydromorphic podzol soils (compare Figures 2 and 3).

North of the Içana River, the vegetation is classified as an area of ecological tension with the predominance of forest (Fama and/or Fdae) over campinarana (Palv). This region is characterized by the occurrence of red-yellow latosol (compare Figures 2 and 3).

The large number of vegetation types in the study area results from very fine adaptations of the flora to subtle differences in environmental conditions. Even slight variations in soil quality and relief are reflected in somewhat diverse plant communities.

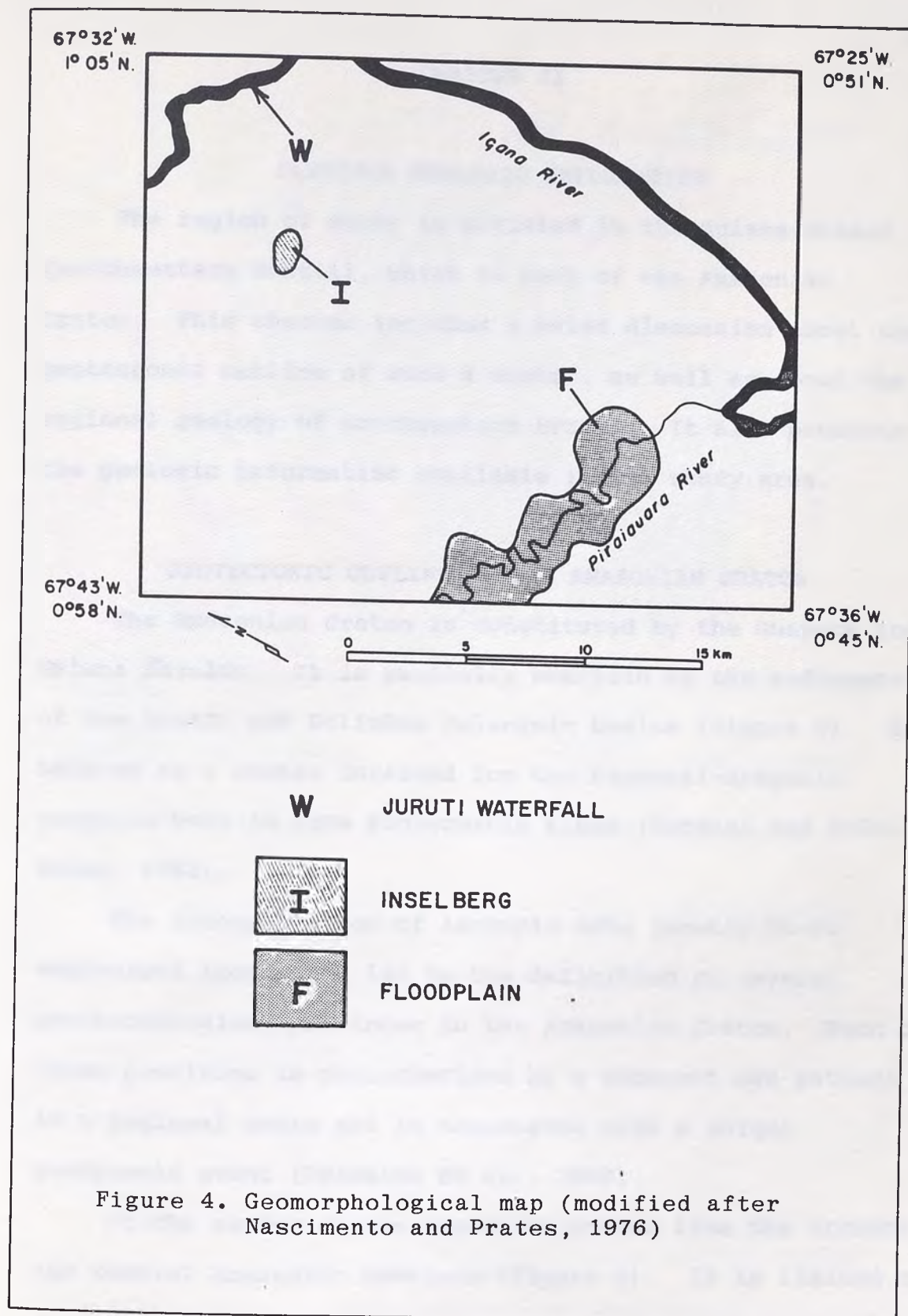
#### GEOMORPHOLOGY

An extensive erosional surface (Rio Branco - Rio Negro Pediplane) occupies a considerable part of northwestern Brazil (Nascimento and Prates, 1976). It is associated with a pediplanation process which took place in Pleistocene times. Many residual topographic features such as inselbergs rise abruptly from the surrounding level ground.

They were formed under a regime of concentrated heavy rainfall related to severe semiarid conditions prevailing during Pleistocene. According to Nascimento and Prates (1976), the last episode of dry weather finished 20,000 to 10,000 years ago.

Many rivers show waterfalls along their courses associated with topographic differences of up to eight meters. Such streams are using most of their erosional energy in downcutting the bedrock and smoothing out irregularities in gradient. According to Nascimento and Prates (1976), this fact suggests that the Rio Branco-Rio Negro Pediplane is being tilted southward as a result of recent tectonic activity.

The study area is included in the Rio Branco-Rio Negro Pediplane. An isolated inselberg can be found within it (Figure 4). The Piraiuara River presents a well developed floodplain. It is built of alluvium carried by the river during floods and deposited in the sluggish water beyond the influence of the swiftest current. Two geomorphological evidences indicate that the Içana River is downcutting the bedrock: the presence of the Juriti waterfall and the absence of alluvial deposits adjacent to the river channel. This attests that the Rio Branco-Rio Negro Pediplane is being tilted southward in the study site. The area along the Piraiuara River may be acting as a local hinge line.



## CHAPTER II

## PREVIOUS GEOLOGIC INFORMATION

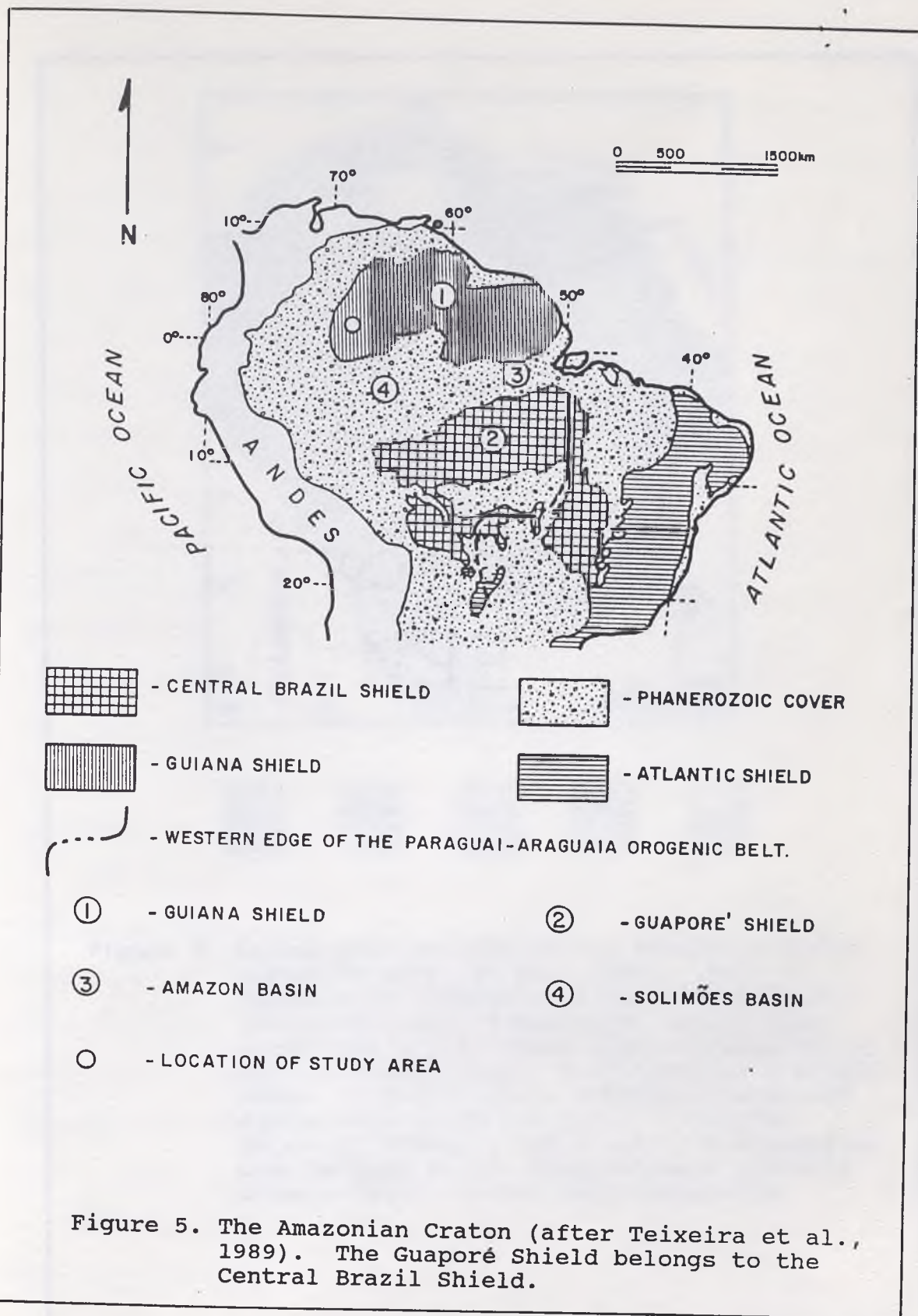
The region of study is situated in the Guiana Shield (northwestern Brazil), which is part of the Amazonian Craton. This chapter includes a brief discussion about the geotectonic outline of such a craton, as well as about the regional geology of northwestern Brazil. It also presents the geologic information available in the study area.

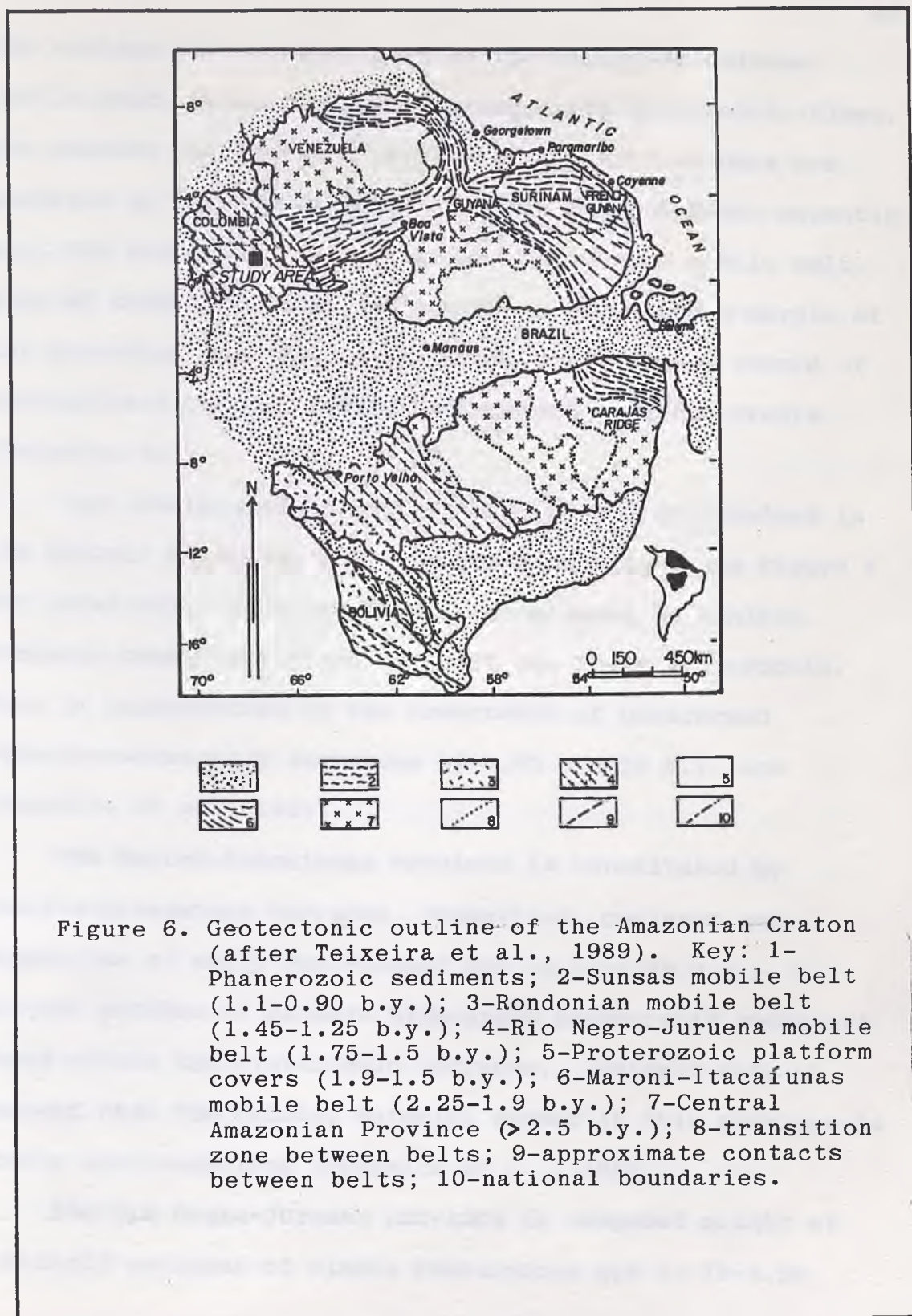
## GEOTECTONIC OUTLINE OF THE AMAZONIAN CRATON

The Amazonian Craton is constituted by the Guaporé and Guiana Shields. It is partially overlain by the sediments of the Amazon and Solimões Paleozoic basins (Figure 5). It behaved as a stable foreland for the Paraguai-Araguaia orogenic belt in late Proterozoic times (Cordani and Brito Neves, 1982).

The interpretation of isotopic data (mostly Rb-Sr whole-rock isochrons) led to the definition of several geochronological provinces in the Amazonian Craton. Each of these provinces is characterized by a coherent age pattern in a regional scale and is associated with a unique geodynamic event (Teixeira et al., 1989).

At the center of the Amazonian Craton lies the Archean age Central Amazonian Province (Figure 6). It is limited in





its eastern and northern part by the Maroni-Itacaiunas mobile belt, which developed during early Proterozoic times. The western and southern margins of the Archean core are bordered by three provinces: the Rio Negro-Juruena magmatic arc, the Rondonian mobile belt and the Sunsas mobile belt. Each of these provinces is located in the western margin of the preceding one (Figure 6). They constitute a record of successively younger middle Proterozoic orogenic events (Teixeira et al., 1989).

Age determinations of 2.70 b.y. have been obtained in the Central Amazonian Province (Carajás Ridge; see Figure 6 for location). This province is considered to exhibit cratonic conditions since at least the Lower Proterozoic. This is corroborated by the occurrence of undeformed volcano-sedimentary sequences of 1.90 - 1.50 b.y. age (Teixeira et al., 1989).

The Maroni-Itacaiunas Province is constituted by granite-greenstone terranes, granulites, gneisses and migmatites of early Proterozoic age (2.20-1.90 b.y.). Several patches of Archean high-grade metamorphic rocks are found within the Proterozoic terranes. Isotopic data suggest that the crustal material formed in this province is mostly mantle-derived (Teixeira et al., 1989).

The Rio Negro-Juruena Province is composed mainly of granitoid terranes of middle Proterozoic age (1.75-1.50

b.y.). So far no indication of older rocks has been found. Its isotopic character strongly suggests a mantle-derived magmatic arc origin. Conversely, the Rondonian (1.45-1.25 b.y.) and Sunsas (1.10-0.90 b.y.) provinces are mostly composed of reworked pre-existing crustal material. They are considered by Teixeira et al. (1989) to be related to intracontinental orogenic events.

Each province is characterized by its own syntectonic granitic plutonism (no granites older than the main orogenic phase are identified). Periods of anorogenic granitic plutonism are contemporaneous with tectonic activity in younger neighboring provinces.

#### REGIONAL GEOLOGY OF NORTHWESTERN BRAZIL

##### (RIO NEGRO-JURUENA PROVINCE)

In southwestern Venezuela and northwestern Brazil, the E-W trending Maroni-Itacaiunas mobile belt is truncated by the NW-SE structures of the Rio Negro-Juruena Province (Figure 6; see also the location of the study area). The geology of the latter province in this region is represented by a complex association of gneissic and granitoid rocks (Guianense Complex; Pinheiro et al., 1976). These rocks are not individualized as distinct units in the available RADAMBRASIL geologic map. However, Dall'Agnol and Abreu (1976) recognized three main lithologic types in this



region: sphene and amphibole-bearing biotite granitoids and gneisses; two-mica granitoids and gneisses; amphibolites and metabasic rocks. The first type is largely dominant in the area, while the second one is only important in the surroundings of the İçana River. Amphibolites and metabasic rocks are by far the least abundant ones. They won't be further discussed in the text.

The sphene and amphibole-bearing biotite granitoids vary from equigranular, coarse to medium grained rocks to very coarse, porphyritic ones. Megacrysts are represented by centimetric idiomorphic microcline. They are grey and relatively mafic rich rocks (10% to 15% modal content). The modal content of quartz is generally low (15% to 25%).

Petrographic types range from quartz-monzodiorite/ granodiorite to quartz-monzonite/monzogranite. The latter two are more frequent. The potassium feldspar has always the clear albite-pericline twinning typical of microcline. The plagioclase shows well developed normal zoning, with corrosion of the calcic cores. Its composition varies from calcic/sodic andesine to sodic oligoclase. Biotite is the dominant mafic mineral, being accompanied by a bluish green, low 2V angle amphibole (hastingsitic hornblende, ferro-hornblende or edenitic hornblende). Several noteworthy automorphic sphene crystals are also present. Opaque

minerals, epidote, allanite, apatite, zircon, and monazite are the accessory minerals (Dall'Agnol et al., 1987).

The two-mica granitoids are pink, equigranular, medium grained monzogranites to syenogranites, rarely quartz-syenites. They are richer in quartz than the sphene and amphibole-bearing biotite granitoids. The potassium feldspar is microcline. The plagioclase is calcic oligoclase, less commonly andesine, with more sodic rims. The mafic mineral content is lower than the sphene and amphibole-bearing biotite granitoids. Biotite and muscovite are always important minerals, while opaques, apatite, zircon, sphene, garnet, fluorite, tourmaline, allanite and rutile are the accessory ones. Tourmaline-bearing pegmatites are found associated with the granites. There are also granoblastic rocks composed of biotite, muscovite, quartz, sillimanite and andalusite, probably corresponding to metasedimentary inclusions in the granites (Dall'Agnol et al., 1987).

The typical sphene and amphibole-bearing biotite granitoids have low  $\text{SiO}_2$  content (about 65%) and high  $\text{TiO}_2$ ,  $\text{FeO} + \text{Fe}_2\text{O}_3$ ,  $\text{MnO}$ ,  $\text{MgO}$  and  $\text{CaO}$  values.  $\text{K}_2\text{O}$  is very high (about 6%);  $\text{Na}_2\text{O}$  is moderate (2.5 to 3%). Such values indicate the strong potassic nature of these granitoids. The Rb and Sr values are similar and generally range from

150 to 350 ppm, resulting in Rb/Sr ratios from 0.7 to 1.5 (Dall'Agnol et al., 1987).

The two-mica granitoids have higher SiO<sub>2</sub> content than the sphene and amphibole-bearing biotite granitoids (greater than 70%, except for the quartz sienites). They are very aluminous (with significant normative corundum) and show moderate contents of Fe<sub>2</sub>O<sub>3</sub> + FeO, MnO, TiO<sub>2</sub>, CaO and MgO. The K<sub>2</sub>O percentages are also very high and clearly dominant over those of Na<sub>2</sub>O. The Rb content is higher (about 300 ppm) than the Sr one (50 to 100 ppm). This results in relatively high Rb/Sr ratios (Dall'Agnol et al., 1987).

The two-mica granitoids have very low magnetic susceptibility values (Sauck and Dall'Agnol unpublished data, in Dall'Agnol et al., 1987). Conversely, the magnetic susceptibility of the sphene and amphibole-bearing biotite granitoids is reported by these authors to be high.

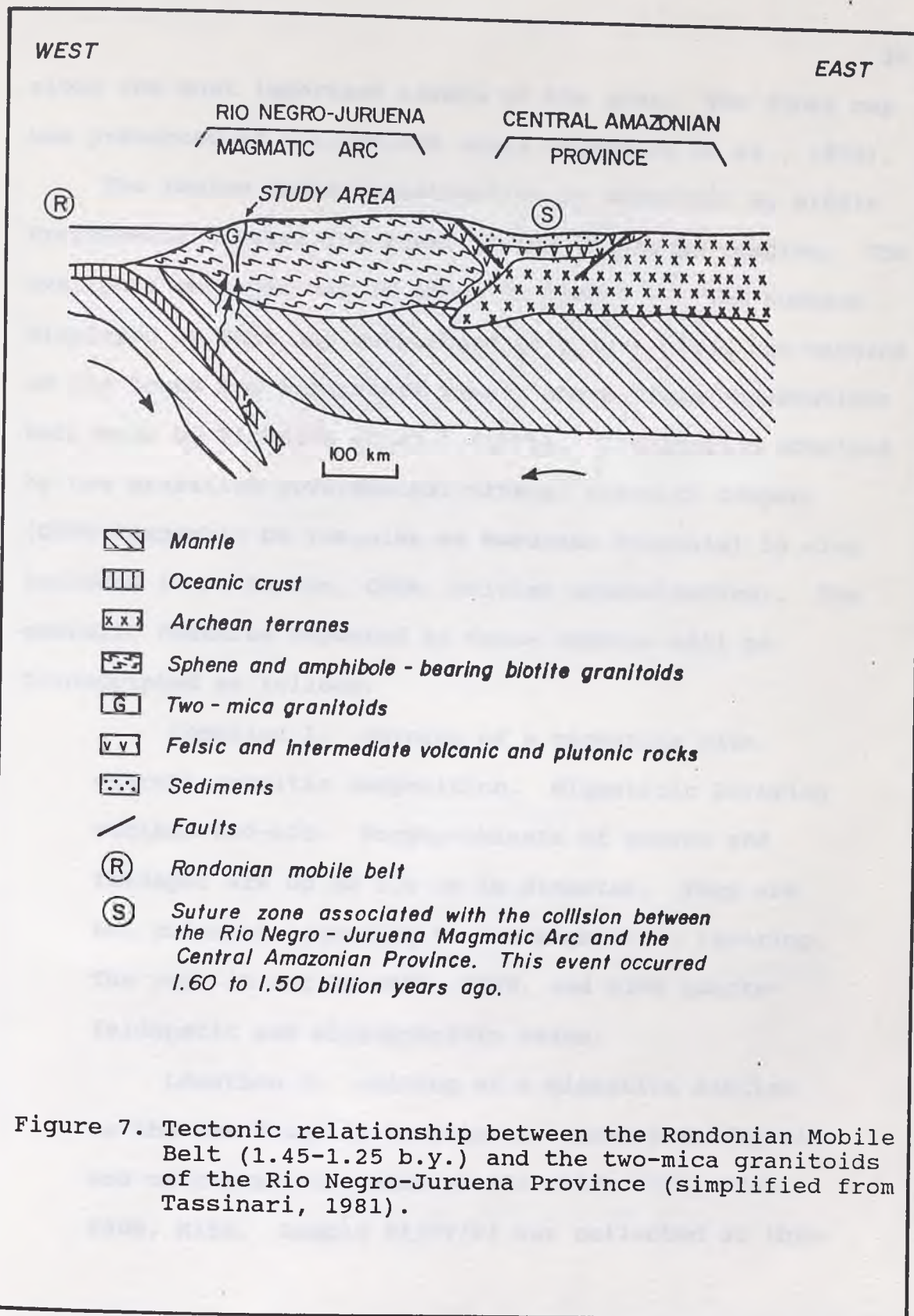
A Rb-Sr radiometric age of  $1640 \pm 26$  m.y. was obtained by Dall'Agnol and Abreu (1976) for the sphene and amphibole-bearing biotite granitoids, with Sr<sup>87</sup>/Sr<sup>86</sup> initial value of  $0.703 \pm 0.001$ . These authors also defined two Rb-Sr isochrons for the two-mica granitoids. The first one shows an age of  $1318 \pm 22$  m.y., with Sr<sup>87</sup>/Sr<sup>86</sup> initial value of  $0.722 \pm 0.002$ . The age of the second one is  $1225 \pm 23$  m.y., with Sr<sup>87</sup>/Sr<sup>86</sup> initial value of  $0.713 \pm 0.002$ . The low Sr<sup>87</sup>/Sr<sup>86</sup> initial value for the sphene and amphibole-bearing

biotite granitoids indicates a primary deep-seated origin, possibly a mantle derivation (Tassinari, 1981). Conversely, the high value of this parameter for the two-mica granitoids is consistent with an origin by melting of previously existent crustal material.

Tassinari (1981) considered the sphene and amphibole-bearing biotite granitoids to be part of the mantle-derived Rio Negro-Juruena magmatic arc (1.75 - 1.50 b.y.). The two-mica granitoids are supposed to be the result of anorogenic plutonism taking place in the Rio Negro-Juruena Province (Tassinari, 1981). This event was contemporaneous with the development of the Rondonian mobile belt (1.45 - 1.25 b.y.). Figure 7 illustrates the tectonic relationship between the Rondonian mobile belt and the two-mica granitoids intruding the Rio Negro-Juruena Province.

#### GEOLOGIC INFORMATION AVAILABLE IN THE STUDY AREA

The area of study is situated in the Pico da Neblina quadrangle, which embraces 73,200 square kilometers. The geological reconnaissance of such a region was performed by the RADAMBRASIL Project, based mainly on the interpretation of X-band side-looking airborne radar images at 1:250,000 scale. Field checking was carried out almost exclusively



along the most important rivers of the area. The final map was presented at 1:1,000,000 scale (Pinheiro et al., 1976).

The region under investigation is underlain by middle Proterozoic crystalline rocks of the Guianense Complex. The available geologic map is shown in Figure 8. The numbers displayed on this map correspond to points along the margins of the Içana and Piraiauara rivers where field observations were made by Pinheiro et al., (1976). Information obtained by the Brazilian governmental mineral research company (CPRM-Companhia de Pesquisa de Recursos Minerais) is also included (O.S. Santos, CPRM, written communication). The geologic features reported by these authors will be transcribed as follows:

Location 1: outcrop of a migmatite with overall granitic composition. Migmatitic layering strikes N30-40E. Porphyroblasts of quartz and feldspar are up to 5.0 cm in diameter. They are not oriented according to the migmatitic layering. The rock is cut by N85W, N65W, and N30E quartz-feldspatic and microgranitic veins.

Location 2: outcrop of a migmatite similar to the one found in location 1. Quartz-feldspatic and microgranitic veins strike N35E, N55W, N70W, N80W, N15E. Sample PI/EV/01 was collected at this

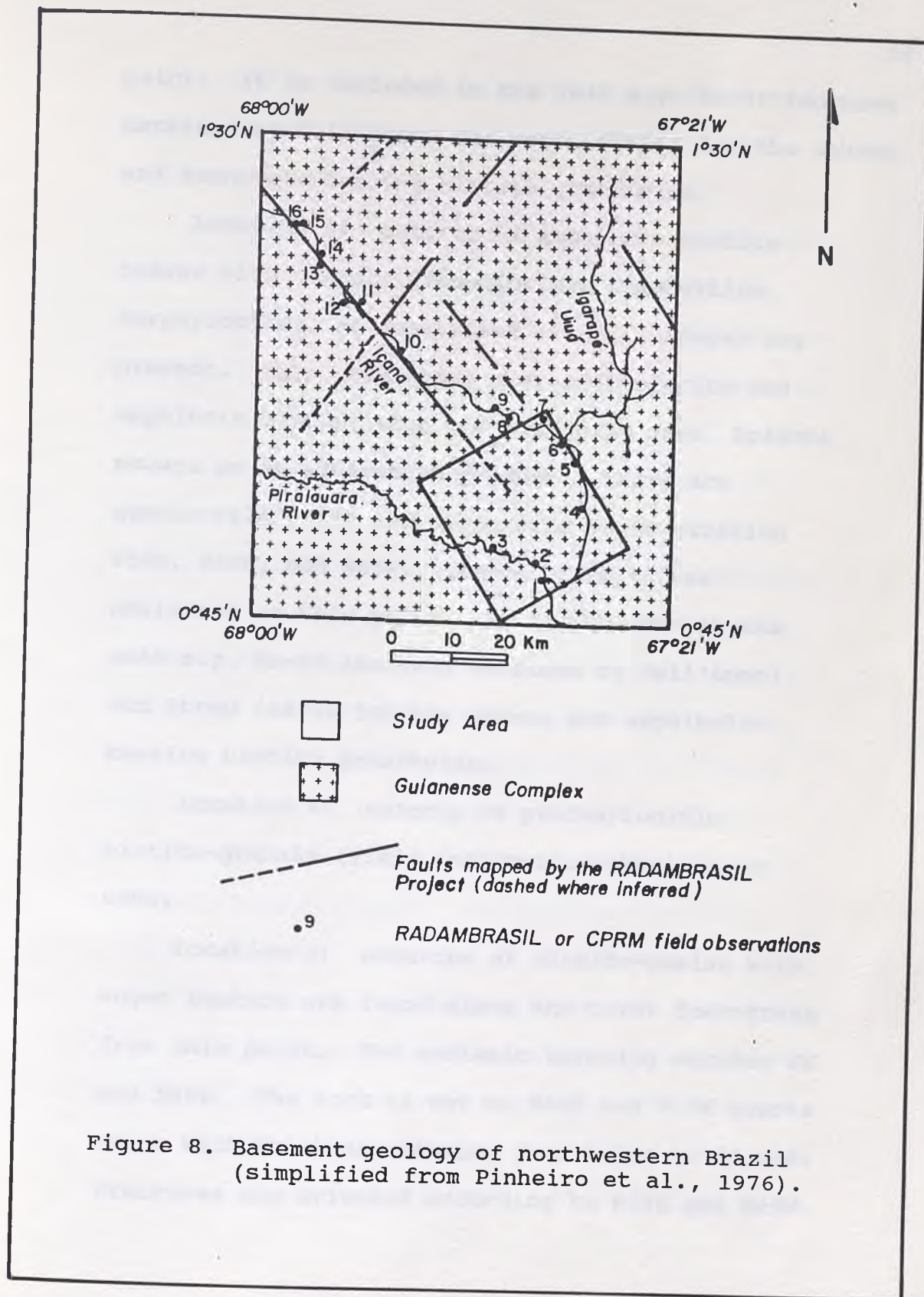


Figure 8. Basement geology of northwestern Brazil (simplified from Pinheiro et al., 1976).

point. It is included in the 1640 m.y. Rb-Sr isochron obtained by Dall'Agnol and Abreu (1976) for the sphene and amphibole-bearing biotite granitoids.

Location 3: outcrop of amphibole-biotite gneiss with overall granodioritic composition. Porphyroblasts of quartz and alkali feldspar are present. This rock shows a greater biotite and amphibole content than the preceding ones. Epidote occurs as an alteration product. There are quartz-feldspatic and pegmatitic veins striking N55W, N60W, and N65W. Sample PI/EV/04 was collected at this point. It is included in the 1640 m.y. Rb-Sr isochron obtained by Dall'Agnol and Abreu (1976) for the sphene and amphibole-bearing biotite granitoids.

Location 4: outcrop of protomylonitic biotite-granite (field information obtained by CPRM).

Location 5: outcrops of biotite-gneiss with augen texture are found along the river downstream from this point. The gneissic layering strikes EW and N80E. The rock is cut by N60E and N10W quartz veins with thickness ranging from 5.0cm to 20.0cm. Fractures are oriented according to N55E and N25W.



Location 6: outcrop of biotite-granite with megacrysts of feldspar reaching up to 4.0 cm. Fractures strike N65W, N40E, and EW.

Location 7: outcrop of quartz-monzonite with fractures oriented according to N50E and N70E.

Location 8: outcrop of porphyritic biotite-granodiorite with fractures oriented according to N70E.

Location 9: outcrop of muscovite-biotite granite (field information obtained by CPRM).

Location 10: outcrop of porphyritic biotite-granite with muscovite. Fractures are oriented according to N80W and N40E. Sample IÇ/EA/12 was collected at this point. It is included in the 1225 m.y. Rb-Sr isochron obtained by Dall'Agnol and Abreu (1976) for the two-mica granitoids.

Location 11: outcrop of protomylonitic biotite-granite (field information obtained by CPRM).

Location 12: outcrop of muscovite-biotite granite. The rock is cut by N70E quartz veins with average thickness of 5.0 cm. Fractures strike N60W and N70E.

Location 13: outcrop of muscovite-biotite granite. The rock is cut by pegmatitic veins striking N05E to N35E.

Location 14: outcrop of protomylonitic biotite-granite (field information obtained by CPRM).

Location 15: outcrop of muscovite-biotite granite (field information obtained by CPRM).

Location 16: outcrop of biotite-muscovite gneiss with sillimanite. Fractures are oriented according to N60E and N40W. Sample IÇ/EA/15 was collected at this point. It is included in the 1225 m.y. Rb-Sr isochron obtained by Dall'Agnol and Abreu (1976) for the two-mica granitoids.

The area of study is therefore characterized by the occurrence of migmatites and gneisses in its southern and central parts (e.g. locations 1, 2, 3, and 5; Figure 8). These rocks are considered to be representative of sphene and amphibole-bearing biotite granitoids (as defined by Dall'Agnol and Abreu, 1976). The protomylonitic biotite-granite outcropping in location 4 was produced by intense deformation of such crystalline metamorphic rocks. The northern part of the area is dominated by granites and quartz-monzonites (locations 6 and 7; Figure 8). Muscovite

is not as conspicuous in these rocks as in the typical two-mica granitoids.

Northwest of the study area, muscovite-bearing granitic rocks are reported to occur along the Içana River (e.g. locations 9, 10, 12, 13, 15, and 16; Figure 8). They are classified as two-mica granitoids by Dall'Agnol and Abreu (1976).

Major faults mapped by the RADAMBRASIL Project are presented in Figure 8. These structures were recognized with the aid of side-looking airborne radar images. They show predominantly NE-SW or NW-SE orientation. Their sense of movement is not known. A remarkable NW-SE fault controls the course of the Içana River where the two-mica granitoids are found (Figure 8). According to Pinheiro et al. (1976), it may continue southwestward into the study area. It is important to mention that the SLAR imagery was acquired by north-south aircraft flights using a westward look direction. Therefore, linear features with east-west orientation were practically invisible on the images. This introduced a serious bias in the structural interpretation made by the RADAMBRASIL Project in the Guiana Shield.

## CHAPTER III

## METHODOLOGY

This chapter presents the investigation procedures used in each major phase of the research: (a) geologic interpretation of spaceborne radar images in heavily-forested regions; (b) vegetation discrimination in spaceborne radar images of rainforest areas using the semivariogram textural classifier; (c) identification of geologic features in crystalline basement terranes using grey-scale aeromagnetic images; (d) delineation of magnetization units in crystalline basement terranes using a terracing operator; (e) integration of information derived from spaceborne radar and aeromagnetic data.

#### REVIEW OF PREVIOUS GEOLOGIC INTERPRETATIONS OF SPACEBORNE RADAR IMAGES IN HEAVILY-FORESTED REGIONS

Imaging radars are very sensitive to surface expressions of present and past tectonic activity (Sabins, 1987). The ability of such sensors to detect topographic discontinuities (a key physiographic expression of structural deformation) has been very useful in the geologic mapping of heavily-forested regions (NASA, 1989).

SEASAT. The first spaceborne imaging radar to survey the Earth was the L-band synthetic aperture system on board Seasat, an instrument package launched into a 800 km altitude near-polar orbit in June 1978 (Fu and Holt, 1982). This horizontally polarized instrument operated at a fixed wavelength (23 cm) and at a fixed look angle ( $20^\circ$  from nadir). The Seasat swath width was 100 km and the theoretical resolution on the surface was approximately 25 m. The near-nadir incidence angle of Seasat (about  $23^\circ$ ) was ideal for acquiring strong oceanic returns, but produced severe layover distortions on terrain images of high-relief regions (NASA, 1989).

Although Seasat was launched primarily for oceanographic studies, radar images were also acquired over land regions in the northern hemisphere. Geologic interpretation of this data set was performed in the surroundings of the Pine Mountain thrust fault (Tennessee-Kentucky-Virginia). This feature marks the separation between the Cumberland Plateau to the north, and the Valley and Ridge Province to the south (Ford et al., 1980). The area is densely forested and covered by a mixed deciduous/coniferous canopy. Steep slopes that face the radar beam appear bright. Folded strata are enhanced by radar sensitivity to changes of slope. Many extensive topographic lineaments are related to major known faults. Geomorphic units are reflected on the

Seasat image as textural domains. They show a good correlation with distinct bedrock associations and bulk lithologic sequences (Ford, 1980).

SHUTTLE IMAGING RADAR. The next spaceborne SAR to follow Seasat was the Shuttle Imaging Radar-A (SIR-A). It was placed by the Space Shuttle Columbia into a 38° inclination, 259 km altitude orbit in November 1981 (Ford et al., 1983). The SIR-A swath width was 50 km and the resolution on the surface was approximately 40 m. The radar system was similar to Seasat (23 cm wavelength and HH polarization). However, since the SIR-A mission was to be used primarily for geological research, the look angle was changed to a fixed value of 47°. The higher incidence angle (about 50°) provided enhanced sensitivity to structural features such as faults and folds (NASA, 1989). SIR-A images showed less severe layover distortion than Seasat data in high-relief regions.

Indonesia was selected as a SIR-A test site for the following reasons (Sabins, 1983): (a) the persistent cloud cover in Indonesia has hampered the acquisition of remote sensing information in the visible and infrared portions of the electromagnetic spectrum; (b) Indonesia provides a representative test for the geological utility of spaceborne radar images obtained over rugged, vegetated terrain. Although radar does not completely penetrate the foliage due

to volume scattering, geologic features are commonly enhanced on radar images by changes in topography underlying the vegetation canopy; (c) because of its present and potential petroleum reserves, Indonesia is an excellent site for evaluating satellite radar data for energy exploration; (d) a wide range of rock types and structures occurs in Indonesia, providing the opportunity to establish the radar signature of these features; (e) Indonesia is a key region to understanding global plate tectonics.

According to Sabins (1983), the vegetation cover in Indonesia masks the surface roughness of bedrock. However, under favorable circumstances, broad categories of rocks may be recognized by their topographic characteristics on radar images:

- (1) carbonate terrain: in humid environments, solution and collapse of carbonate rocks produce Karst topography which is readily recognized by the distinctive pitted surface. In Indonesia, carbonate terrain generally occurs as uplands surrounded by lowlands eroded from less resistant rocks;
- (2) clastic terrain: clastic sedimentary terrain is recognized by the occurrence of cuestas and hogbacks where the rocks are dipping. Flat-lying clastic rocks develop terraces and associated erosional scarps. The lack

- of Karst topography generally distinguishes clastic from carbonate terrains in humid regions;
- (3) volcanic terrain: areas formed by young volcanic rocks are recognized on SIR-A images by irregular lava flows associated with conical knobs formed by cinder cones or eroded volcanic necks;
  - (4) alluvial and coastal terrain: this category is characterized by uniform image tone, low relief, and the presence of estuaries and meandering streams;
  - (5) melange terrain: melange refers to lithologic units developed in subduction zones. They consist primarily of clastic sediments as well as of rocks derived from oceanic crust and mantle. Lenticular rock fragments of a wide range of sizes, up to kilometers in length, are enclosed in a matrix of sheared clay which may be slaty or phyllitic. Erosion of these rocks produces an irregular, rounded terrain with unsystematic drainage patterns. Stratification is not recognizable at the scale of radar images, nor are individual rock fragments detectable;
  - (6) metamorphic terrain: they are constituted by sedimentary rocks that have been metamorphosed to slate, quartzite and schist. The highly dissected metamorphic terrain has high relief and angular ridges that distinguish it from the lower relief and rounded appearance



of melange terrain. Foliation trends are not discernible at the scale of SIR-A images;

(7) undifferentiated bedrock: because of erosion and deformation, features of younger volcanic terrains are lacking in older volcanic areas which cannot be recognized on SIR-A images without additional information.

The radar signature of dipping layers depends upon the relationship between dip slopes and radar look direction (Sabins, 1983). If the strata dip toward the radar beam, dip slopes have bright signatures. Antidip scarps, which are in the radar shadow, have dark signatures. Where beds dip away from the radar beam, the antidip scarps are bright and the dip slopes are dark. These relationships between look direction, dip slopes, and SIR-A image signature were seen by Sabins (1983) in Indonesia along the flanks of folds.

Sabins (1983) reported that lineaments were generally expressed on the SIR-A images of Indonesia as escarpments, linear rivers, and aligned drainage segments. He found good correlation between image linear features and previously mapped faults.

The next spaceborne mission carried out by NASA was the Shuttle Imaging Radar-B (SIR-B). It was launched in October 1984 on the Space Shuttle Challenger. SIR-B also used

Seasat/SIR-A technology (23 cm wavelength and HH polarization). However, this system was equipped with an articulating antenna so that selectable look angles could be obtained over the  $15^{\circ}$  -  $60^{\circ}$  range. In addition, SIR-B data were the first to be digitally encoded and processed (Cimino et al., 1988).

The SIR-B system acquired digital data over the heavily vegetated and cloud-covered Guiana Shield region. It operated at a fixed look angle of  $35^{\circ}$  (rather than at a multi-angle mode as previously planned), what prevented stereo radar investigations. The image swath was approximately 24 km wide. The SIR-B data take extended for many hundreds of kilometers in length. It may provide only a restricted view of geological features owing to its limited width (Ford and Sabins, 1986).

The first attempt to use such data in local structural studies was made by Ford et al. (1986). The SIR-B image analyzed by them covers a portion of the Guiana Shield localized in northwest Brazil and southwest Colombia. It displays outcrops of folded Precambrian metasediments (Tunui Group) that comprises the Serra do Caparro (Brazil) and part of the Serrania de Nanquen (Colombia). This stratigraphic unit has very restricted distribution in the Brazilian part of the Guiana Shield. The Caparro and Nanquen mountains rise to about 300 m above the level of underlying rocks

(migmatites, granites and gneisses of the Guianense Complex). The remote, jungle-covered area is inaccessible.

At the 35 degree look angle used in this SIR-B scene, dip slopes facing the radar beam have very bright signatures. This indicates that they are steep, perhaps 30° or more (Ford et al., 1986). Outcrop patterns and bedding attitudes of the rocks belonging to the Tunui Group define a series of small anticlines and synclines. The southern part of the Serra do Caparro is displaced relative to the northern part by the Caparro fault. This is a right-lateral strike-slip fault whose extension in the crystalline terranes of the Guianense Complex is scarcely perceptible. This happens because such fault has no evident topographic expression in the crystalline area and is oriented nearly parallel to the radar direction of illumination (Ford et al., 1986). In fact, apart from the problem of illumination geometry, it is much more difficult to identify structural features in the deeply dissected metamorphic areas of the Guianense Complex than in the relief-forming metasediments of the Tunui Group.

From the above discussion, it is apparent that visual interpretation of spaceborne radar images can be very useful in the geologic mapping of heavily-forested, humid regions. This is especially true when structural features such as folds and major faults are enhanced on radar data by changes

in bedrock topography underlying the vegetation canopy. Under favorable conditions, broad lithologic categories may be recognized by their geomorphological characteristics on radar images (e.g., Karst topography distinguishes carbonate-rich sequences; cinder cones help to identify young volcanic rocks). However, the deeply dissected crystalline terranes of the Guiana Shield represent a departure from the geologic examples presented so far (namely, Pine Mountain thrust fault, Indonesia, and Caparro/Nanquen mountains). In this region, relief is completely flat. Lithologic boundaries and geologic structures have no evident topographic expression, what prevents the utilization of classic geomorphological criteria in the interpretation of SIR-B images. However, spaceborne radars are an invaluable tool for flooding detection in forested floodplains (Hess et al., 1990). The bright appearance of flooded forests on L-band, HH polarization radar images results from double-bounce reflections between smooth water surfaces and tree trunks or branches. Enhanced backscattering on SIR-B images has been shown to occur in tropical floodplain forests (Ford and Casey, 1988). In the Guiana Shield, flooded vegetation was considered a key cover type for the recognition of minor topographic differences (up to 8 m) possibly associated with underlying geologic structures.

The identification of spatial radiometric patterns on the SIR-B image was regarded as important for structural mapping in the study area. Examples of such patterns are individual linear features developed on an uniform background and linear stream channels with bright radar signatures associated with flooded vegetation. This task was performed using a digital image processing technique (as suggested by Lowman et al., 1987, and by Masuoka et al., 1988). A simple contrast stretch program called TLM (track-ball linear mapping) effectively enhanced remarkable tonal linear features on the SIR-B image of the study area (as presented in Chapter 4). The geologic significance of these features is discussed in Chapter 6. The analysis of SIR-B data was conducted on a VAX 11/780 based Interactive Digital Image Manipulation System (IDIMS) at the Mackay School of Mines.

VEGETATION DISCRIMINATION IN SPACEBORNE RADAR  
IMAGES OF RAINFOREST AREAS USING THE  
SEMIVARIOGRAM TEXTURAL CLASSIFIER (STC)

Semivariograms are considered to be an important tool in the analysis of ore deposits (Journel and Huijbregts, 1978). They are also very useful in the study of remote sensing images (Carr and Myers, 1984; Curran, 1988; Glass et al., 1988; Jupp et al., 1988; Woodcock et al., 1988a; Woodcock et al., 1988b; Curran and Dungan, 1989; Jupp et al., 1989; MacDonald and Carr, 1989; Ramstein and Raffy, 1989; Rubin, 1989; Wald, 1989; Aymard and MacDonald, 1990). In this research, a semivariogram-based textural classifier was utilized to discriminate and map distinct vegetation units (especially flooded vegetation) in the SIR-B data of the Guiana Shield. The digital number (DN) assigned to each SIR-B pixel is a scaled representation of the integrated backscatter from the canopy contained within a single ground resolution cell. In the study site, each ground resolution cell measures about 20 m in the range direction by 30 m in the azimuth; a resolution at which the radar does not resolve individual trees. Vegetation units were visually distinguished as groups of pixels with similar DN values over extended areas (as discussed in Chapter 4).

According to Matheron (1963), a regionalized variable is one that has a fixed location in space. By this definition, the DN (digital number) values in remote sensing images represent a regionalized variable. The semivariogram function characterizes the spatial structure of a regionalized variable. It has the following form:

$$\gamma(h) = \left[ \frac{1}{2n} \sum_{i=1}^n [z(x_i) - z(x_i+h)]^2 \right], \text{ where:}$$

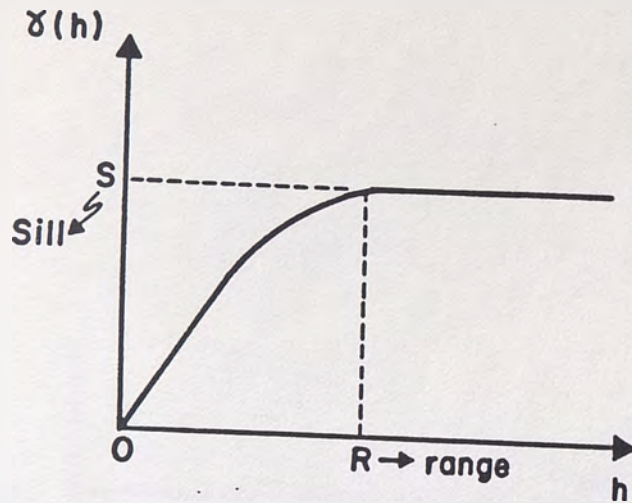
- $\gamma(h)$  = semivariogram function
- $Z(x_i)$  = value at location  $x_i$
- $Z(x_i+h)$  = value at a location  $h$  away from  $x_i$
- $n$  = number of pairs being compared
- $h$  = separation or lag distance

The shape of the semivariogram function is a reflection of the degree of autocorrelation between samples. The ideal shape of a semivariogram has a value of zero for  $h=0$  (there is no difference between any value and itself), rises smoothly upwards and curves into a straight horizontal shape. As the value of  $\gamma(h)$  increases with the separation distance, the degree of spatial autocorrelation between samples decreases until a value of  $h$  is reached at which  $\gamma(h)$  does not increase. This value of  $\gamma(h)$  is referred to as the sill, and represents the variance of the data set. The value of  $h$  at which  $\gamma(h)$  no longer increases is called the range. This semivariogram shape is referred to as

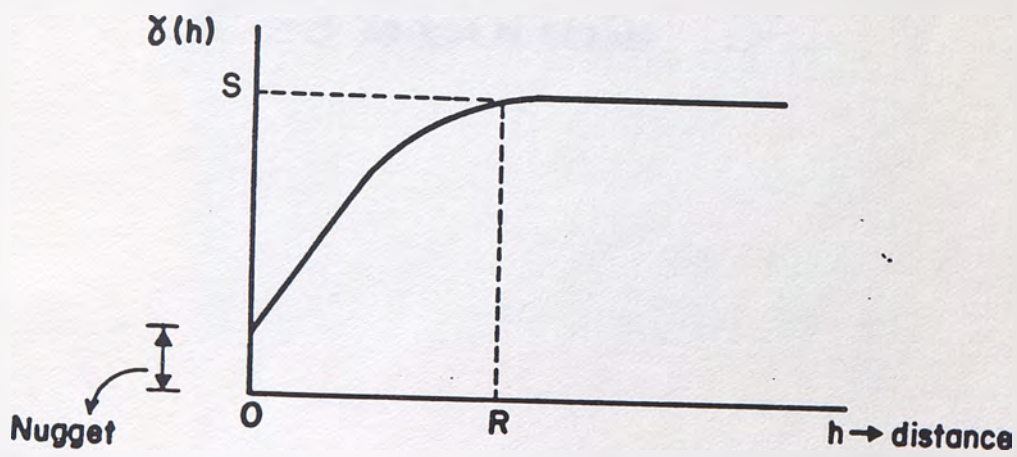
spherical (Figure 9a). Beyond the range two samples have no influence upon each other, i.e., knowledge of one sample tells us nothing about the value of the other. Often there is an apparent failure of the semivariogram to go through the origin, in which case a nugget effect is involved (Figure 9b). This circumstance is believed to be the result of spatial randomness within the data set. A completely random data set would result in a semivariogram defined by a straight horizontal line at  $\gamma(h) = \text{variance}$  (Figure 10).

A simple experiment was performed by MacDonald et al. (1990) in order to determine whether semivariograms contain textural information. The black and white horizontal striped image shown in Figure 11 was randomly scrambled. The resultant image is depicted in Figure 12. Semivariograms were then calculated for the original and scrambled images. The semivariogram of the original image presented a cyclical character (Figure 13a). It converged to a point corresponding to the variance of the data. The scrambled image semivariogram was a straight line at the level of the variance (Figure 13b). It is similar to the pure nugget effect semivariogram displayed in Figure 10. Note that the overall mean and variance of the digital images were not affected by the scrambling process. MacDonald et al. (1990)



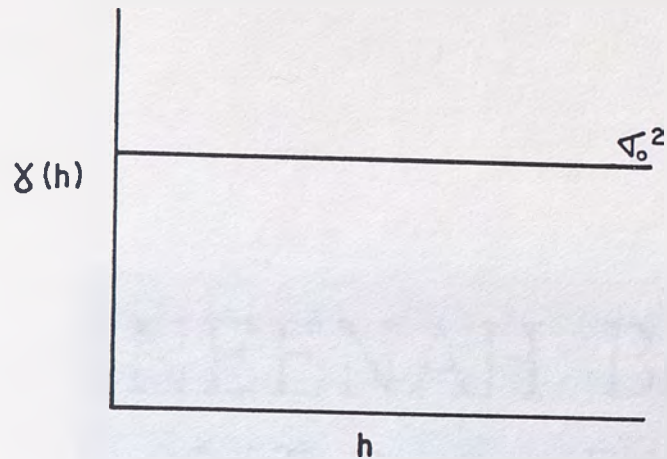


(a) Semivariogram passing through the origin.



(b) Semivariogram showing a nugget effect.

Figure 9. Spherical model of semivariogram.



$\sigma_0^2 \rightarrow$  variance of data set

Figure 10. Horizontal semivariogram at the level of the variance. It is produced by a data set having no spatial autocorrelation.

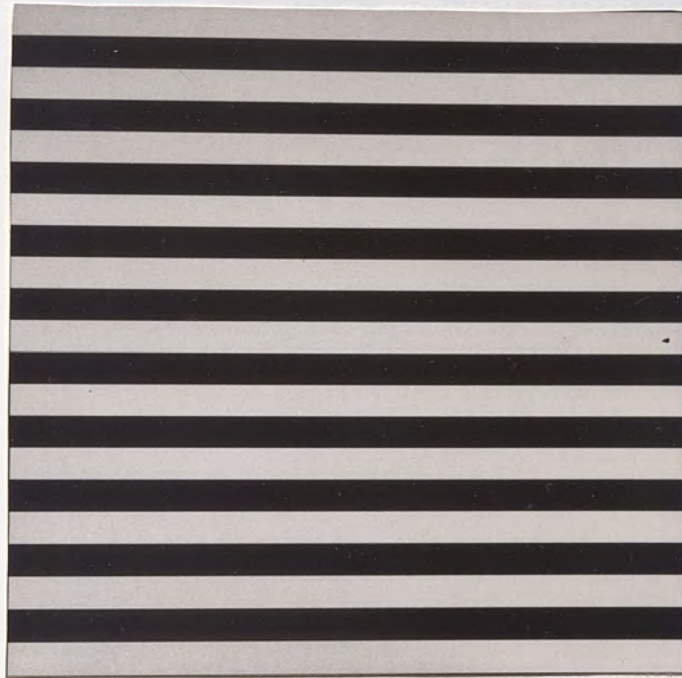
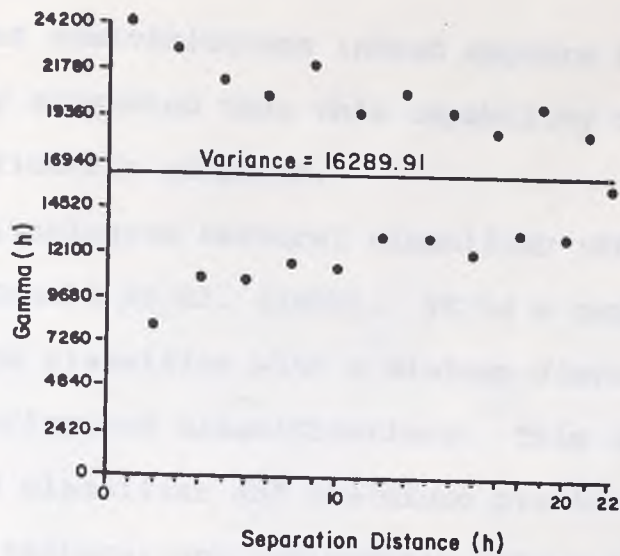


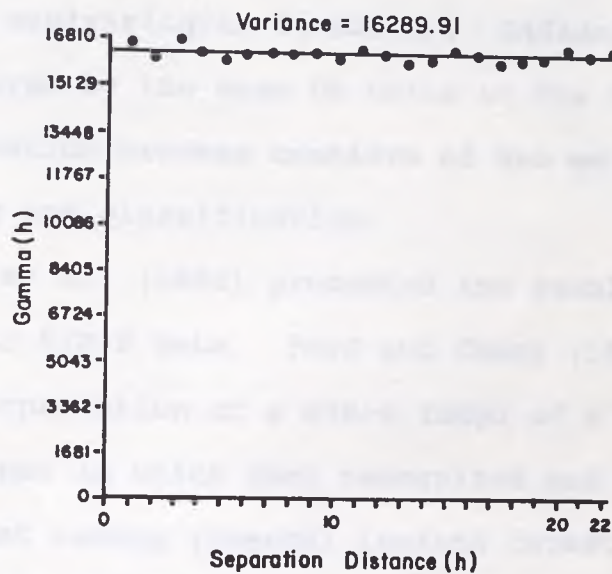
Figure 11. Horizontal striped image (mean = 127.50; variance = 16289.91; size = 22 by 22 pixels).



Figure 12. Randomized horizontal striped image (mean = 127.50; variance = 16289.91; size = 22 by 22 pixels).



(a) Semivariogram of original horizontal striped image.



(b) Semivariogram of randomized horizontal striped image.

Figure 13. Semivariogram behavior (a) of a horizontal striped image and (b) of a spatially randomized image. Straight lines in both diagrams show variance of data sets.

concluded that semivariograms indeed capture textural information. They suggested that this capability can be used for image classification purposes.

The semivariogram textural classifier (STC) was proposed by MacDonald et al. (1990). It is a supervised parallelepiped type classifier with a minimum distance to mean check for overlapping classifications. This is a strictly deterministic classifier and therefore provides the option of combining textural and radiometric information. Textural information is expressed by the spatial structure of a surface cover type (which is described by the shape and value of the semivariogram function). Radiometric information is conveyed by the mean DN value of the cover type. The classification process consists of two major sub-processes: training and classification.

Miranda et al. (1990) presented the results of an STC application to SIR-B data. Ford and Casey (1988) performed a visual interpretation of a SIR-B image of a tropical rainforest of Borneo in which they recognized and mapped three units of forest canopy (coastal lowland forest, tidal forest and swamp) and two units of open areas (clearcut and wetland). The resultant map is shown in Figure 14. Miranda et al. (1990) classified the same SIR-B image using STC in an attempt to emulate Ford and Casey's interpretation.

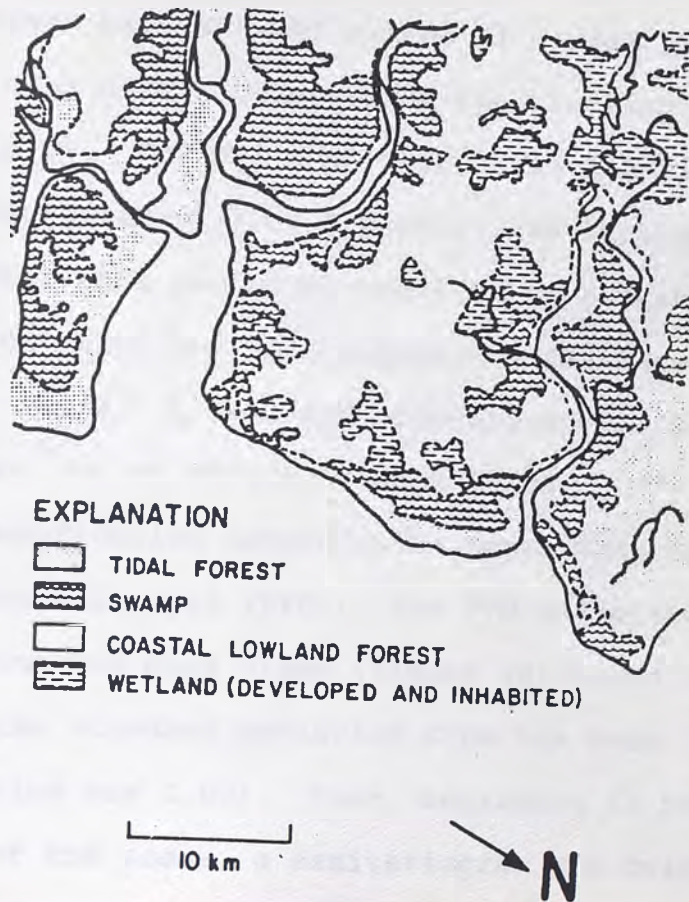


Figure 14. Surface units mapped from SIR-B image of coastal lowlands, Borneo. After Ford and Casey (1988).

Four classes selected by Ford and Casey (1988) were used by Miranda et al. (1990) in this experiment (Figure 15): water (1), tidal forest (2), coastal lowland forest (3), and swamp or flooded vegetation (4). The training subprocess began with the definition of a mask (22 by 22 pixels) for each class, under which the training was performed (Table 1). The STC then calculated a semivariogram within a moving window (7 by 7 pixels) for each pixel in the training mask. This procedure resulted in a mean and standard deviation value for each separation distance (up to six) in each class. A mean and standard deviation were also calculated for the DN values of each class.

The classification subprocesses began with the definition of a parallelepiped (PPD). The PPD established boundary conditions for each class (Figure 16) based upon a multiple of the standard deviation from the mean (in that case, this value was 2.00). Then, beginning in the upper left corner of the scene, a semivariogram was calculated for the window surrounding each pixel (keeping the same dimension as the moving window used in the training subprocess). The resulting semivariogram, along with the DN value of the central pixel, were compared with the PPD values. If the value of each separation distance and the DN were situated between the minimum and maximum boundaries for any class,



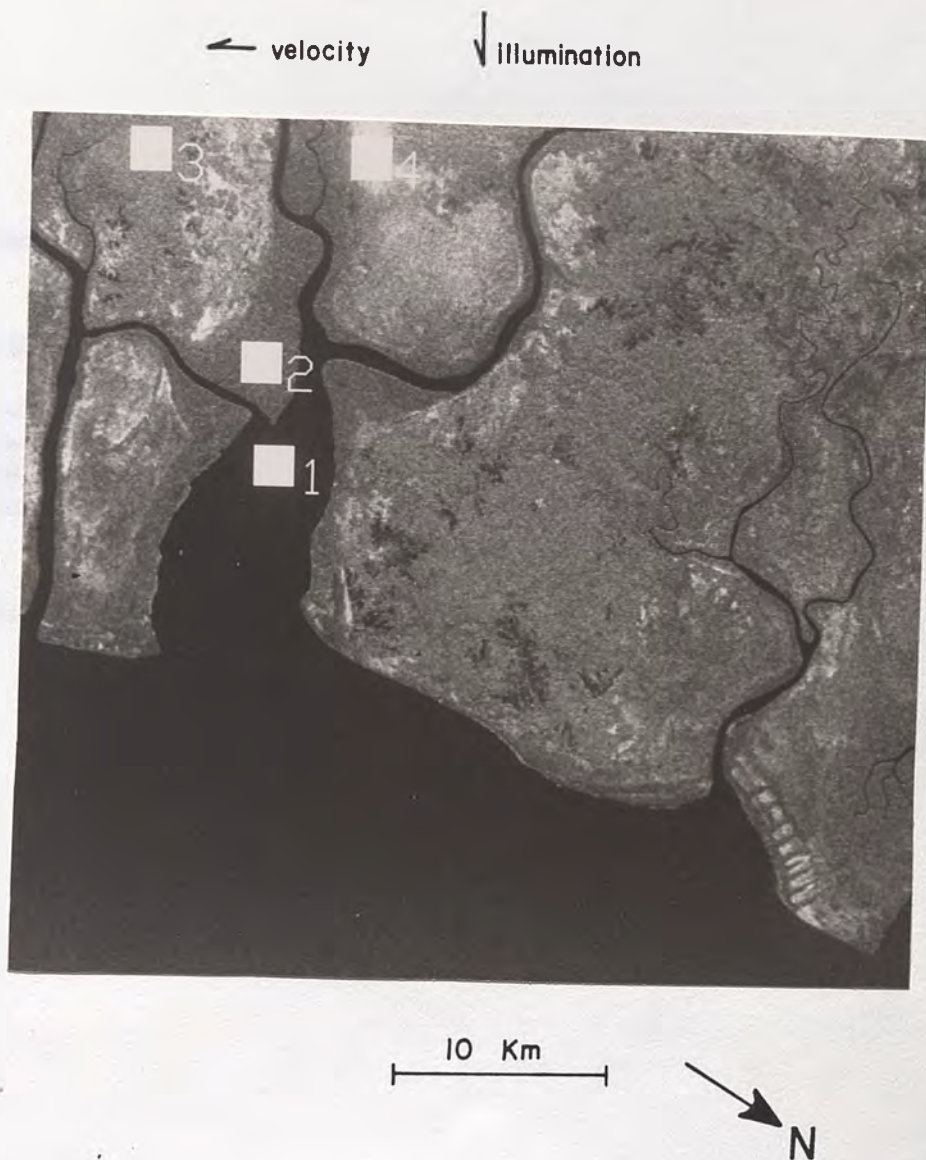


Figure 15. Training masks for water (1), tidal forest (2), coastal lowland forest (3), and swamp (4). After Miranda et al. (1990).

---

Surface cover type	DN Mean	DN Variance
Water	38.17	12.11
Tidal forest	83.58	85.43
Coastal lowland forest	110.81	131.25
Swamp	161.34	471.43

---

Table 1. Borneo image: statistical moments for water and vegetation training masks. After Miranda et al. (1990).

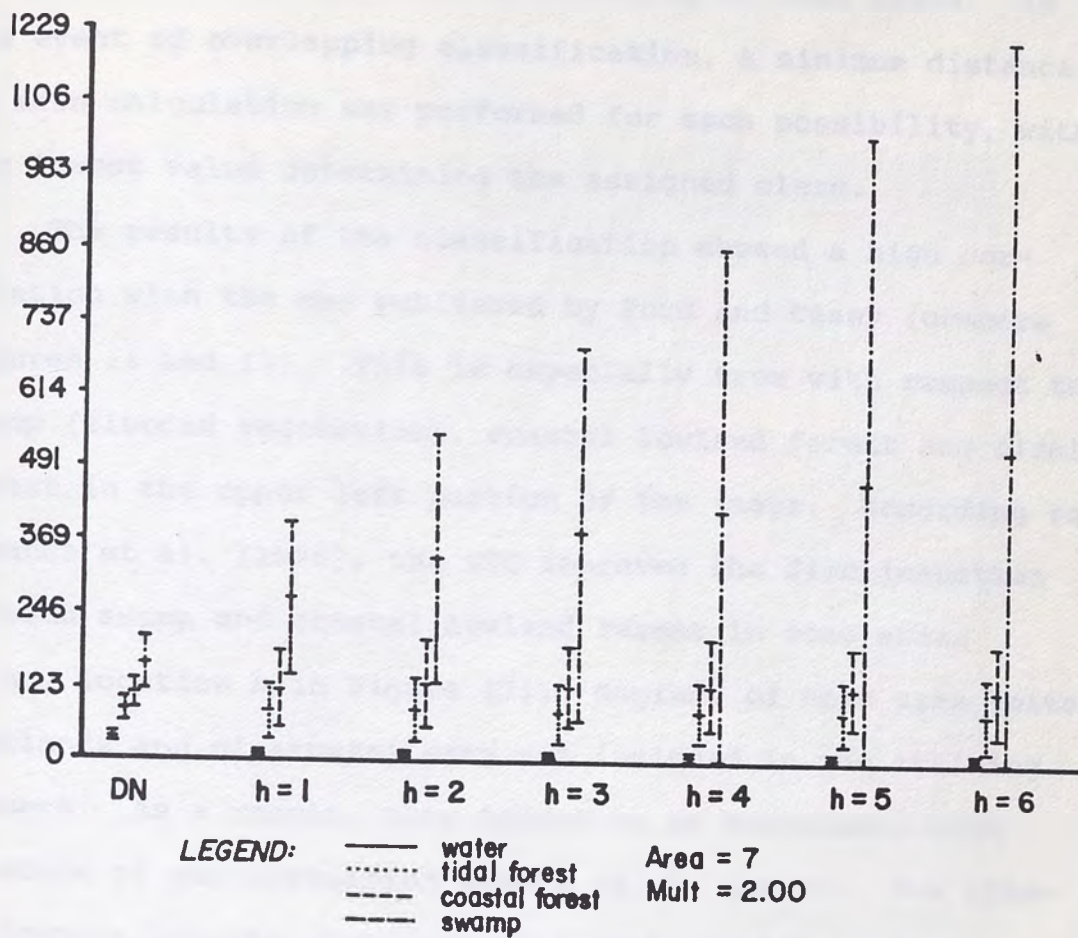


Figure 16. Borneo image: decision boundaries for parallelepiped classification (multiplier = 2.00). After Miranda et al. (1990).

then the pixel was defined as belonging to that class. In the event of overlapping classification, a minimum distance to mean calculation was performed for each possibility, with the lowest value determining the assigned class.

The results of the classification showed a high correlation with the map published by Ford and Casey (compare Figures 14 and 17). This is especially true with respect to swamp (flooded vegetation), coastal lowland forest and tidal forest in the upper left portion of the image. According to Miranda et al. (1990), the STC improved the discrimination between swamp and coastal lowland forest in some areas (e.g., location A in Figure 17). Regions of open area units (wetlands and clearcuts) were not included in the training process. As a result, they tended to be associated with clusters of non-classified pixels (B, C, and D). The classification results also suggested that coastal lowland forest and tidal forest occur interspersed with each other in the central portion of the image (E). This result was not portrayed in Ford and Casey's map. Water constituted the worst classification result of that study due to noise in the data. Increased local DN variance (as a result of noise) in the bottom portion of the image resulted in the misclassification of water as tidal forest (location F). Finally, Miranda et al., (1990) concluded that the STC is a

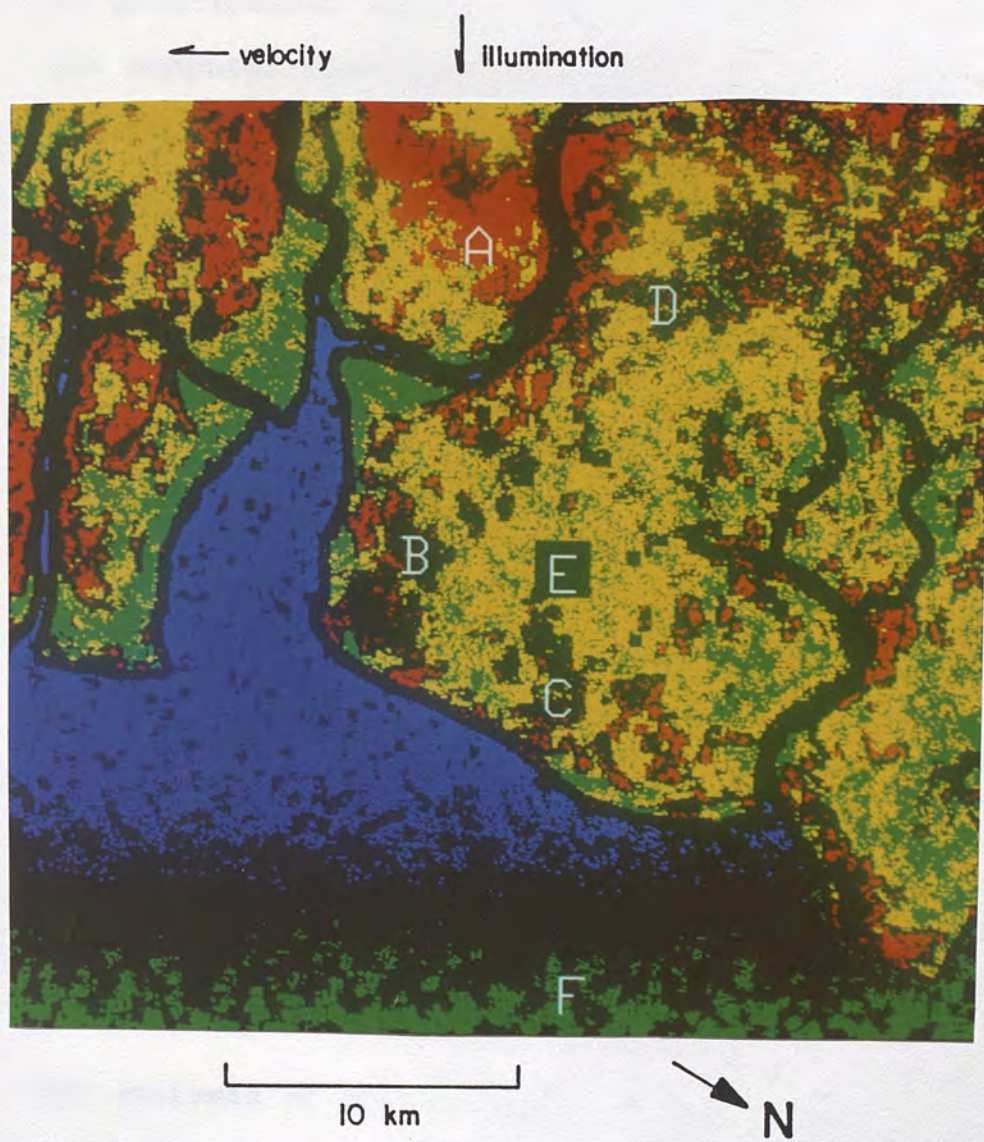


Figure 17. Borneo image: classification result. Water = blue, tidal forest = green, coastal lowland forest = yellow, swamp = red. After Miranda et al. (1990).

valuable tool for mapping rainforest environments using L-band/HH polarization spaceborne radars.

All computer programs used by Miranda et al. (1990) were written in Borland's Turbo Pascal 5.5 by John A. MacDonald and implemented on a 20 MHz 80386 based personal computer at the Mackay School of Mines. This software was utilized in the vegetation study of SIR-B data presented in Chapter 4.

#### REVIEW OF IDENTIFICATION OF GEOLOGIC FEATURES IN CRYSTALLINE BASEMENT TERRANES USING GREY-SCALE AEROMAGNETIC IMAGES

Grey-scale images depict aeromagnetic data in 256 brightness levels ranging from black (the lowest value) to white (the highest value). The images are usually displayed at small scales, so that as many features as possible show up hard-edged and photograph-like (Cordell and Knepper, 1987).

The analysis of aeromagnetic grey-scale images can reveal new information even in well studied areas. These products are especially suited to emphasize high-frequency features and to discriminate zones of anomalous signature.

With the aeromagnetic data in image format, a wide variety of digital processing techniques is available as an aid to interpretation. Edge enhancement and contrast

stretching are two possible examples. This approach is routinely used in remote sensing studies, but is seldom applied in potential field geophysics.

Cordell and Knepper (1987) displayed aeromagnetic data from the Rolla 1° by 2° quadrangle, Missouri, as a small-scale, grey tone image. It provided a clear picture of basement features beneath the sedimentary cover. Late-stage, tin-bearing granites of the Proterozoic St. François magmatic terrane were sharply outlined. The plutons averaged about 11 km in diameter and occupied 12 percent of the surveyed area. That study also revealed unreported magnetic patterns in the crystalline basement, possibly related to lead-zinc-copper mineralization in overlying carbonate strata of Cambrian age. Lack of confirmation of linear and curvilinear features previously interpreted from contour aeromagnetic maps showed that the improved high-frequency resolution of image data provided effective constraints on the delineation of anomaly edges and boundaries of signature zones.

The aeromagnetic data of the Guiana Shield were converted to a grey-scale image using software developed by the United States Geological Survey and implemented on a VAX 11/750 at the Branch of Geophysics, Denver. The procedures involved in the analysis of this data are discussed in Chapter 5.

REVIEW OF DELINEATION OF MAGNETIZATION UNITS IN  
CRYSTALLINE BASEMENT TERRANES USING A TERRACING OPERATOR

The terracing operator converts smoothly varying potential fields into a step function composed of flat segments separated by steeply dipping zones. Such a denomination is intended to evoke an image of rice-paddy terraces where, by an analogous process of cut and fill, originally smooth hillsides are similarly transformed (Cordell and McCafferty, 1989). For a complete description of data processing procedures pertaining to the terrace method see Phillips (1990).

The terracing operation is an iterative process that seeks to define abrupt boundaries between homogeneous domains. Transitional borders are inadmissible. The results have discontinuous first derivatives and cannot be depicted as contour lines (they are only displayed by color levels). The magnetization distribution obtained by the terracing method is not necessarily an "equivalent source". Therefore, forward calculations based on such a distribution may not give rise to an exact fit with the observed data (Cordell and McCafferty, 1989).

The terrace method yields a highly useful geologic-like map, where structural features and magnetization units within the magnetic basement are outlined. This is an invaluable product for the study of (1) Precambrian crystal-



line terranes covered by flat-lying sedimentary sequences, and (2) tropical rainforest shield areas where outcrops are scarce. Examples of geologic applications of this technique are discussed in the following paragraphs.

The terracing operator was applied separately to aeromagnetic and gravity data from a 136 km by 123 km area in eastern Kansas (Cordell and McCafferty, 1989). The region consists of undisturbed Paleozoic strata overlying a Proterozoic crystalline basement (granites and rhyolites of 1.35-1.40 b.y. age). Supracrustal metamorphic rocks as old as early Proterozoic have also been drilled in some places. The basement is about 1000 meters deep and has no more than a few hundred meters of local topographic relief. Results provided a reasonably good physical representation of both gravity and aeromagnetic information. Superposition of terrace maps from the two data sets showed many areas of agreement that were referenced to geologic features within the buried Precambrian crystalline terranes. The emerging picture of basement geology was much better portrayed if compared with the interpretation derived either from the scanty available drill data or from the visual inspection of gravity and aeromagnetic contour maps.

The United States Geological Survey maintains a resident advisory group in Venezuela as part of a cooperative project. One of the objectives of such an enterprise is to

apply state-of-the-art technology to mineral exploration in the Venezuelan portion of the Guiana Shield (Wynn et al. 1989). As much as 25% of the aeromagnetic data available in this region may be found in digital form. The remainder is constituted by published contoured maps or analog records. With hand-contoured data, subjective interpretation is usually the only kind of analysis that can be done. While not completely satisfactory, it provides information about the location of discrete geologic bodies and about boundaries between different magnetic terranes. Despite these limitations, a single quadrangle at 1:50,000 scale covering the Bochinche area (eastern Bolivar State) was chosen by Wynn et al. (1989) for manual digitization. A terrace map was one of the products derived from the digitized data. It allowed the identification of many discrete geologic structures. Their boundaries were defined much more precisely in the terrace map than in the original contoured data. The terrace map was divided into 13 different levels of modeled magnetization contrast, expressed in terms of  $\text{emu.cm}^{-3}$  (cgs system). Such a representation provided useful insights to geologic mapping in that Precambrian area characterized by sparse outcrops and nearly 100% forest cover.

A terrace map of the Guiana Shield digital aeromagnetic data was produced using software developed by the United States Geological Survey. Such programs are implemented on

a VAX 11/750 at the Branch of Geophysics, Denver. The procedures involved in this analysis are discussed in Chapter 5.

#### ANALYSIS AND INTEGRATION OF SPACEBORNE RADAR AND AEROMAGNETIC DATA: SUMMARY OF PROCEDURES

The research was performed according to the following steps:

- (1) Discrimination and mapping of standing water beneath canopy layers on the SIR-B image using the semivariogram textural classifier (STC). Flooded vegetation was considered indicative of subtle topographic relief (up to 8 m );
- (2) Identification of linear geomorphic features based on the spatial distribution of STC-mapped flooded vegetation;
- (3) Identification of tonal linear features on the TLM-stretched SIR-B image. Special interest was devoted to (a) individual linear features developed on an uniform background, and (b) linear stream channels with bright radar signatures associated with forested floodplains;
- (4) Development of a map of SIR-B linear features including (a) linear geomorphic features defined on the basis of

- the spatial distribution of flooded vegetation, and (b) tonal linear features;
- (5) Production of a grey-scale image of reduced-to-pole magnetic anomalies, in order to highlight zones of distinct magnetic signature;
  - (6) Production of a terrace-magnetization map that delineates induced magnetization boundaries and theoretically outlines geologic structures and varying magnetic terranes;
  - (7) Production of a map showing the location of maximum values of the horizontal component of the pseudogravity gradient (boundary lines). They represent abrupt lateral changes in magnetization that are interpreted as steep structural or lithologic contacts;
  - (8) Comparison of aeromagnetic and SIR-B interpretation results with the geologic data acquired in the field by the RADAMBRASIL Project. Geologic structures and broad terrane categories were delineated for the first time as a result of this comparison. RADAMBRASIL field samples showed similar petrographic characteristics within specific terrace-magnetization units. Areas of agreement between magnetization boundary lines and SIR-B linear features were interpreted as structural discontinuities in the magnetic basement having topographic expression.



## CHAPTER IV

## SPACEBORNE RADAR ANALYSIS

This chapter presents the results of the SIR-B image analysis, which was performed in the initial stages of the research (i.e., prior to the interpretation of aeromagnetic data and without any information about the surface geology of the study area). The main topics to be discussed are (a) discrimination of vegetation types and water bodies using the semivariogram textural classifier (STC); (b) identification of tonal linear features using a contrast stretching technique; and (c) development of a map of SIR-B linear features.

## CHARACTERISTICS OF SIR-B DATA

In 1984, the Shuttle Imaging Radar-B (SIR-B) acquired digital data over an inaccessible, heavily-vegetated and generally cloud-covered region of the Guiana Shield in northwestern Brazil (Figures 1 and 18; Table 2). Available natural resource information in this area is limited to a reconnaissance survey conducted by the RADAMBRASIL Project at a 1:1,000,000 scale with the aid of X-band SLAR imagery. Digital conversion and subsequent quantitative analysis of this analog airborne data set is not a feasible task. It is very difficult to correlate tonal information between

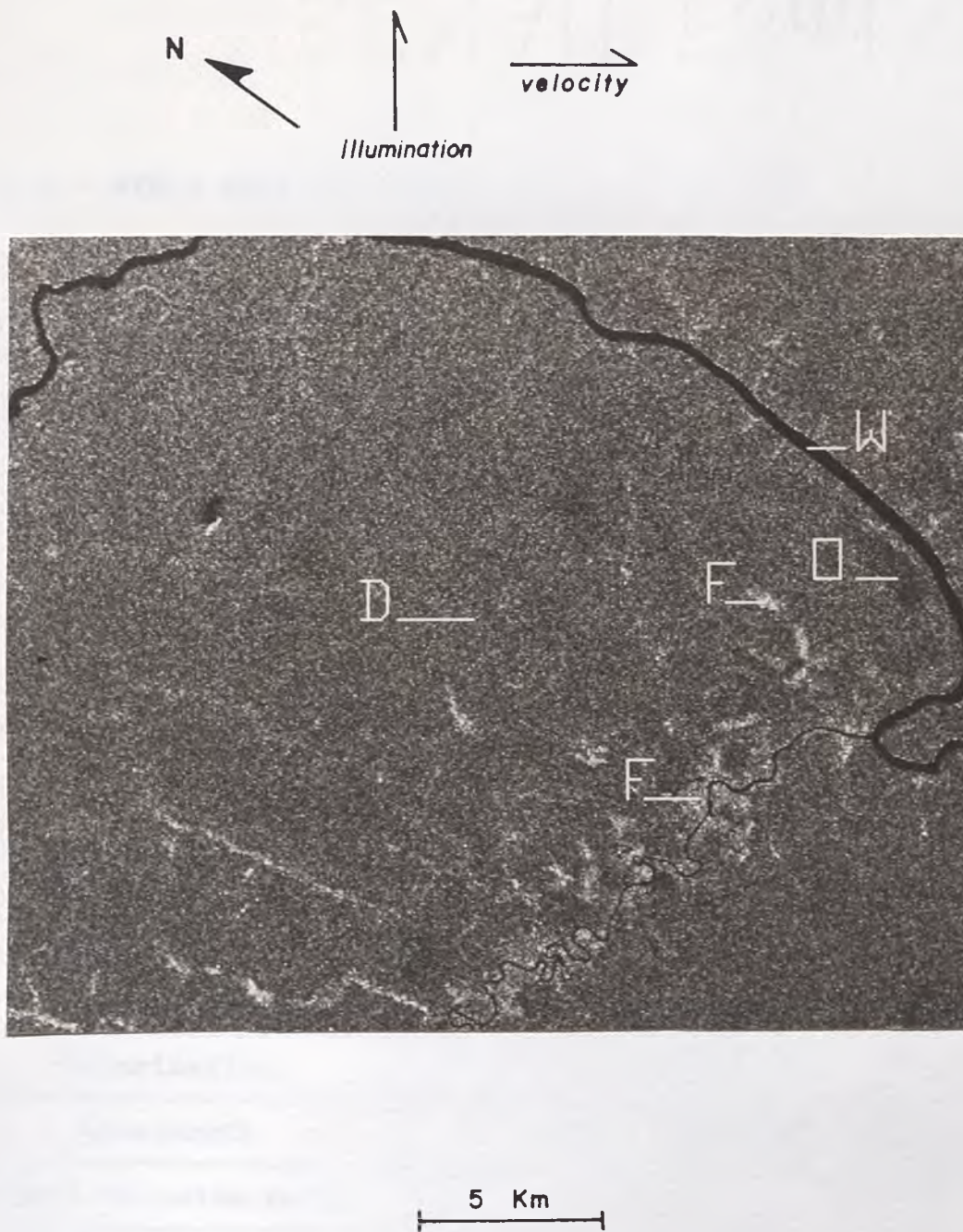


Figure 18. SIR-B image of the study area, Guiana Shield, Brazil (data take MC 118.30; portion of scene 107). Raw data. Image size is 1862 by 2268 pixels. W=water; O = open vegetation; D = dense vegetation, and F = flooded vegetation.

Table 2. SIR-B data characteristics in the study area.

Data take	MC-118.30
Scene	107
Center latitude/longitude	0° 58.0' (N) / 67° 36.0' (W)
Swath width	25 km
Sampling	5 BPS (bits per sample)
Track	147.0° (to true north)
Look direction	N 57° E
Center incidence angle	35.7°
Center resolution	24.1 m (Range) X 29.5 m (Azimuth)
Pixel size	12.5 m
Polarization	HH
Wavelength	23.4 cm (L-band)
Signal to noise ratio	8.91 dB
Number of looks	4



distinct radar strips due to differences in photographic processing (Correa, 1979).

The acquisition of SIR-B data over northwestern Brazil was hindered by arcing in the antenna feed, resulting in a reduction of swath width and image contrast (Elachi et al., 1986). In addition, the Guiana Shield was imaged using only a single incidence angle (as opposed to multiple incidence angles as initially planned), which prevented stereo investigations. In spite of these inadequacies, the digital analysis of SIR-B data provided excellent results in the study area.

A further comment about the Guiana Shield SIR-B data refers to speckle, which can be described as the granular noise associated with imaging radars. It is expressed as random high and low intensity pixels on the image (Mueller and Hoffer, 1989). Skolnik (1980) states that constructive and destructive interference result in a breakup of distributed scatterers, causing the speckled appearance of radar imagery. There are two general ways of suppressing radar speckle: pre-image correlation (multi-look approach) and post-image correlation (low-pass spatial filtering). SIR-B image contrast in the Guiana Shield is already reduced due to problems in data acquisition. The application of low-pass filters to minimize speckle noise would make image interpretation extremely difficult. Therefore, only multi-

look processing (4-look imagery) was used in order to reduce speckle on the SIR-B data of the Guiana Shield.

#### DISCRIMINATION OF VEGETATION TYPES AND WATER BODIES USING THE SEMIVARIOGRAM TEXTURAL CLASSIFIER (STC)

Within the study area, the backscattered energy measured by the SIR-B antenna is primarily influenced by the following environmental conditions:

- (1) the topography is predominantly flat as a result of extensive erosion, hence there is a negligible modulation of the radar backscatter by slope effects;
- (2) the cover types are exclusively composed of vegetation and water, with a complete lack of consolidated and unconsolidated rock cover, soil cover and cultural features.

The SIR-B ground resolution cell in the investigation site measures about 24 m in the range direction by 30 m in the azimuth direction (Table 2). At this resolution, the sensor does not resolve individual trees. The digital number (DN) assigned to each pixel is a scaled representation of the integrated backscatter from the canopy within a single ground resolution cell (Ford and Casey, 1988).

Vegetation units were visually distinguished on the SIR-B image as groups of pixels with similar DN values over extended areas (Figure 18). They were designated as (a) dense

vegetation, (b) open vegetation, and (c) flooded vegetation. Water was included as an additional surface cover type.

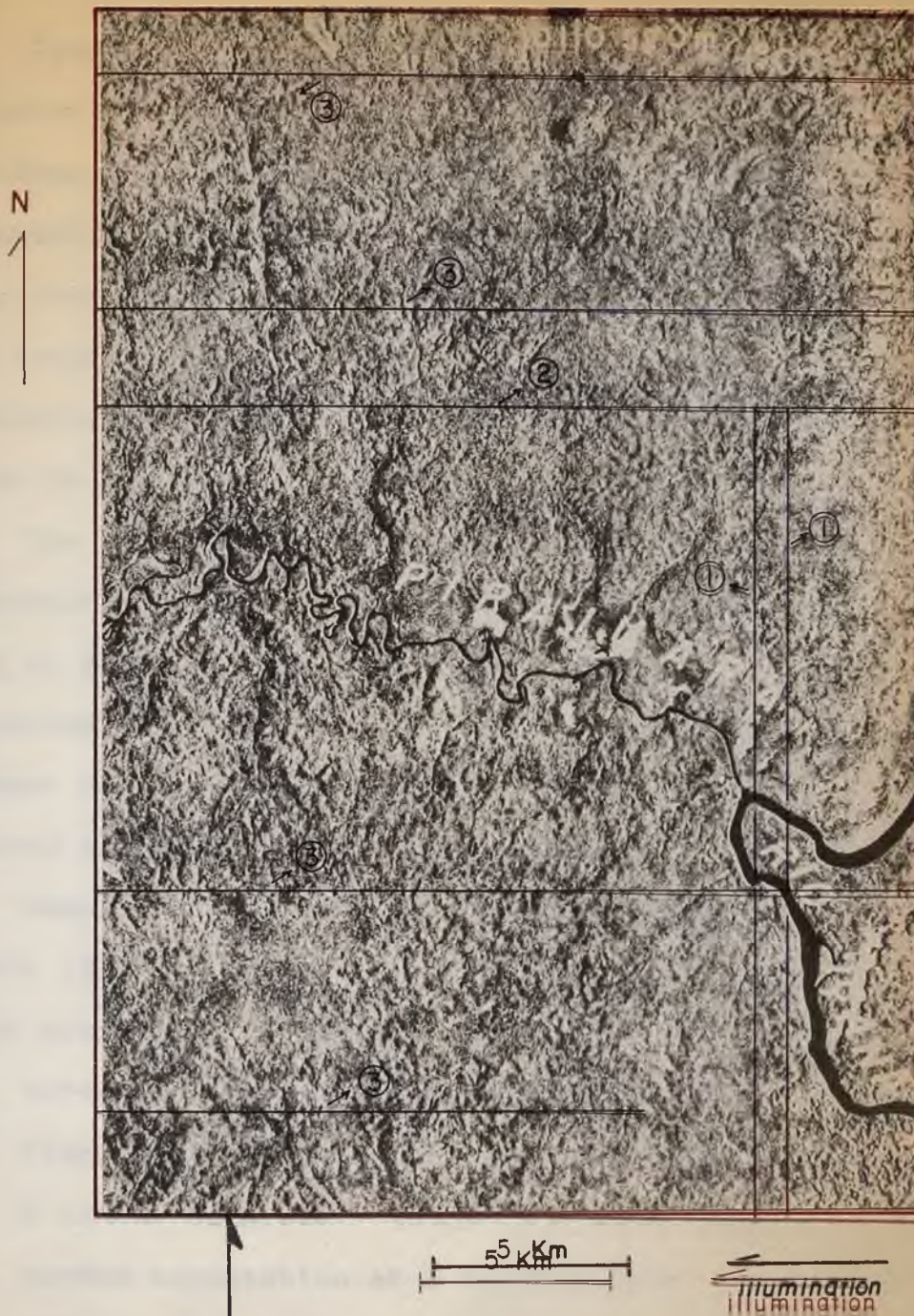
Water constitutes smooth surfaces of mostly specular reflection. It consists of very low DN values on the SIR-B image. Backscatter from dense vegetation is considered to be predominantly diffuse. In fact, previous radar observations of deciduous forests have indicated that microwave energy at L-band with HH polarization is scattered back diffusely from stems and branches (Sieber, 1985). It is also assumed in this study that the relatively thinner and more sparse canopy of the open vegetation unit produces lower levels of diffuse backscatter (and therefore lower DN values than dense vegetation). Flooded vegetation presents the strongest backscatter in the investigated area (high DN values; see Figure 18). The SIR-B scene shows that brighter image tones outline the floodplains of some streams. This occurs due to the presence of standing water below the canopy in the floodplains, as suggested by the idealized profile of Figure 19.

Previous studies have indicated that standing water beneath a canopy strongly reinforces backscatter at L-band, HH polarization radar images (MacDonald et al., 1980; Waite et al., 1981; Krohn et al., 1983; Ormsby et al., 1985; Place, 1985; Hoffer et al., 1986; Imhoff et al., 1986; Richards et al., 1987; Ford and Casey, 1988; Imhoff and



Gesch, 1990; Hess et al., 1990). The reinforcement has been shown to come from an additional component of microwave energy that penetrates vegetation and is returned by double forward reflection at the smooth interface beneath the canopy layers (Engheta and Elachi, 1982).

According to Ford and Casey (1988), vegetation is more deeply penetrated at longer wavelengths (L-band). The radar energy at shorter wavelengths (X-band) is more attenuated in the upper part of the canopy. This difference in penetration capability was verified by Ford and da Cunha (1985) at the intersection of SIR-A data takes 24C and 31 (Santa Helena and Taxidermista rivers; Amazonian region of Brazil). In this area, which is underlain by a Precambrian basement complex, alluvial forest associated with floodplains appeared very bright on SIR-A images (L-band, HH polarization). Corresponding RADAMBRASIL data (X-band, HH polarization) showed no significant tonal differences along floodplains and failed to discriminate areas of alluvial forest. The same result was obtained by Ford and da Cunha (1985) at the intersection of SIR-A data takes 24C and 34 (Rio Negro forest reserve; northern Brazil). In the Guiana Shield, RADAMBRASIL mosaics also failed to discriminate areas of flooded forest associated with tributaries of the Piraiauara River (Figure 20). Conversely, such features are remarkably portrayed in the corresponding SIR-B image (compare Figures 18 and 20).



Artifacts:

- ① Fine lines along azimuth direction
- ② Radar strips separated by a straight line

Figure 29. Strong banding along range direction and image showing the confluence of Piraiuara and Içana Rivers.



Figure 20. RADAMBRASIL X-band image showing the confluence of Piraiauara and Içana Rivers.

Data sets for semivariogram calculations (hereafter referred to as training masks) were extracted from selected portions of the SIR-B image considered to be representative of specific vegetation units (Figures 21 and 22). Water was also included in such a semivariogram analysis. The size of all training masks is 22 by 22 pixels. Histograms and DN statistics (mean and variance) for the training masks are shown in Figure 23.

The semivariogram calculations used in this study are isotropic and hence contain no directional information. This is done by computing the semivariogram value for every direction and grouping separation distances into their integer parts (e.g., a separation distance of 3.7 is considered as 3).

Results obtained for separation distances up to 22 pixels (Figure 24) indicate that each cover type in the study area has a distinctive semivariogram:

- (1) water: the semivariogram for water is essentially flat, exhibiting behavior similar to that expected for a random data set. There is a small drop from the random expectation at a separation of 1 pixel, but for greater lag distances the semivariogram has only minor fluctuations around the estimated sill;



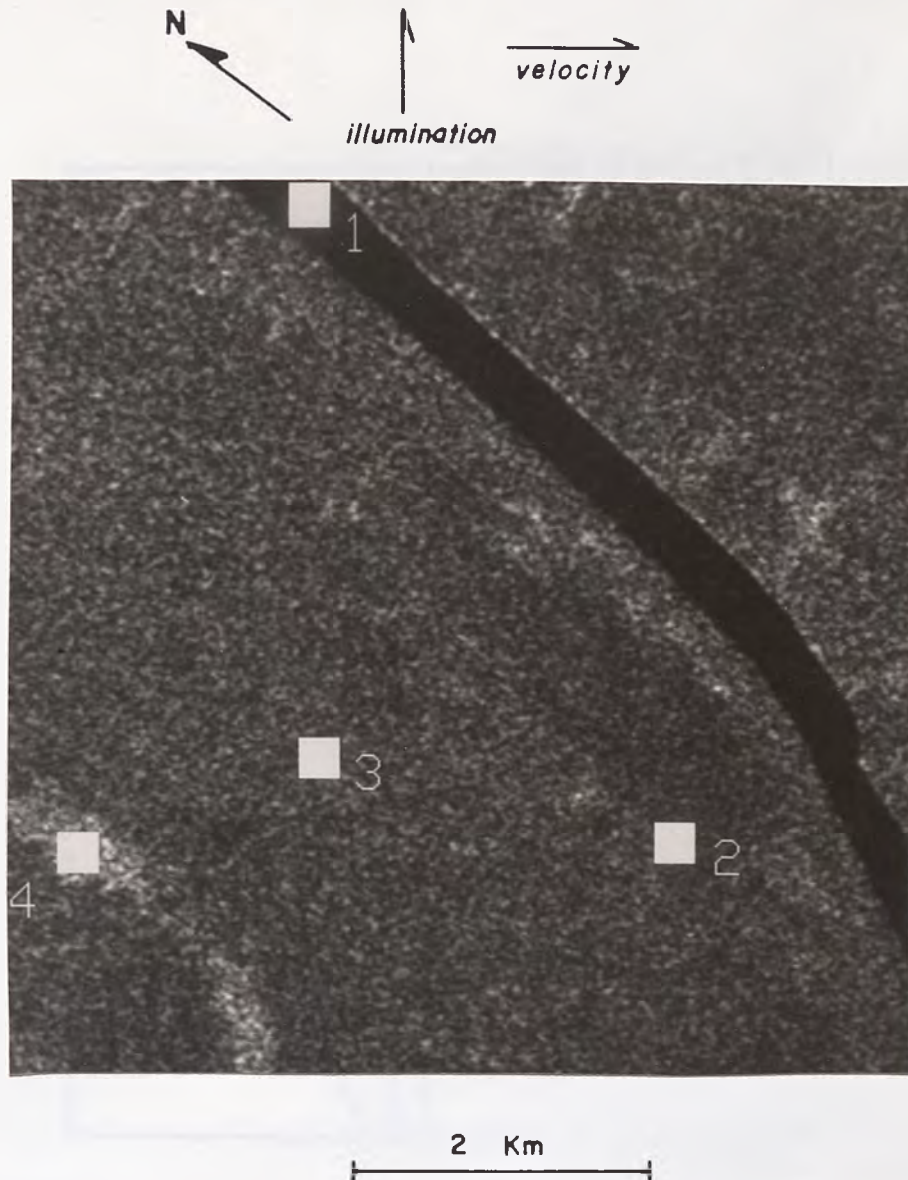


Figure 21. Training masks for water (1), open vegetation (2), dense vegetation (3), and flooded vegetation (4). Training masks are 22 by 22 pixels large. Image size is 480 by 512 pixels. See Figure 22 for location.

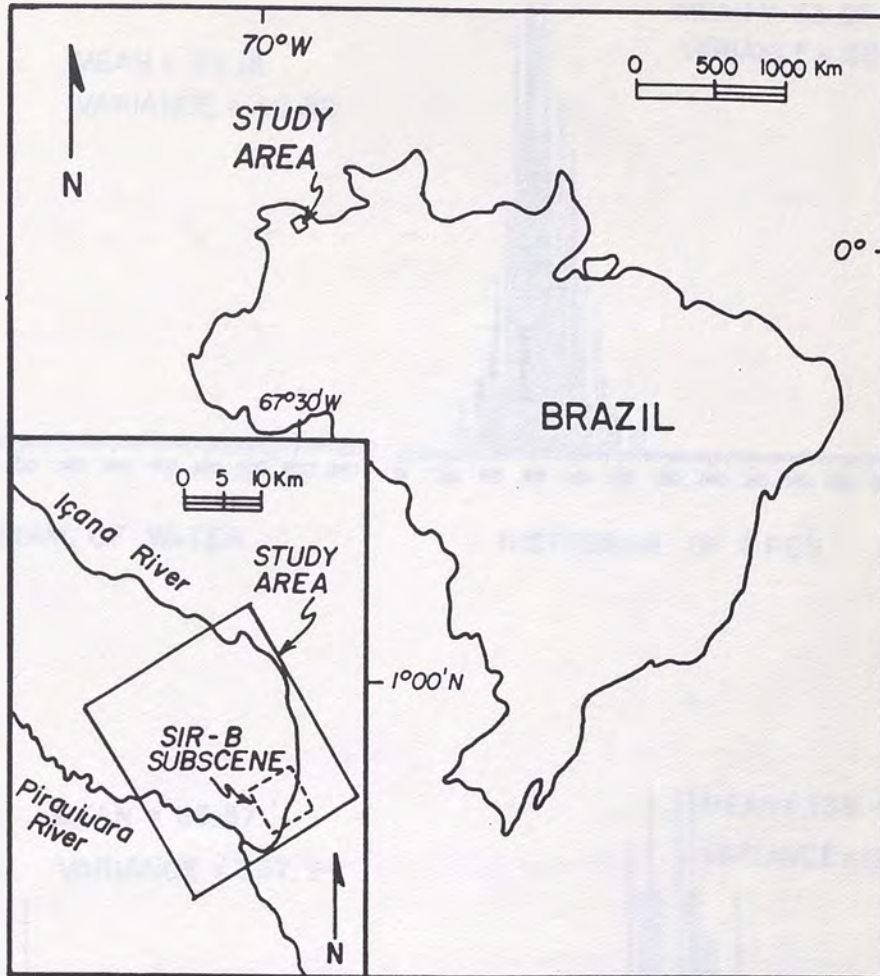


Figure 22. Location map of the SIR-B subscene where training masks were selected.

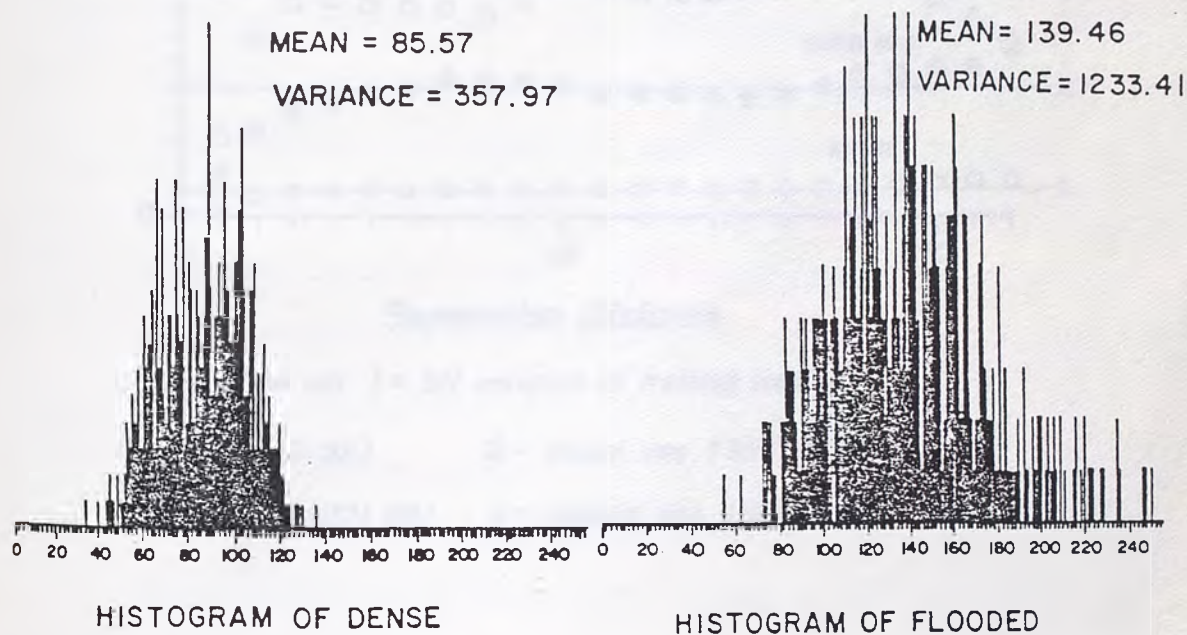
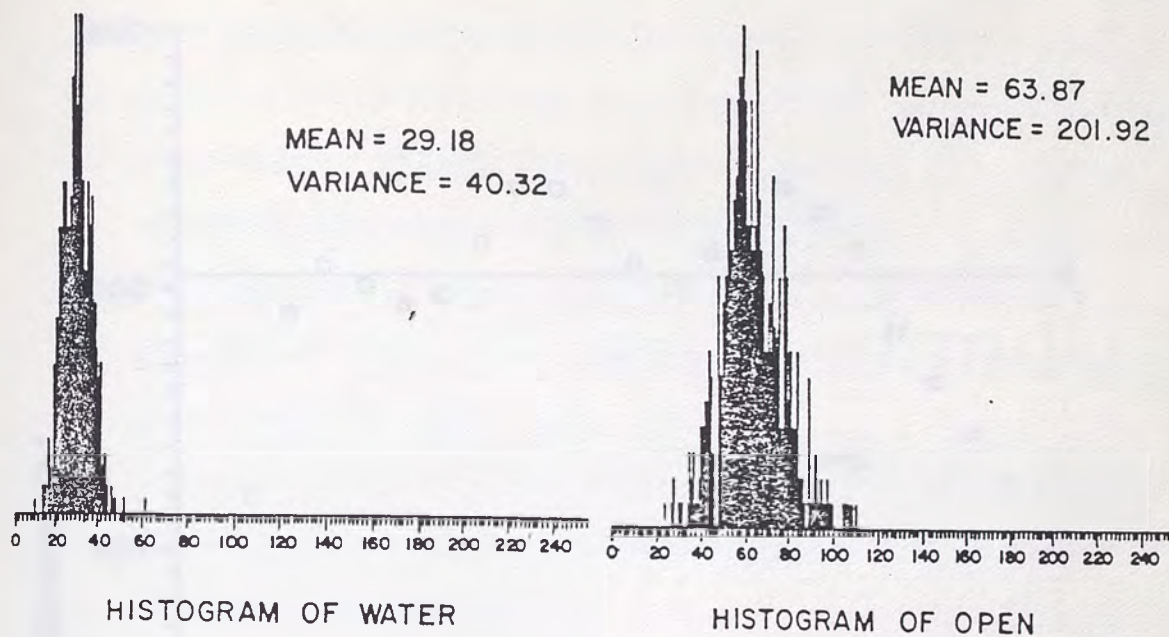
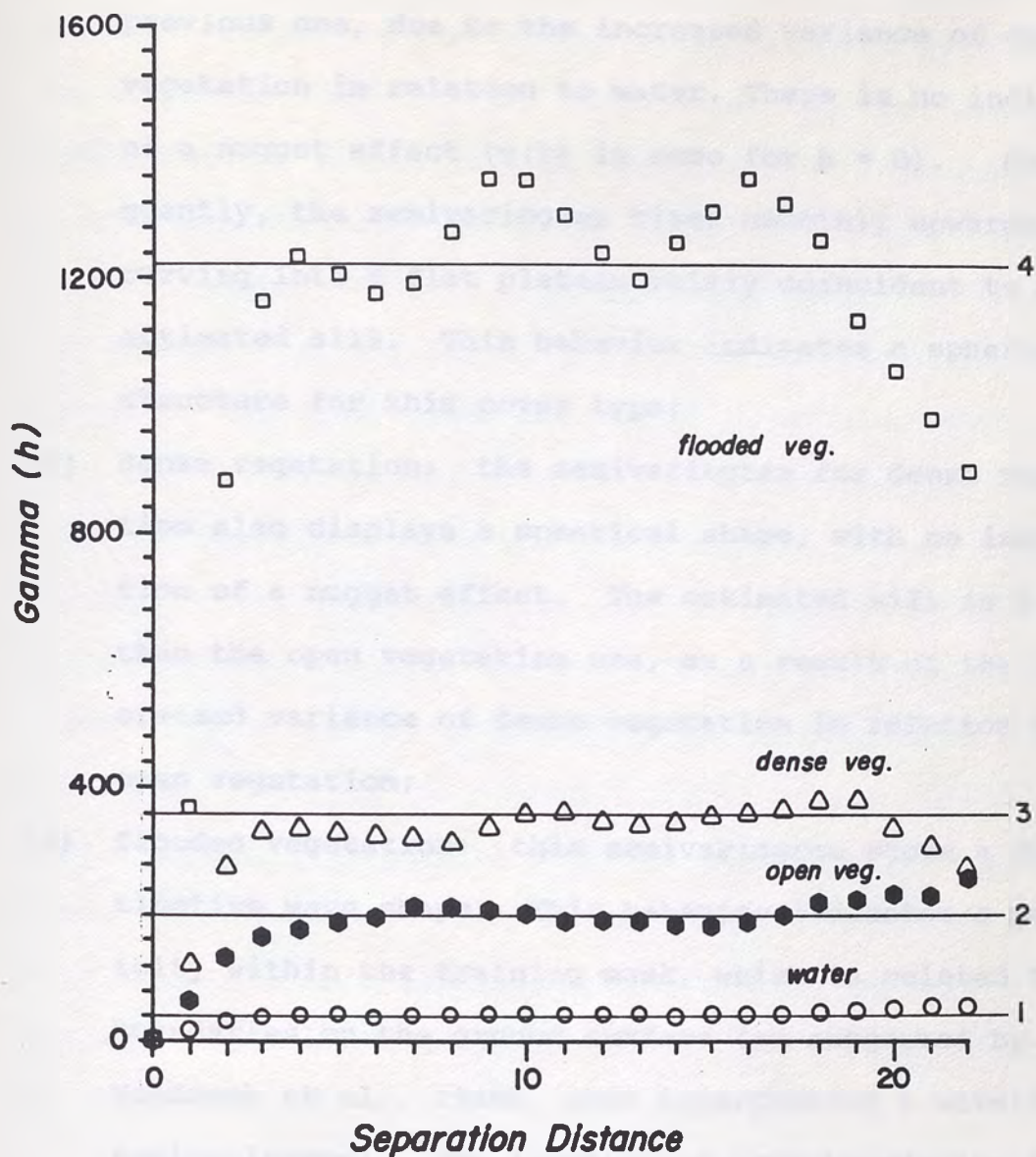


Figure 23. Histograms and DN statistics of Guiana Shield training masks.



Estimated sill (= DN variance of training mask)

1- water (40.32)

3- dense veg (357.97)

2- open veg. (201.92)

4- flooded veg. (1233.41)

Figure 24. Semivariograms of Guiana Shield training masks.

- (2) open vegetation: this semivariogram is higher than the previous one, due to the increased variance of open vegetation in relation to water. There is no indication of a nugget effect ( $\gamma(h)$  is zero for  $h = 0$ ). Subsequently, the semivariogram rises smoothly upwards, curving into a flat plateau fairly coincident to the estimated sill. This behavior indicates a spherical structure for this cover type;
- (3) dense vegetation: the semivariogram for dense vegetation also displays a spherical shape, with no indication of a nugget effect. The estimated sill is higher than the open vegetation one, as a result of the increased variance of dense vegetation in relation to open vegetation;
- (4) flooded vegetation: this semivariogram shows a distinctive wave shape. This behavior indicates a periodicity within the training mask, which is related to boundaries on the ground surface (as suggested by Woodcock et al., 1988b, when interpreting a wavelike semivariogram). The location of such boundaries is possibly controlled by the spatial distribution of standing water beneath the canopy. Flooded vegetation presents the highest variance among the cover types of the study area (Figure 23). This is why it is associated with the highest values of  $\gamma(h)$  in Figure 24.

Differences in semivariogram behavior within the SIR-B image of the Guiana Shield were first reported by Miranda and MacDonald (1989). They recommended the application of geostatistical classification techniques to this data set, since significantly distinct cover types presented unique semivariograms. In fact, the results obtained by Miranda and MacDonald (1989) provided the motivation for the development of the semivariogram textural classifier (STC).

The STC was employed in this research to discriminate and map vegetation units and water bodies. As discussed in Chapter 3, the classification process consists of two major subprocesses: training and classification. The training masks used in the training subprocess were the ones shown in Figure 21. The STC calculated a semivariogram within a moving window (7x7 pixels) for each pixel in each training mask. This procedure resulted in a mean and standard deviation value for each separation distance (up to six) in each class. A mean and a standard deviation were also calculated for the DN values of each class (Table 3).

The classification subprocess began with the definition of a parallelepiped (PPD). The PPD established boundary conditions for each class (Figure 25) based upon a multiple of the standard deviation from the mean (in this study, such a multiplier was 1.00). Then, beginning in the upper left corner of the scene, a semivariogram was calculated for the



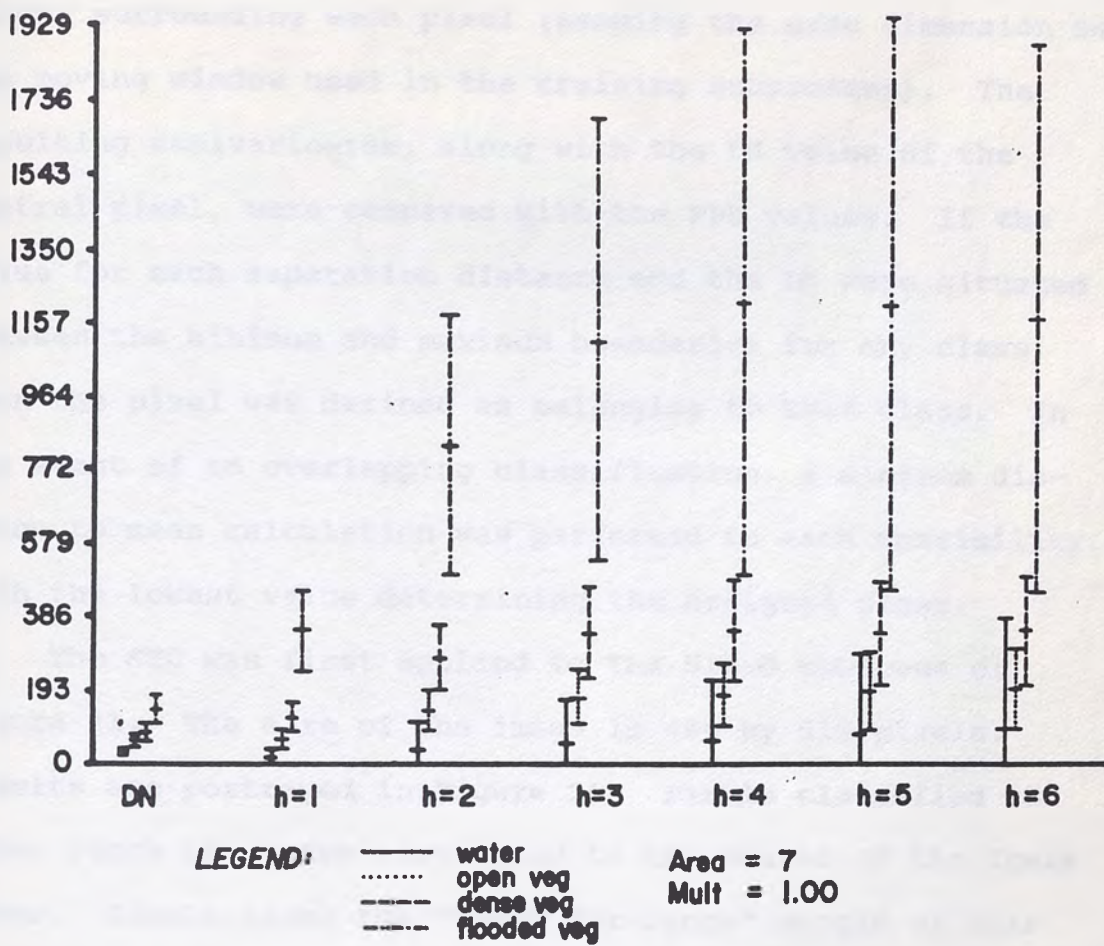


Figure 25. Guiana Shield image: decision boundaries for parallelepiped classification (multiplier = 1.00).



window surrounding each pixel (keeping the same dimension as the moving window used in the training subprocess). The resulting semivariogram, along with the DN value of the central pixel, were compared with the PPD values. If the value for each separation distance and the DN were situated between the minimum and maximum boundaries for any class, then the pixel was defined as belonging to that class. In the event of an overlapping classification, a minimum distance to mean calculation was performed to each possibility, with the lowest value determining the assigned class.

The STC was first applied to the SIR-B subscene of Figure 21. The size of the image is 480 by 512 pixels. Results are portrayed in Figure 26. Pixels classified as water (dark blue) are restricted to the course of the Içana River. Pixels along the "radar far-range" margin of this river are classified as flooded vegetation (e.g., location A in Figure 26). This is possibly caused by radar reflections off the water surface in the river onto the trees on the river margin and back to the SIR-B antenna (double-bounce effect). This effect is not observed along the opposite ("near range") margin. Locations B and C represent areas of predominantly open vegetation. This cover type also occurs interspersed with dense vegetation (E). Flooded vegetation outlines the alluvial plain of a stream in the lower left bottom of the image (D). It is interesting to note the

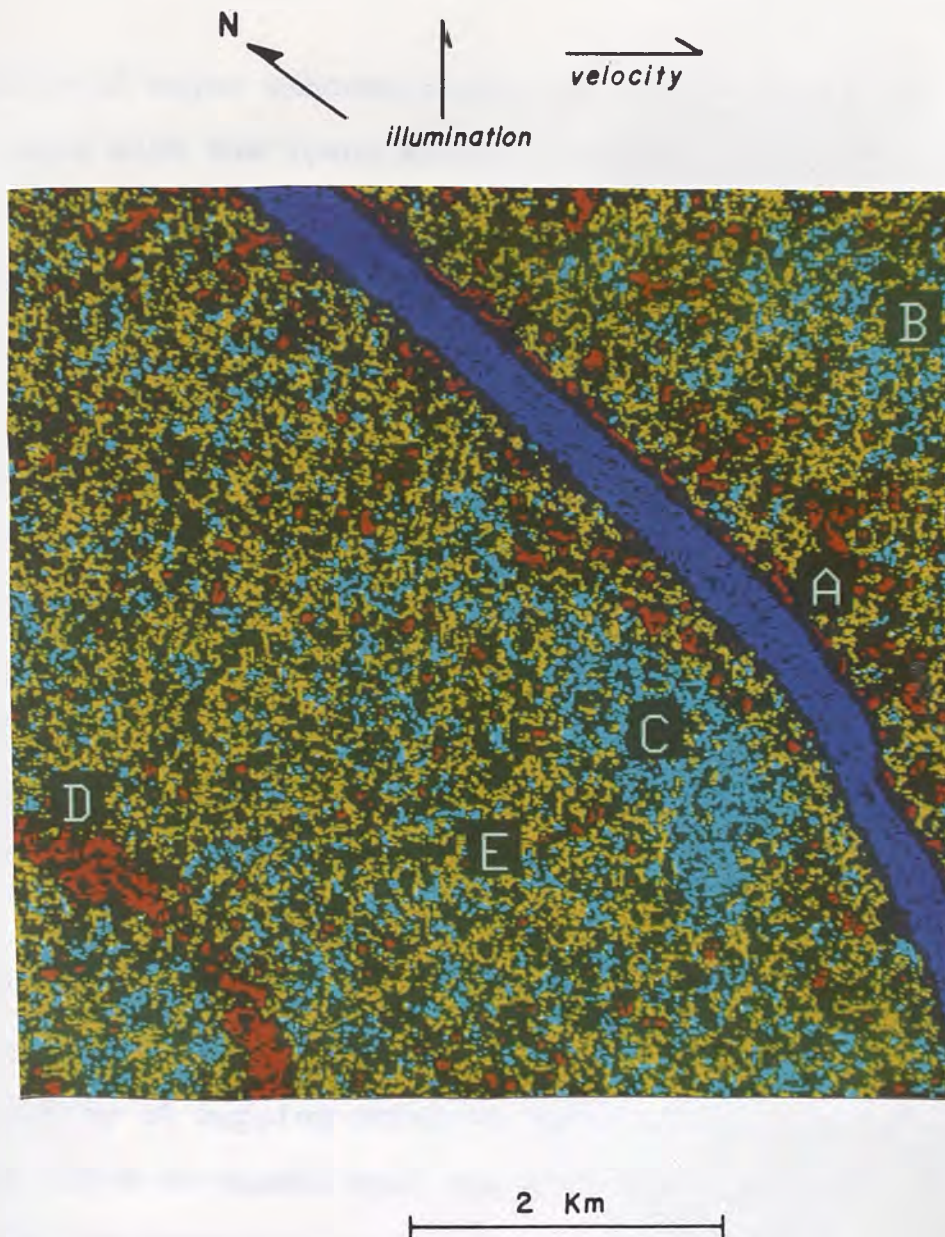


Figure 26. Guiana Shield: classification results including all classes. Image size is 480 by 512 pixels (for location see Figure 22). Water = dark blue; open vegetation = light blue; dense vegetation = yellow, flooded vegetation = red. See text for explanation about A, B, C, D, and E.

absence of major concentrations of flooded vegetation associated with the Içana River. Unclassified pixels (black) are randomly distributed through the image. This means that their spatial disposition does not provide any additional information about the cover types of the area being studied.

Areas of interspersed open and dense vegetation in Figure 26 are tentatively associated with dense campinarana typical of watersheds. Zones of predominantly open vegetation are interpreted as areas of highly leached soil where the campinarana has a relatively thinner and more sparse canopy. Flooded vegetation on the SIR-B image is related to dense campinarana with alluvial influence and standing water beneath the canopy.

The objective of SIR-B data analysis is to display landscape patterns indicative of subtle structural features in the crystalline terranes of the Guiana Shield. The capability of mapping standing water beneath canopy layers makes SIR-B an useful tool for geomorphic studies in relatively flat, heavily-vegetated areas. It is considered in this research that water and flooded vegetation are the key cover types for the recognition of minor topographic differences (up to 8 m) in the investigated area. With such an assumption in mind, the STC was applied to the SIR-B image that embraces the study site (Figure 18). The size of this data set is 1862 by 2268 pixels. Classification results

including only water and flooded vegetation are shown in Figure 27. Geomorphologic information obtained with this procedure can be described as:

- (1) the course of the Içana River is perfectly outlined by pixels classified as water (compare Figures 18 and 27). Conversely, only few pixels along the Piraiauara River are ascribed to this cover type. Recall that during classification a semivariogram was calculated for a 7 by 7-pixels window surrounding each pixel. Because the Piraiauara River is narrow, contamination within the moving window by non-water pixels was severe;
- (2) flooded vegetation conspicuously outlines the alluvial plain of the Piraiauara River. The same does not happen with the Içana River. This is consistent with the hypothesis that such a river is actively downcutting the bedrock, as a result of the southward tilting of the Rio Branco-Rio Negro Pediplane. The area along the Piraiauara River may be acting as a local hinge line;
- (3) a very subtle topographic high subparallel to the course of the Piraiauara River is defined by the spatial distribution of flooded vegetation. Location A in

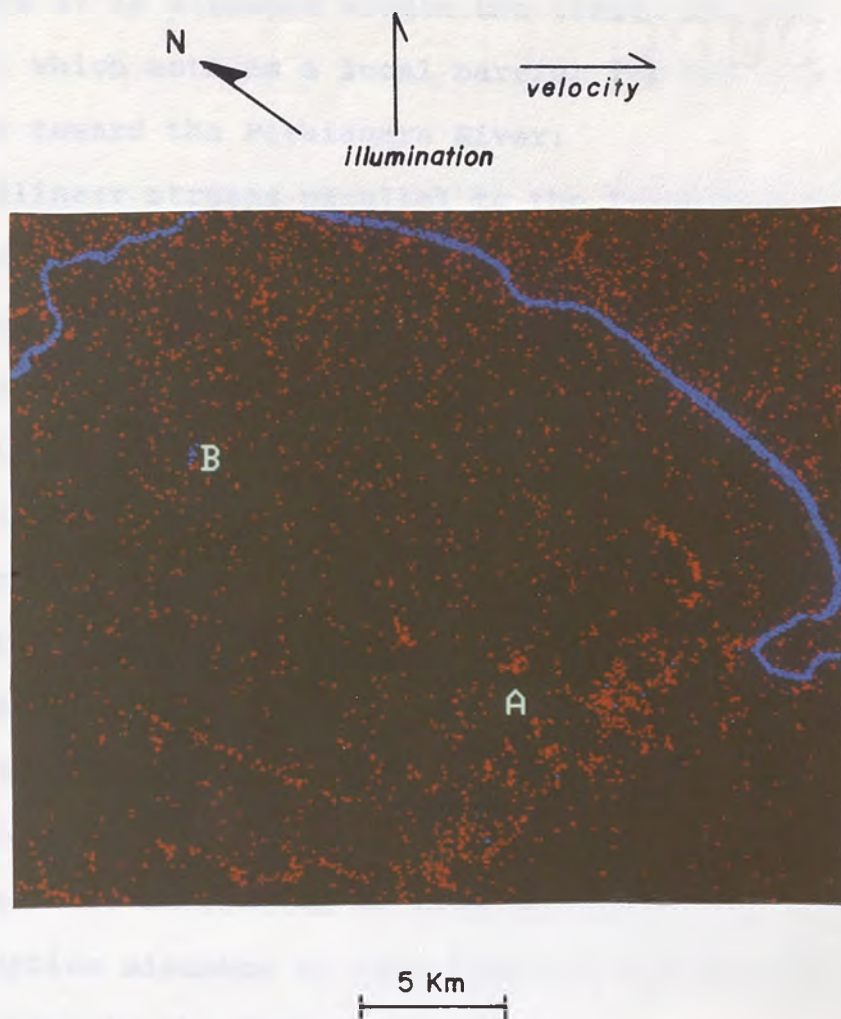


Figure 27. Guiana Shield: classification results including only two classes (water and flooded vegetation). Image size is 1862 by 2268 pixels. Water = blue; flooded vegetation = red. See text for explanation about A and B.

Figure 27 is situated within the limits of this feature, which acts as a local barrier for the flow of water toward the Piraiauara River;

- (4) rectilinear streams parallel to the Içana River are noticeable in the lower left bottom of the image (Figure 27). These streams are offset by linear drainage segments oriented in the same direction of the Piraiauara River;
- (5) location B in Figure 27 refers to the only prominent positive topographic feature in the study site (an inselberg). Several pixels in this place are misclassified as water. They actually correspond to radar shadow (slopes facing away the radar antenna). Slopes facing the radar beam have high DN values and are erroneously attributed to flooded vegetation. Classification mistakes of this kind are unlikely to occur elsewhere in the investigated area.

Geomorphologic information derived from the STC-mapped landscape patterns (flooded vegetation and water ) was utilized in the development of a map of linear geomorphic features (Figure 28). These features are described as follows:

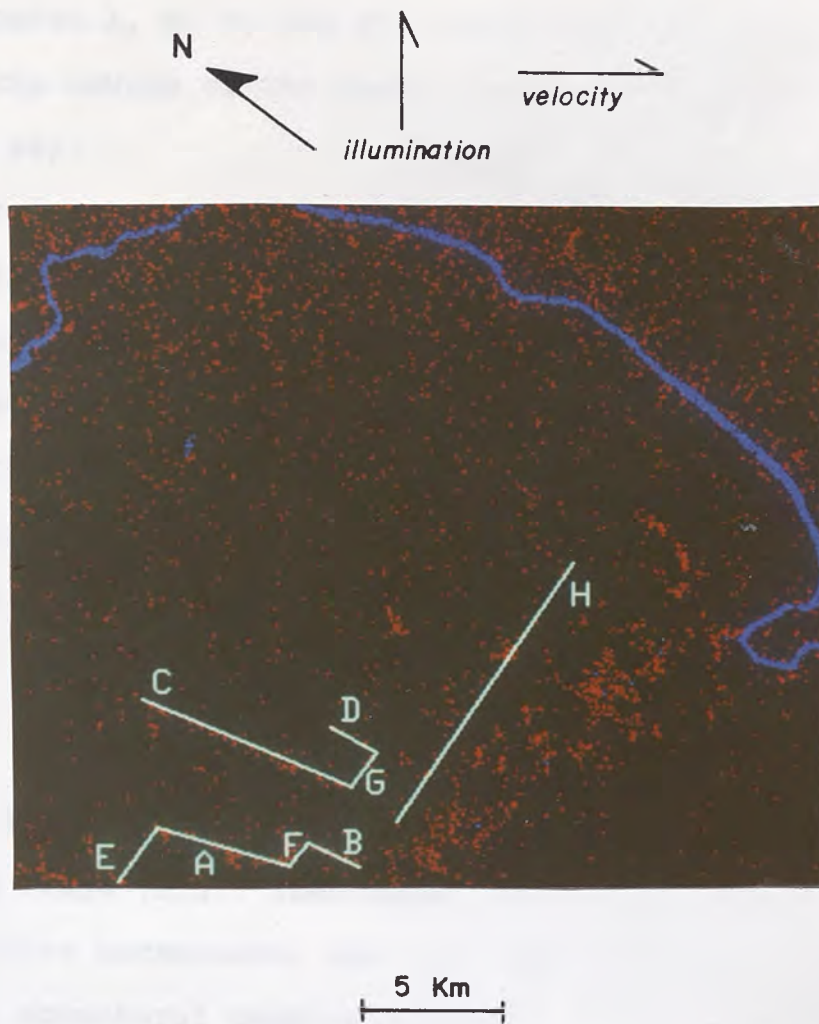


Figure 28. Linear geomorphic features defined on the basis of the spatial distribution of flooded vegetation.

- (1) features A, B, C, and D: rectilinear streams parallel to the course of the Içana River (compare Figures 27 and 28);
- (2) features E, F, and G: linear drainage segments oriented in the same direction of the Piraiauara River (compare Figures 27 and 28). They offset the rectilinear streams parallel to the Içana River;
- (3) feature H: subtle topographic high subparallel to the course of the Piraiauara River (compare Figures 27 and 28).

#### IDENTIFICATION OF TONAL LINEAR FEATURES USING A CONTRAST STRETCHING TECHNIQUE

The identification of spatial radiometric patterns on the SIR-B image (e.g., individual linear features developed on an uniform background) was considered important in this study for structural mapping purposes. This task was difficult because (a) geologic structures and boundaries between different lithologic units have little apparent expression in the study area; (b) the DN range of the Guiana Shield SIR-B data is rather restricted due to problems in data acquisition. A digital image-processing procedure had to be used before photogeologic interpretation was possible.

The analysis of SIR-B data was conducted on a VAX 11/780 based Interactive Digital Image Manipulation System (IDIMS) at the Mackay School of Mines. A simple linear



contrast stretch program called TLM (trackball linear mapping) was applied to expand the originally narrow range of SIR-B DN values. This IDIMS function allows the user to interactively apply a linear intensity transformation to the currently displayed image. The trackball and the cursor are utilized to control the slope (contrast) and intercept (brightness) of the linear transformation. The user can adjust the contrast of the image by moving the cursor vertically up and down. Image brightness can be regulated by moving the cursor horizontally from left to right (VAX-IDIMS Functional Guide, 1987).

Differences between contrast-stretched images originated from the same raw data are sometimes subtle. Selection of the "best" enhancement is a subjective decision taken by the interpreter (Masuoka et al., 1988). The image shown in Figure 29 was considered to be the best result obtained with TLM in the study area. Spatial radiometric patterns identified on this TLM-stretched image can be described as (a) linear stream channels with bright radar signatures associated with flooded vegetation, and (b) dark linear features developed on an uniform background. Attempts to perform directional filtering in order to highlight tonal features with specific orientations were not as successful.

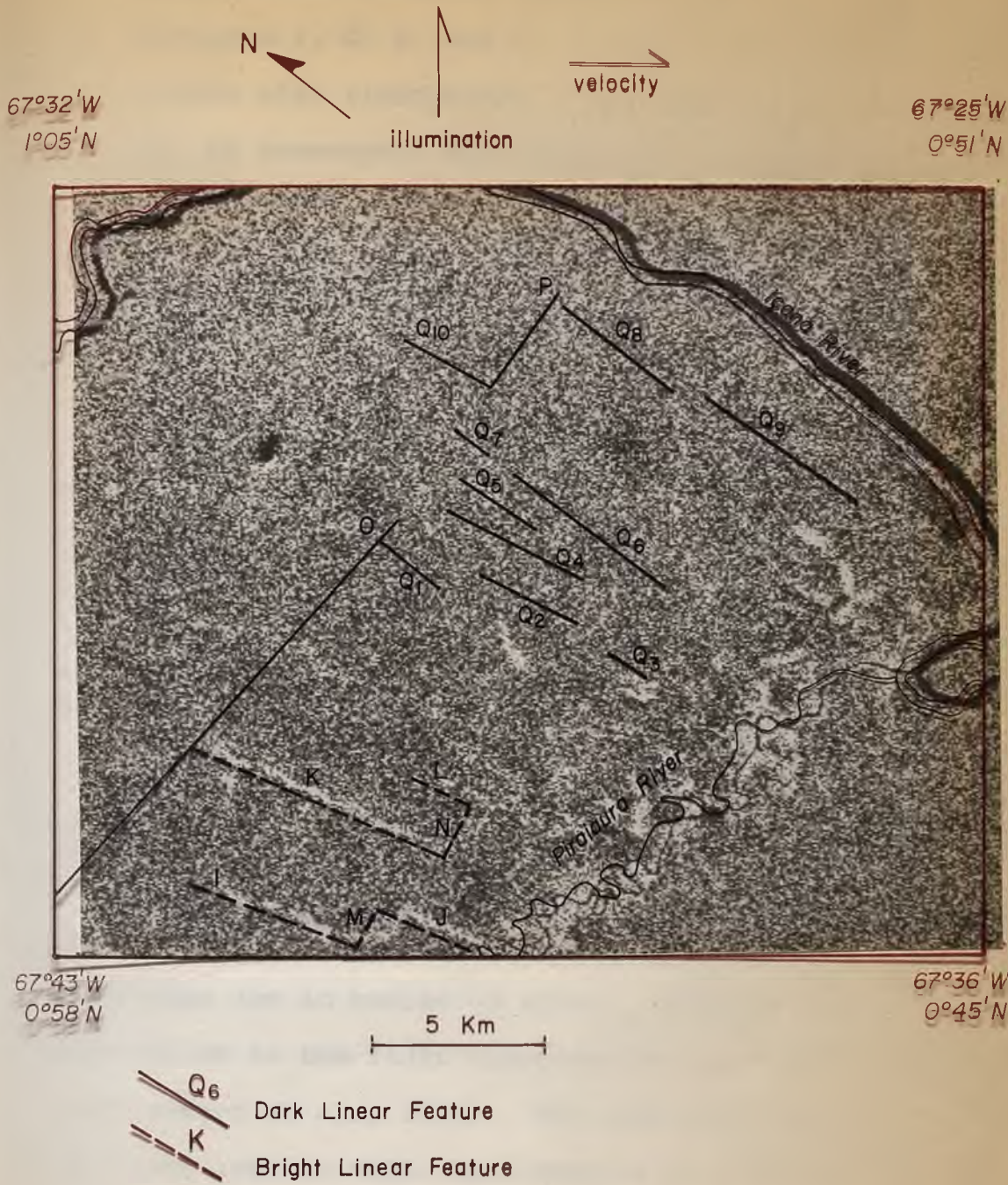


Figure 29. SIR-B contrast-stretched image using TLM (trackball linear mapping).

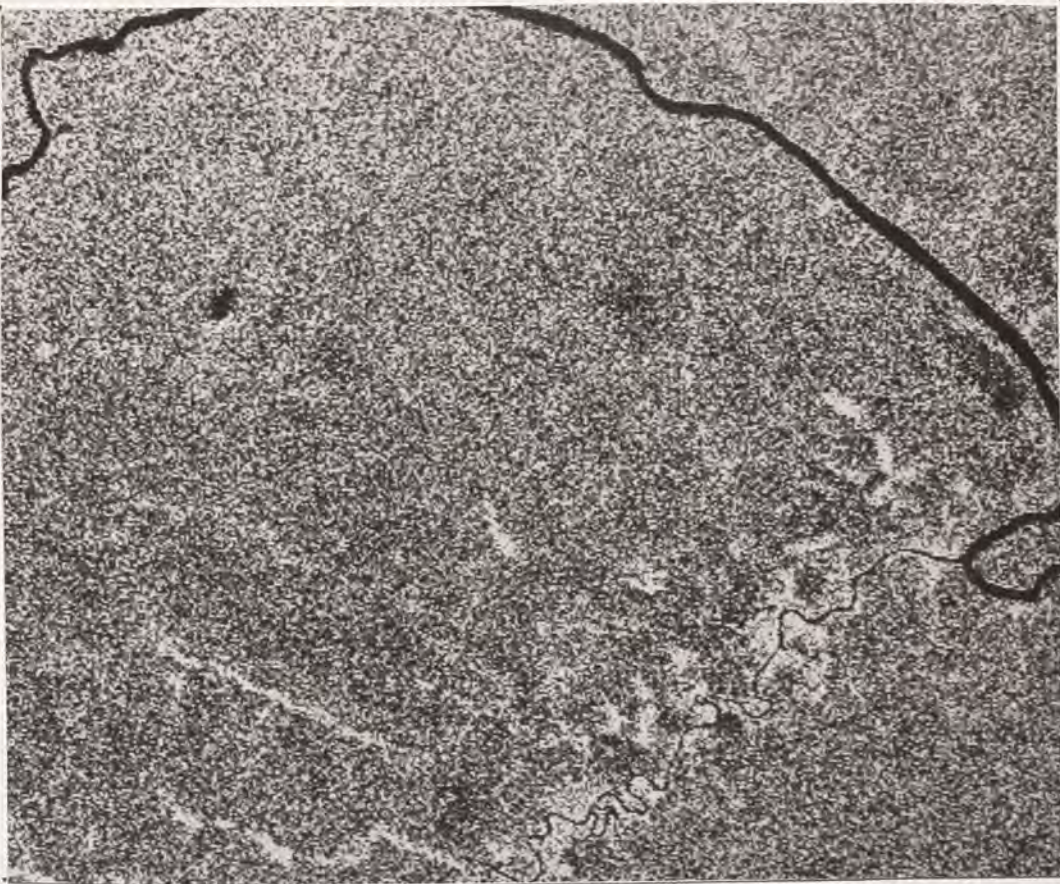


Figure 29. SIR-B contrast-stretched image using TLM (trackball linear mapping).

Tonal linear features identified on Figure 29 are:

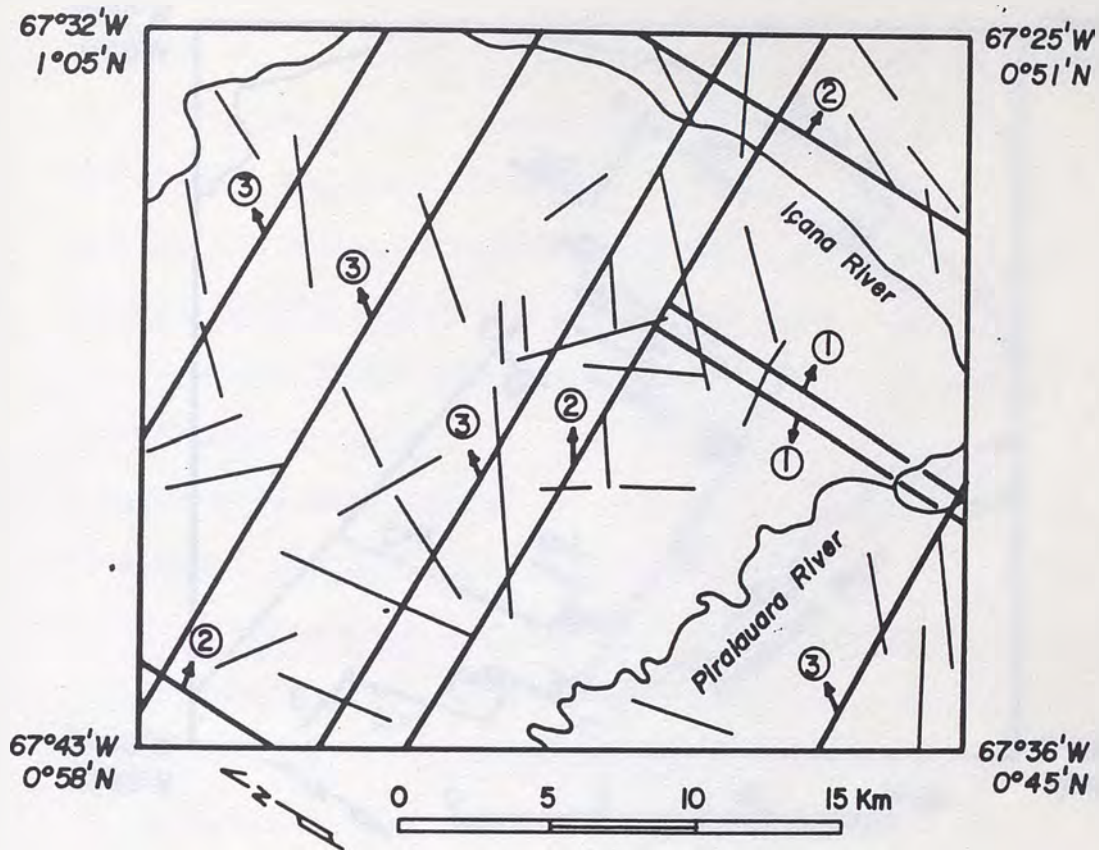
- (1) features I, J, K, and L: bright linear features associated with floodplains. They correspond, respectively, to geomorphic features A, B, C, and D on Figure 28;
- (2) features M and N: bright linear features offsetting the previous ones. They correspond, respectively, to geomorphic features F and G on Figure 28;
- (3) feature O: dark linear feature developed on a watershed zone (notice how it truncates feature K);
- (4) feature P: dark linear feature aligned with feature O;
- (5) features Q<sub>1</sub> to Q<sub>10</sub>: dark linear features parallel to the course of the Içana River. They define a trend on the image whose individual elements do not cross features O and P.

The photointerpreter has always to take into account the influence of radar look direction in the detection of structural trends. Unless there are compensating factors such as roughness (as along linear clearings) or dielectric properties (as in bodies of water), features within 20° of parallelism to the radar illumination are practically invisible (Lowman et al., 1987). The look direction of SIR-B in the study area is N57E, what results in detectability restrictions for features striking N37E to N77E. This fact was thoroughly considered when aeromagnetic and SIR-B data were jointly analyzed (Chapter 6).

An additional remark refers to the X-band SLAR imagery acquired by the RADAMBRASIL Project. According to Correa (1979), anomalous features can be found in the RADAMBRASIL SLAR images which are not related to any of the terrain types present in the surveyed region. Figure 20 illustrates some of these artifacts in the study area: (a) fine lines along the radar azimuth direction (N-S) which indicate that the data film was scratched during processing; (2) part of the mosaic showing two radar strips separated by a straight line; (3) strong banding along the range direction (E-W) observed when the radar system did not compensate for excessive aircraft flight instability. These problems made the identification of tonal linear features using RADAMBRASIL images a difficult task. Figure 30 shows that the SLAR mosaics corresponding to the investigated site are severely affected by artifacts. Therefore, such a data set was not utilized in this research.

#### DEVELOPMENT OF A MAP OF SIR-B LINEAR FEATURES

The map of SIR-B linear features shown in Figure 31 includes (a) spatial radiometric patterns identified on the linearly stretched SIR-B image, and (b) linear geomorphic features defined on the basis of the spatial distribution of flooded vegetation (compare Figures 28, 29, and 31). SIR-B linear features may represent the surface expression of



**Artifacts:**

- ① Fine lines along azimuth direction
- ② Radar strips separated by a straight line
- ③ Strong banding along range direction

Figure 30. Tonal linear features identified on X-band RADAMBRASIL SLAR images.

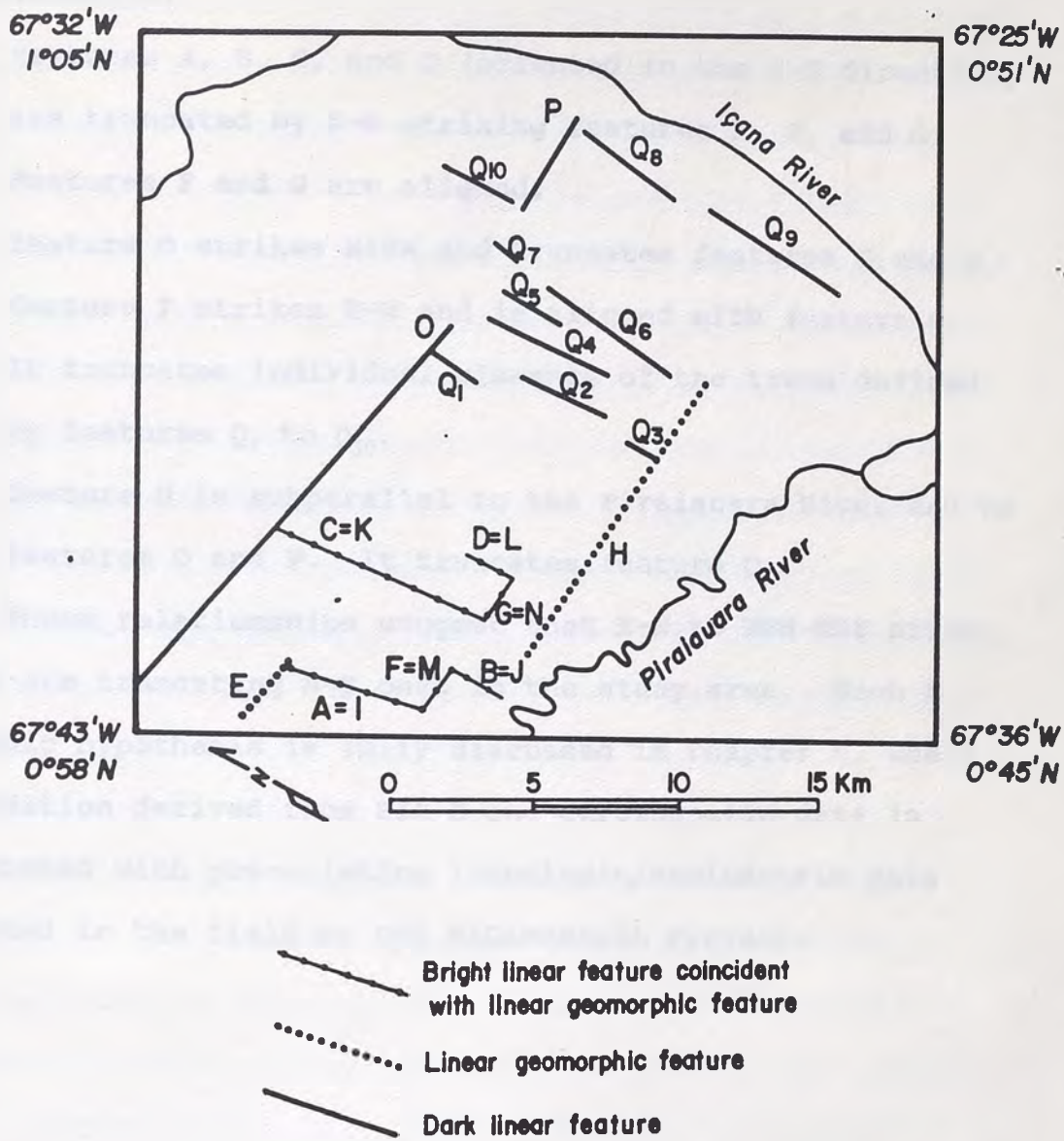


Figure 31. Map of SIR-B linear features.

underlying geologic structures. Examination of Figure 31 allows the establishment of the following cross-cutting relationships:

- (a) features A, B, C, and D (oriented in the N-S direction) are truncated by E-W striking features E, F, and G. Features F and G are aligned;
- (b) feature O strikes N80W and truncates features C and Q<sub>1</sub>;
- (c) feature P strikes E-W and is aligned with feature O. It truncates individual elements of the trend defined by features Q<sub>1</sub> to Q<sub>10</sub>.
- (d) feature H is subparallel to the Piraiuara River and to features O and P. It truncates feature Q<sub>3</sub>.

These relationships suggest that E-W to WNW-ESE structures are truncating N-S ones in the study area. Such a geologic hypothesis is fully discussed in Chapter 6, where information derived from SIR-B and aeromagnetic data is integrated with pre-existing lithologic/radiometric data obtained in the field by the RADAMBRASIL Project.



## CHAPTER V

## AEROMAGNETIC ANALYSIS

Regional investigations are often aided by the analysis of magnetic anomalies associated with major geologic features (see for example Hildenbrand et al., 1983). The distribution of upper-crustal magnetized rock bodies interpreted from the anomalies may convey new information about known lithotectonic units or reveal the existence of previously unreported ones. The availability of digital aeromagnetic data in the Guiana Shield allowed the development of a variety of products which are useful to geologic mapping (e.g., grey-scale aeromagnetic images, horizontal-gradient and terrace-magnetization maps). The analytical techniques used to generate such products are discussed in this chapter.

## CHARACTERISTICS OF THE DIGITAL AEROMAGNETIC DATA

The digital aeromagnetic data used in this research were obtained in February 1987 by ENCAL S/A Consultoria e Aerolevantamentos, under contract to the Brazilian government (Hildenbrand et al., 1987). This survey was part of a major aerogeophysical reconnaissance embracing approximately 157,000 square kilometers in northwestern Brazil (border region with Colombia and Venezuela). Measurements of the total magnetic field strength were carried out by a proton-

precession magnetometer GEOMETRICS, model G-803, with sensitivity of 1.0 nanotesla (nT). Flight-lines were flown north-south, with a line spacing of 2.0 km and a sampling interval of approximately 60 m. Tie-lines were flown east-west, with 20.0 km line spacing. The survey was performed in a draped mode 150 m of constant elevation above the relatively flat terrain of the investigated region.

The reduction of total magnetic field data to anomaly data is necessary to remove estimated causes of magnetic variation from the original observations other than those arising from the magnetic effects of the Earth's crust (Kearey and Brooks, 1984). In the Guiana Shield, corrections were performed by Hildenbrand et al. (1987) with regard to (a) significant time variations of magnetic measurements with periods of seconds, minutes, and hours due to solar-induced activity (diurnal variation correction); (b) differences between magnetic field values at intersections between flight lines and tie lines (leveling of magnetic profiles); (c) effects of theoretical magnetic dipoles at the center of the Earth (IGRF removal).

The IGRF (International Geomagnetic Reference Field) is a mathematical representation of the Earth's main magnetic field due to sources in the core (Dobrin and Savit, 1988). About 90% of the Earth's field can be represented by the field of a theoretical magnetic dipole at the center of the

Earth inclined at about  $11.5^\circ$  to the axis of rotation (Kearey and Brooks, 1984). The magnetic moment of this theoretical geocentric dipole can be calculated from the observed field. If this dipole field is subtracted from the observed magnetic field, the residual field can then be approximated by the effects of a second, smaller dipole. The process can be continued by fitting dipoles of ever decreasing moment until the observed geomagnetic field is simulated to any required degree of accuracy. The effects of each fictitious dipole contribute to a function known as an harmonic and the technique of successive approximations of the observed field is known as spherical harmonic analysis (Kearey and Brooks, 1984). This method has been used to compute the formula of the International Geomagnetic Reference Field (IGRF) which defines the theoretical undisturbed magnetic field at any point on the Earth's surface. In magnetic surveying, the IGRF is used to remove from the data those magnetic variations attributable to this theoretical field.

The IGRF removal from the Guiana Shield data was performed by Hildenbrand et al. (1987) as follows:

- (1) a geomagnetic reference field (IGRF) was calculated for 13 points uniformly distributed in the survey area. Calculations were carried out utilizing the method

proposed by the United States Department of Commerce-  
Environmental Science and Services Administration  
(USDC-ESSA), 1985, updated to February 1987;

- (2) a least-square regression was performed to obtain the coefficients for the two-variable, second-order polynomial surface that best fits these 13 points where the IGRF was calculated;
- (3) an approximate geomagnetic reference field was then calculated for each sample in the survey area using the coefficients obtained from step (2). This reference field was obtained utilizing the following equation:

approximate geomagnetic reference field (nT) =

$$= Ax^2 + By^2 + Cxy + Dx + Ey + F, \text{ where}$$

$$x = e - 724 \text{ km}$$

$$e = \text{sample UTM coordinate (east) in km}$$

$$y = n - 10066 \text{ km}$$

$$n = \text{sample UTM coordinate (north) in km}$$

$$A = -0.14558 \times 10^{-3} \text{ nT/Km}^2$$

$$B = 0.53744 \times 10^{-3} \text{ nT/Km}^2$$

$$C = -0.22348 \times 10^{-3} \text{ nT/Km}^2$$

$$D = -1.06317 \text{ nT/Km}$$

$$E = 4.27442 \text{ nT/Km}$$

$$F = 30716.6 \text{ nT}$$

- (4) the calculated reference field value for each sample was then subtracted from the sample's measured value.

Having applied the diurnal, leveling, and geomagnetic corrections, the remaining magnetic field variations in the study area, hereafter referred to as magnetic anomalies, are theoretically attributed to spatial changes in the magnetic properties of the Earth's crust down to the Curie-point isotherm. The Curie point is the temperature at which magnetic properties of ferromagnetic and ferrimagnetic substances disappear (575° C for magnetite; Telford et al., 1986). The Curie-point isotherm for common ferrimagnetic minerals such as magnetite lies at a depth of about 20 Km in continental areas (Kearey and Brooks, 1984), but it varies with changes in geothermal gradient and water content of lower crustal materials. The sources of major magnetic anomalies are consequently restricted to the upper part of the continental crust.

Following data reduction, the aeromagnetic data set consists of a series of profile lines composed of values of magnetic anomalies. In order to obtain grey-scale images or terrace-magnetization maps, it is necessary to convert these unevenly distributed profile values to a regularly spaced grid through a process of interpolation. The Guiana Shield data were gridded at an interval of 500 m (one-fourth the flight-line interval) by a minimum curvature technique (computer program MINC; Webring, 1981). The output is a grid of equi-spaced interpolated values written to disk in

binary form. This program uses the biharmonic difference equation to generate a smooth surface that has the property of minimum total curvature, where curvature refers to the estimate of the second horizontal derivatives in x and y directions at each grid location (Webring, 1981). The critical parameter concerning MINC is gridding interval. A coarse interval results in aliasing (distortion of output frequency) and loss of information. Too fine an interval results in isolated anomalies and an obscured regional picture. Webring (1981) suggests that the optimum interpolation interval is generally one-half to one-fifth the data spacing (recall that the Guiana Shield data was gridded at one-fourth the flight-line interval). In this study, the size of the grid obtained with MINC was 222 rows x 223 columns. A contour map generated from this regular grid is shown in Figure 32. Only the 100 nT contour lines have been represented in order to avoid clutter. This product corresponds to a  $1^\circ \times 1^\circ$  area encompassing the study site (see location map in Figure 33). The gridded data obtained with the minimum - curvature interpolation technique provided the database for the analytical procedures subsequently discussed in this chapter.

Figure 32. Magnetic anomaly map of the study site. Contour interval is 100 nT. Contour lines are drawn at 100 nT intervals.

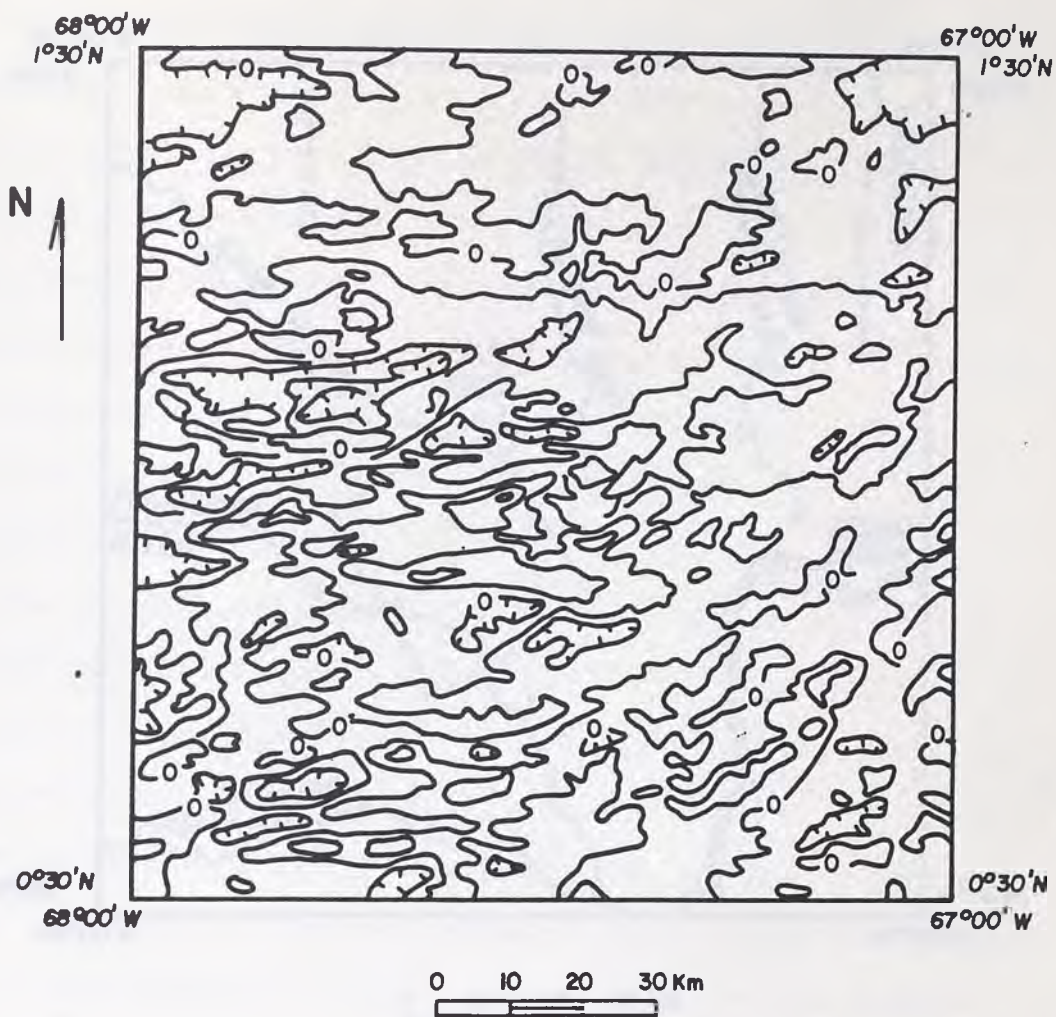


Figure 32. Magnetic anomaly map (Guiana Shield). Contour interval is 100 nT. Hachures indicate areas of magnetic lows.

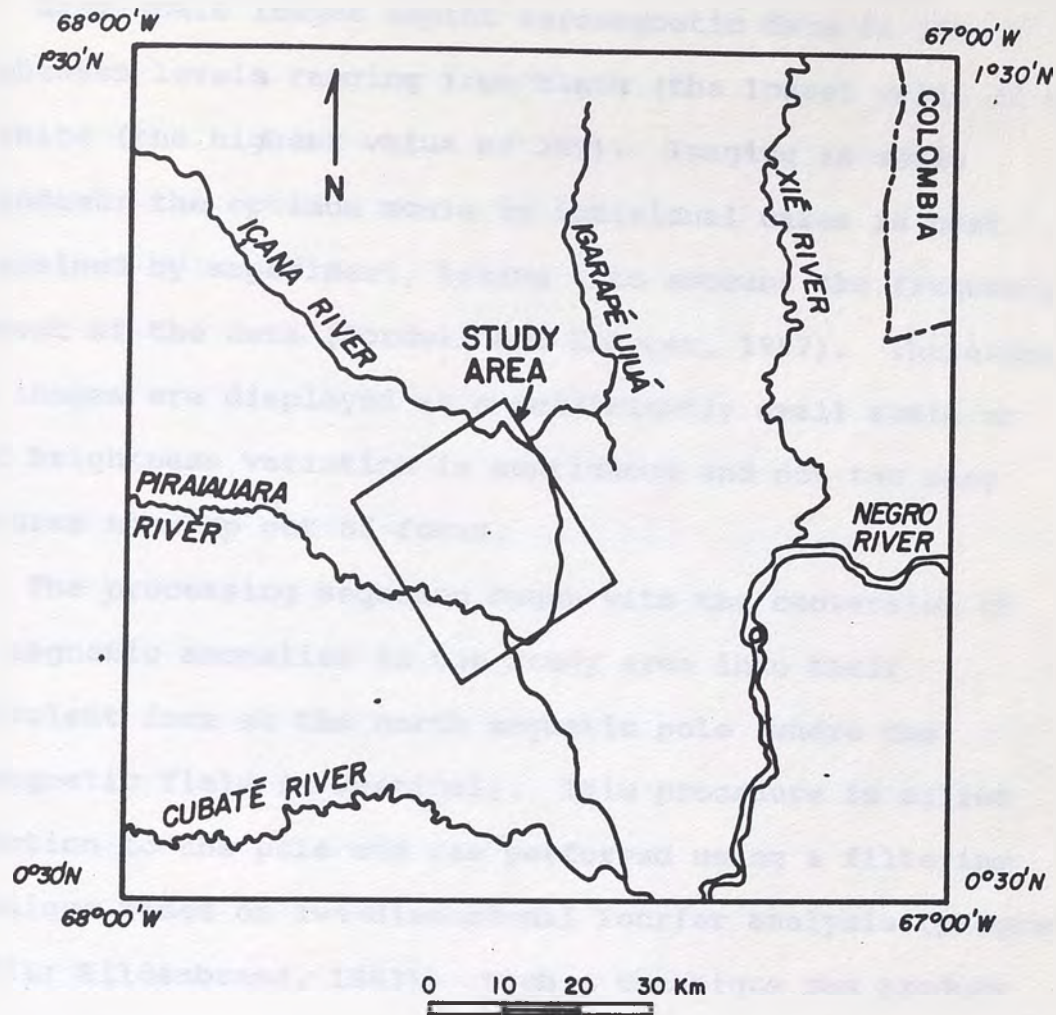


Figure 33. Location map of the aeromagnetic data set.



## PRODUCTION OF A GREY-SCALE AEROMAGNETIC IMAGE

Grey-scale images depict aeromagnetic data in 256 brightness levels ranging from black (the lowest value of 0) to white (the highest value of 255). Imaging is scale dependent; the optimum scale in individual cases is best determined by experiment, taking into account the frequency content of the data (Cordell and Knepper, 1987). Therefore, the images are displayed at a sufficiently small scale so that brightness variation is continuous and not too many features show up out of focus.

The processing sequence began with the conversion of the magnetic anomalies in the study area into their equivalent form at the north magnetic pole (where the geomagnetic field is vertical). This procedure is called reduction to the pole and was performed using a filtering technique based on two-dimensional Fourier analysis (program FFTFIL; Hildenbrand, 1983). Such a technique can produce distorted anomalies near grid boundaries. These anomalies result from abrupt terminations of the data. This edge effect can be appreciably reduced by adding rows and columns of assigned grid values to the input data. Edge effects are still present but are primarily within the frame of assigned border values which are removed after the filtering process (Hildenbrand, 1983). In the Guiana Shield, 20 rows and columns were added to each side of the input grid in order

to reduce edge distortions. The program FFTFIL required as input parameters the inclination ( $25.1^\circ$ ) and declination ( $-6.8^\circ$ ) of the geomagnetic field in the investigated region by the time the survey was performed (February 1987). Lacking constraints, it was assumed that the magnetization vector was parallel to the geomagnetic field (i.e., no remanent magnetization was present).

A symmetric body produces a symmetric anomaly at the magnetic poles (Dobrin and Savit, 1988). Hence, the reduction to the pole is a way to remove asymmetries caused by a nonvertical magnetization (an effect which is particularly severe at low magnetic latitude areas such as the Guiana Shield). Symmetric anomalies are visually easy to interpret because they are approximately centered over their respective causative bodies.

After reducing the magnetic anomalies to the pole, a grey-scale aeromagnetic image was obtained as follows:

- (1) the data were regridded to a very fine grid interval (60m) using cubic-spline interpolation (program REGRID; Branch of Geophysics, 1989). The size of the grid was 1842 rows x 1851 columns, which determined the dimensions of the grey-scale image negative (1 grid interval = 60m = 1 pixel = 0.01 cm on the negative; therefore 1842 rows x 1851 columns gave rise to a 18.4 cm x 18.5 cm film negative at a scale of 1:600,000);

- (2) in order to convert the grid to an image, magnetic anomaly values were rescaled to integers in the range 0 to 255 using the program GRDREM (L. Cordell, U.S. Geological Survey, written communication). The software truncated the upper and lower two percent of the magnetic anomaly values and linearly scaled the remaining data to 256 brightness levels ranging from black (lowest value) to white (highest value). The objective was to produce an image with good overall contrast. Dynamic range was reduced, and therefore short-wavelength (high-frequency) features were enhanced;
- (3) the file obtained from step (2) was written to a magnetic tape for standard optronics processing, which resulted in a negative film-transparency of the grey-scaled aeromagnetic image at a scale of 1:600,000.

Examination of the Guiana Shield aeromagnetic data using the grey-scale image format (Plate 1) enabled the identification of distinct magnetic patterns in the surroundings of the study area:

- (1) pattern a: magnetically low areas characterized by very dark signatures on the grey-scale image and probably related to two-mica granite plutons (similar interpretation was made by Cordell and Knepper, 1987);

- (2) pattern b: areas characterized by intermediate brightness levels and probably related to gneisses;
- (3) pattern c: magnetically high areas characterized by very bright signatures on the grey-scale image and probably related to magnetic granites (as suggested by Anne E. McCafferty, U.S. Geological Survey, personal communication);
- (4) pattern d: dike-like magnetic feature cross-cutting pattern c and probably related to a discordant intrusive body. Grey levels are darker westward (point 1) than eastward (point 2). Consequently, magnetic anomaly values are lower westward than eastward;

The bright and dark spots visible on the grey-scale image (e.g., locations labelled with letter e on Plate 1) are survey artifacts. This effect is not apparent in the contour map depicted on Figure 32. The reason for such a problem is not exactly known. It may have been caused by vibration of the magnetometer during data acquisition (M. Webring, U.S. Geological Survey, personal communication). Rectilinear segments on the image are flight-line (N-S trends) or tie-line (E-W trends) artifacts (e.g., letters f and g, respectively, on Plate 1).

The patterns identified on the grey-scale aeromagnetic image are a qualitative representation of spatial variations in the magnetic properties of the upper levels of the crust.

However, such a representation is rooted in visual perception rather than in deterministic physical theory (as pointed out by Cordell and Knepper, 1987). A quantitative approach to resolve how magnetization domains are distributed in the study area is given by the terracing operator (Cordell and McCafferty, 1989). This technique is discussed in the next section.

#### DEVELOPMENT OF A TERRACE-MAGNETIZATION MAP OF THE GUIANA SHIELD AEROMAGNETIC DATA

The terrace procedure yields a highly useful geologic-like map, where magnetic domains in the crystalline basement can be outlined. The physical property under consideration is magnetization ( $J$ ). A magnetic body placed in an external magnetic field becomes magnetized by induction. The intensity of induced magnetization ( $J_i$ ) is proportional to the strength of the field ( $H$ ) and is oriented in the direction of that field (Kearey and Brooks, 1984). The degree to which the body is magnetized is determined by its magnetic susceptibility ( $K$ ), which is defined as  $K=J_i/H$ . Therefore,  $J_i=KH$ . In the cgs system  $J_i$  is expressed in  $\text{emu}\cdot\text{cm}^{-3}$  ( $\text{emu}=\text{electromagnetic unit}$ ),  $H$  is measured in oersteds, and magnetic susceptibility is dimensionless. The inherited magnetization remaining after the removal of the external field is known as remanent magnetization ( $J_r$ ). Total magnetization ( $J$ ) is the sum of induced magnetization ( $J_i$ ) and remanent magnetization ( $J_r$ ). Due to the lack of

information concerning remanent magnetism in rocks of the study area, it is assumed that the total magnetization vector is parallel to the Earth's magnetic field (inclination =  $25.1^\circ$  and declination =  $-6.8^\circ$ ). This assumption is a possible source of error in the results obtained by the terracing operator.

A number of procedures were performed to produce the terrace-magnetization map of the Guiana Shield data. They are briefly described below. For a more detailed description, see Phillips (1990).

- (1) the initial step involved the removal of a second-order polynomial regional surface (Figure 34) from the gridded magnetic anomaly data (Figure 32) using the program SURFIT (Branch of Geophysics, 1989). The objective was to decrease the dynamic range of the data in order to emphasize short-wavelength anomalies associated with shallow crustal sources, and thereby improve the color resolution of these magnetic features (Cordell and McCafferty, 1989, and McCafferty, 1991). The resulting second-order residual magnetic field is portrayed as a color shaded relief map illuminated from north (Figure 35);
- (2) a close examination of Figure 35 revealed the presence of noise in the data, which is characterized by scattered spots on the map. A stripping filter

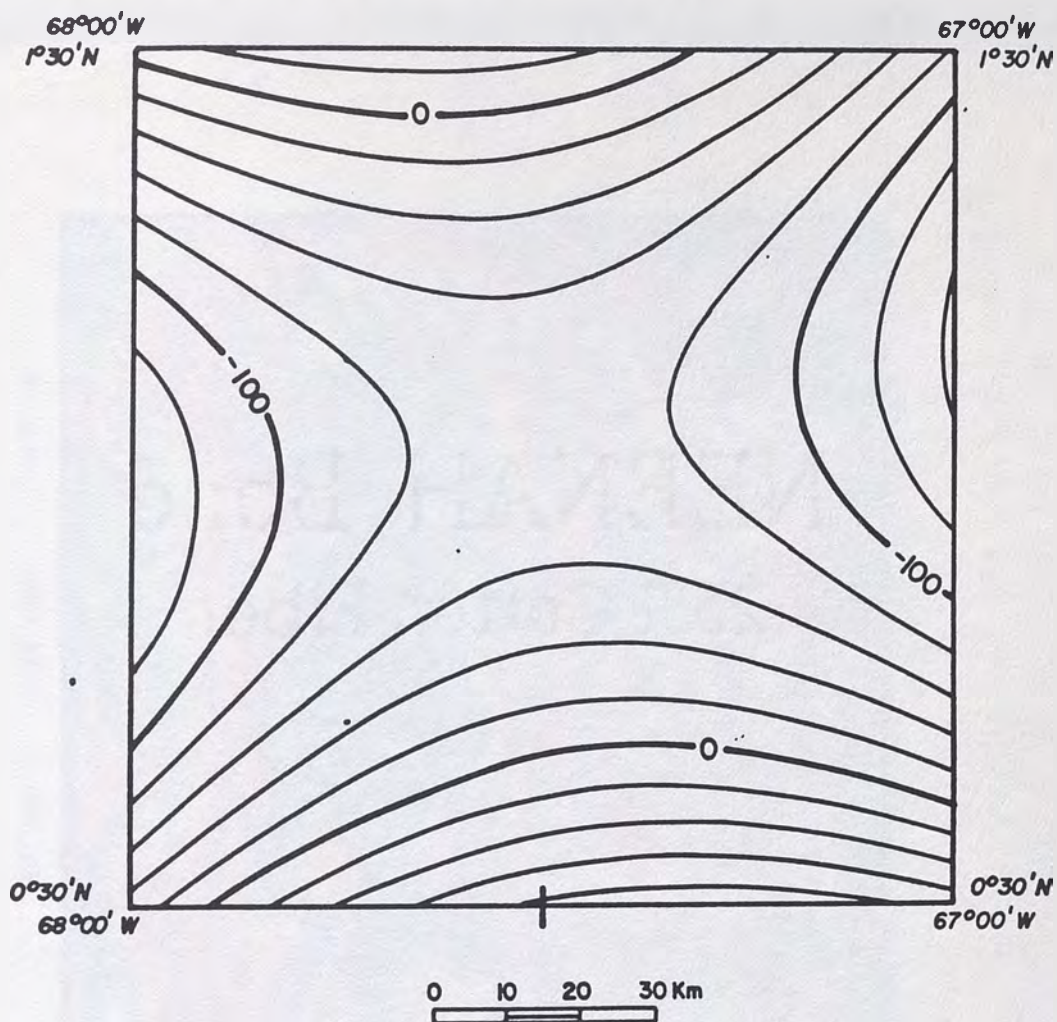


Figure 34. Second-order polynomial regional surface removed from the gridded magnetic anomaly data. Contour interval is 100 nT.

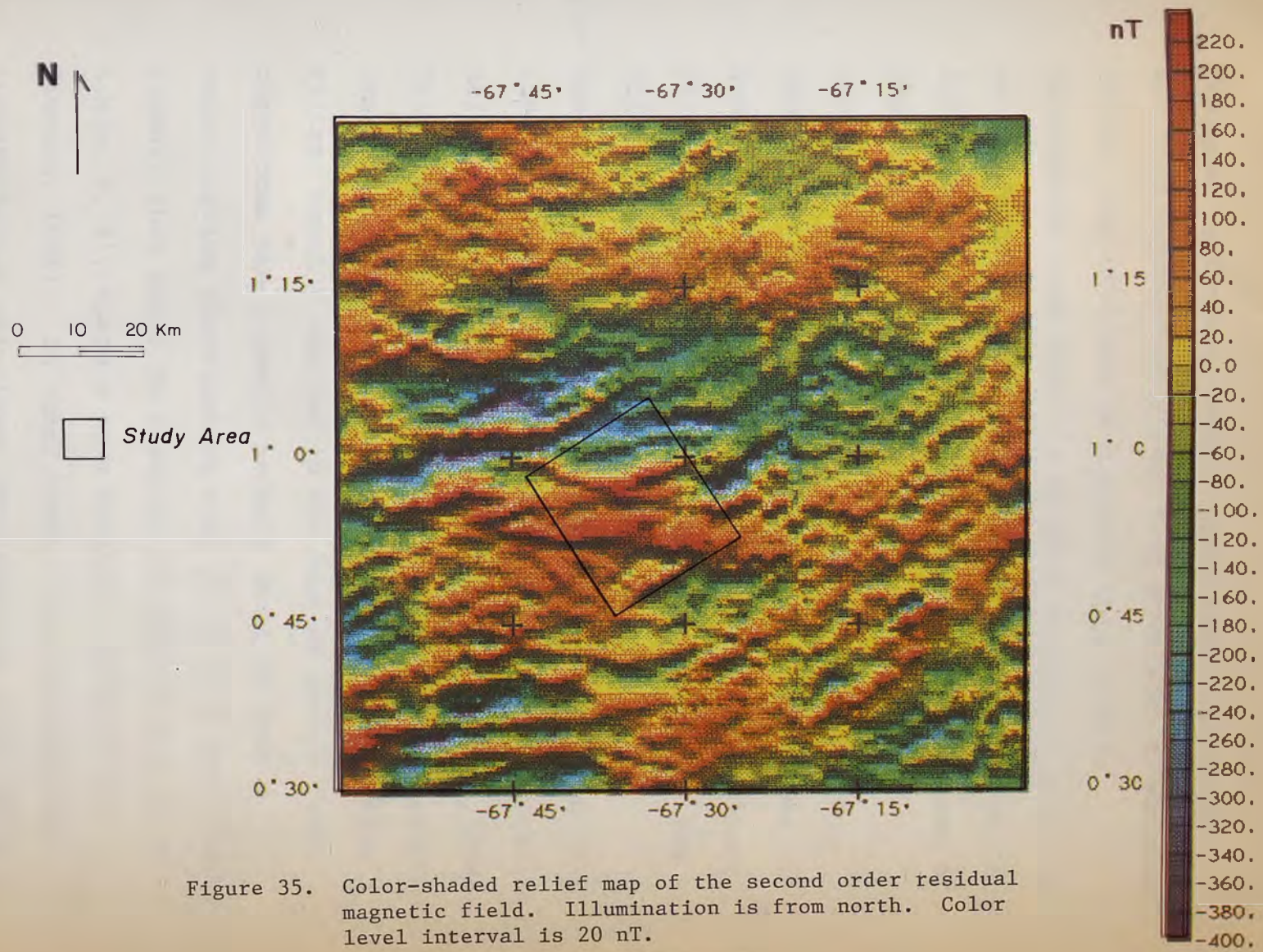


Figure 35. Color-shaded relief map of the second order residual magnetic field. Illumination is from north. Color level interval is 20 nT.



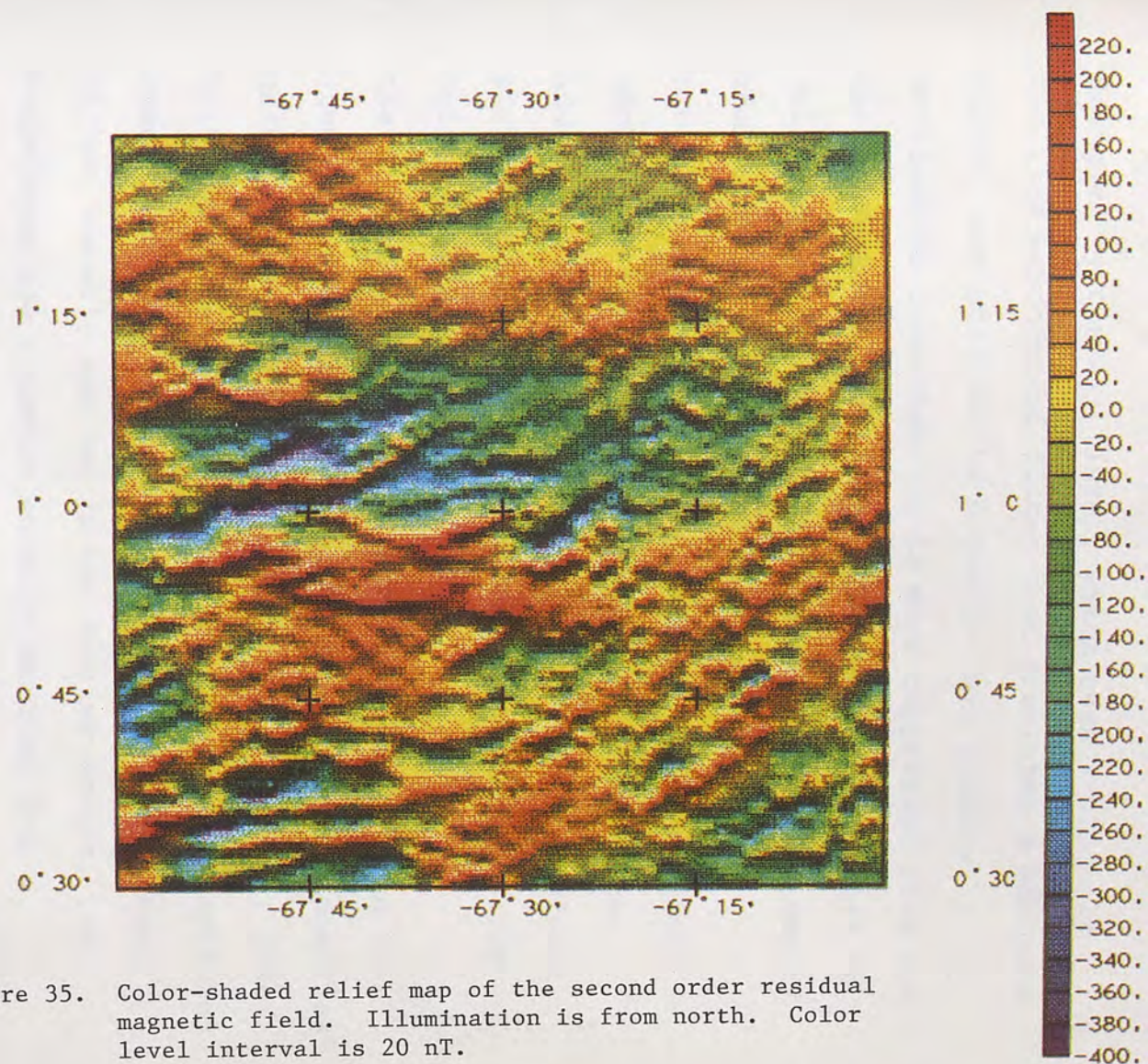


Figure 35. Color-shaded relief map of the second order residual magnetic field. Illumination is from north. Color level interval is 20 nT.

designed by Cordell (1985), which uses a slightly modified exponential filter that simulates a bandpass filter, was utilized to minimize this problem.

Wavelengths less than 3.0 km were suppressed from the data. Features indicative of noise were observed to fall within this range. A color shaded relief map of the filtered data is shown in Figure 36. This procedure may have resulted in loss of information about very shallow magnetic sources. Such a loss, however, did not have much influence on the regional picture obtained with the aeromagnetic data for the Guiana Shield study site;

- (3) the filtered second-order residual data obtained in step (2) were then converted to pseudogravity anomalies using the program BOUNDARY (Blakely and Simpson, 1986). This transformation is a standard step in the terracing operation. The pseudogravity transform is a linear filter, usually applied in the Fourier domain, that transforms the magnetic anomaly observed over a magnetization distribution  $m(x, y, z)$  into the gravity anomaly that would be observed if density  $\rho(x, y, z) = k \cdot m(x, y, z)$ , where  $k$  is a constant (Blakely and Simpson, 1986). In other words, the pseudogravity transformation calculates from magnetic data, given a density contrast and a magnetic contrast, the

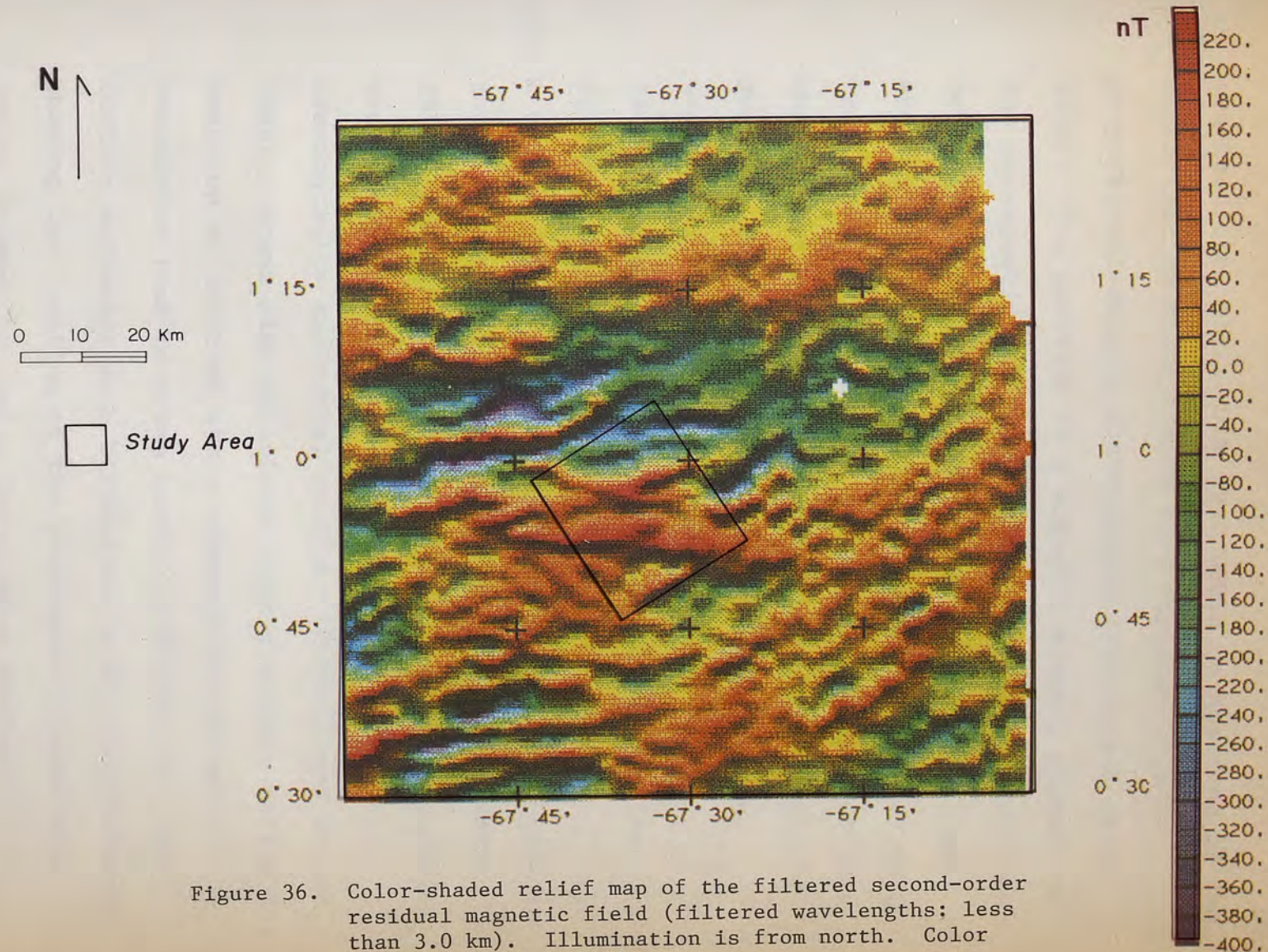


Figure 36. Color-shaded relief map of the filtered second-order residual magnetic field (filtered wavelengths: less than 3.0 km). Illumination is from north. Color level interval is 20 nT.

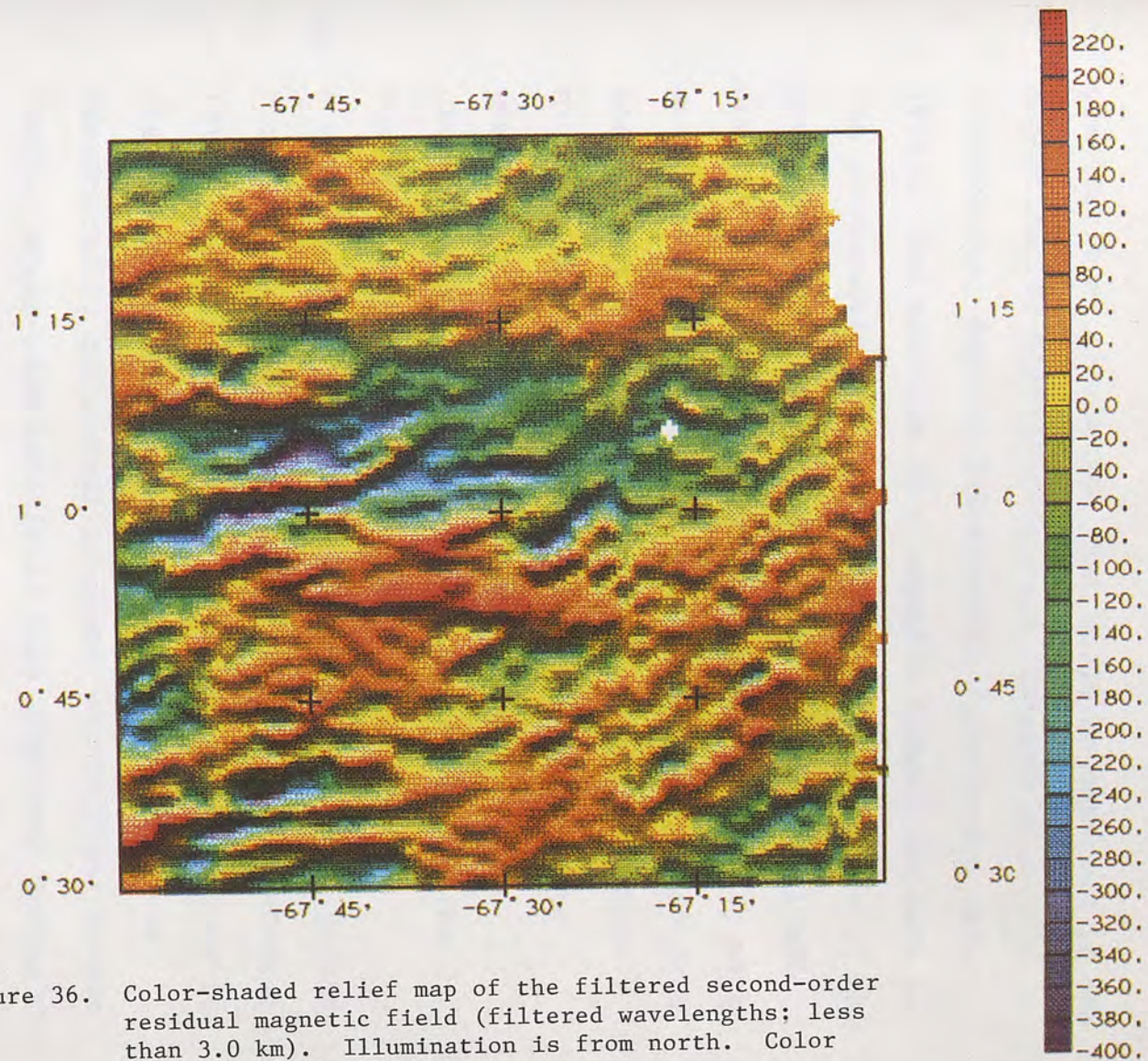


Figure 36. Color-shaded relief map of the filtered second-order residual magnetic field (filtered wavelengths; less than 3.0 km). Illumination is from north. Color level interval is 20 nT.

gravitational attraction that would be observed if the magnetization distribution were replaced by a proportional density distribution (Dobrin and Savit, 1988). The position of a magnetic anomaly depends on the geomagnetic latitude and the dipolar nature of the causative body. In regions of low magnetic latitude such as the Guiana Shield, the apparent location of a magnetization boundary is considerably displaced from the correct position. The amount of shift of the magnetic gradients relative to geologic contacts depends on the depth, strike, and shape of the causative body. The pseudogravity transformation corrects for this shift;

- (4) A grid of the horizontal gradient of the pseudogravity anomalies was calculated using the program BOUNDARY (Blakely and Simpson, 1986). Magnetization boundaries are determined by evaluating the magnitude of the pseudogravity horizontal gradient (Cordell and Grauch, 1985). Areas with relatively high gradients define the position of inferred steep basement-magnetization boundaries (red to green colors in Figure 37). To further emphasize such boundaries, a map was produced showing the location of the pseudogravity gradient maxima (Figure 38) using the program BOUNDARY.

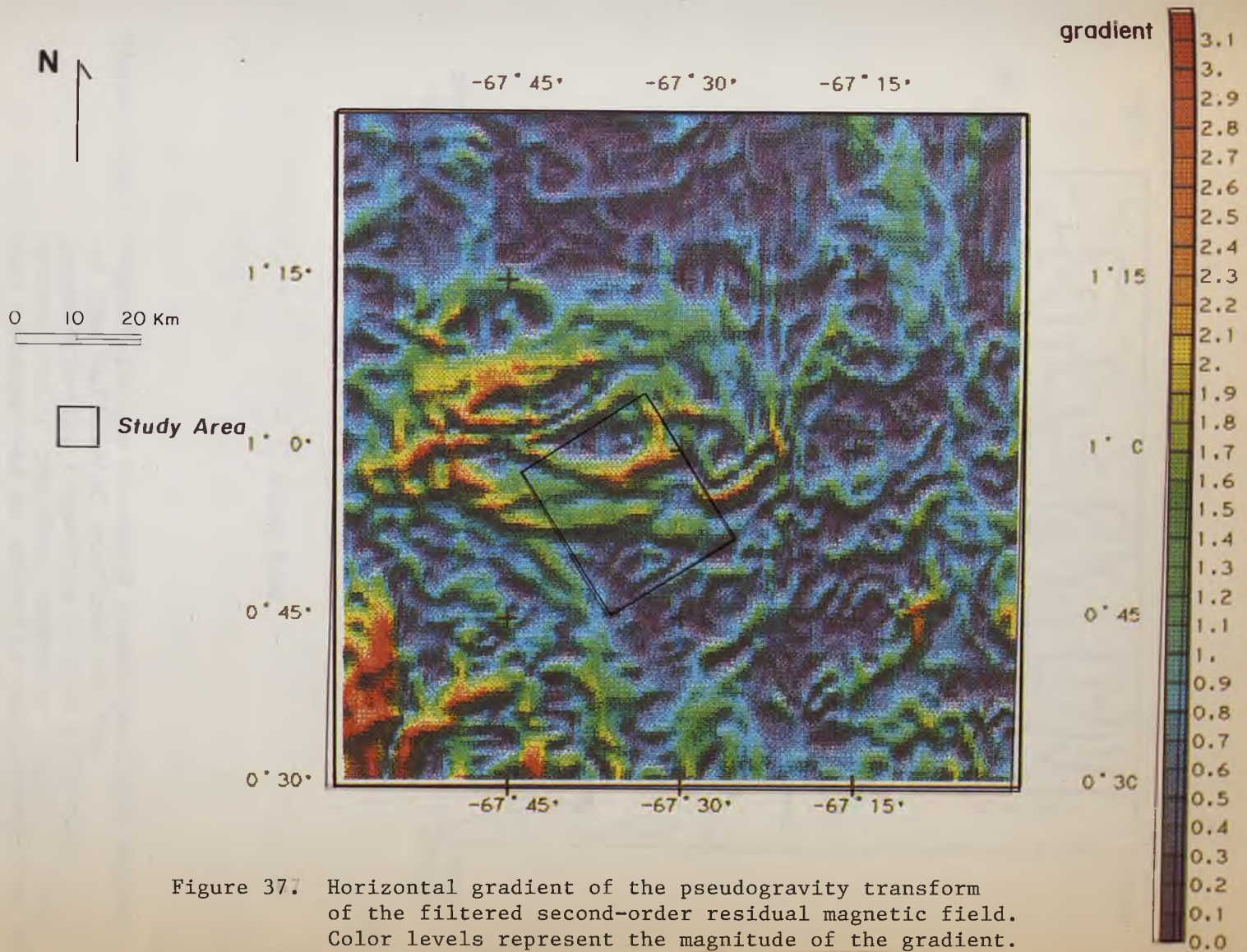


Figure 37. Horizontal gradient of the pseudogravity transform of the filtered second-order residual magnetic field. Color levels represent the magnitude of the gradient.

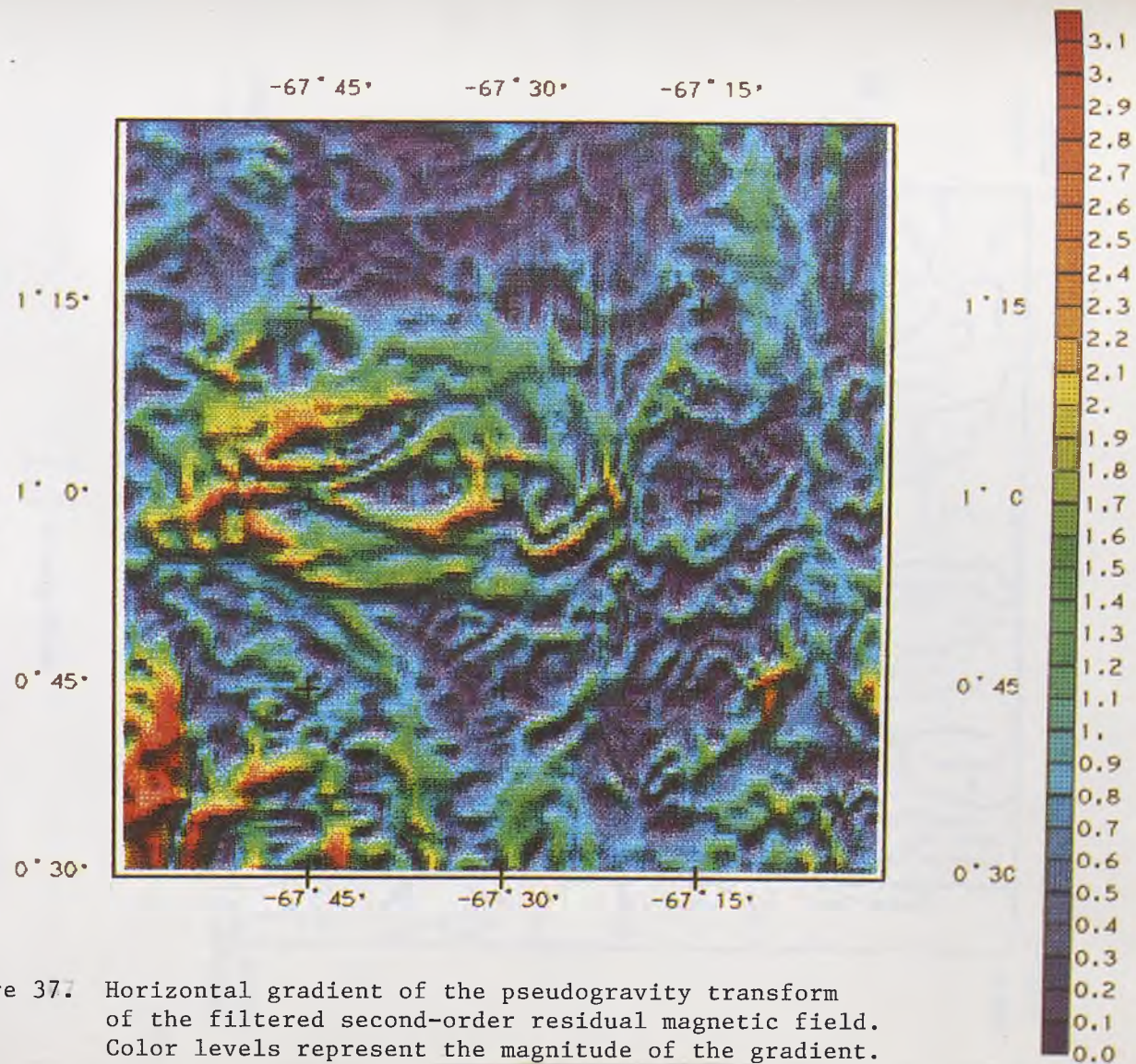


Figure 37. Horizontal gradient of the pseudogravity transform of the filtered second-order residual magnetic field. Color levels represent the magnitude of the gradient.

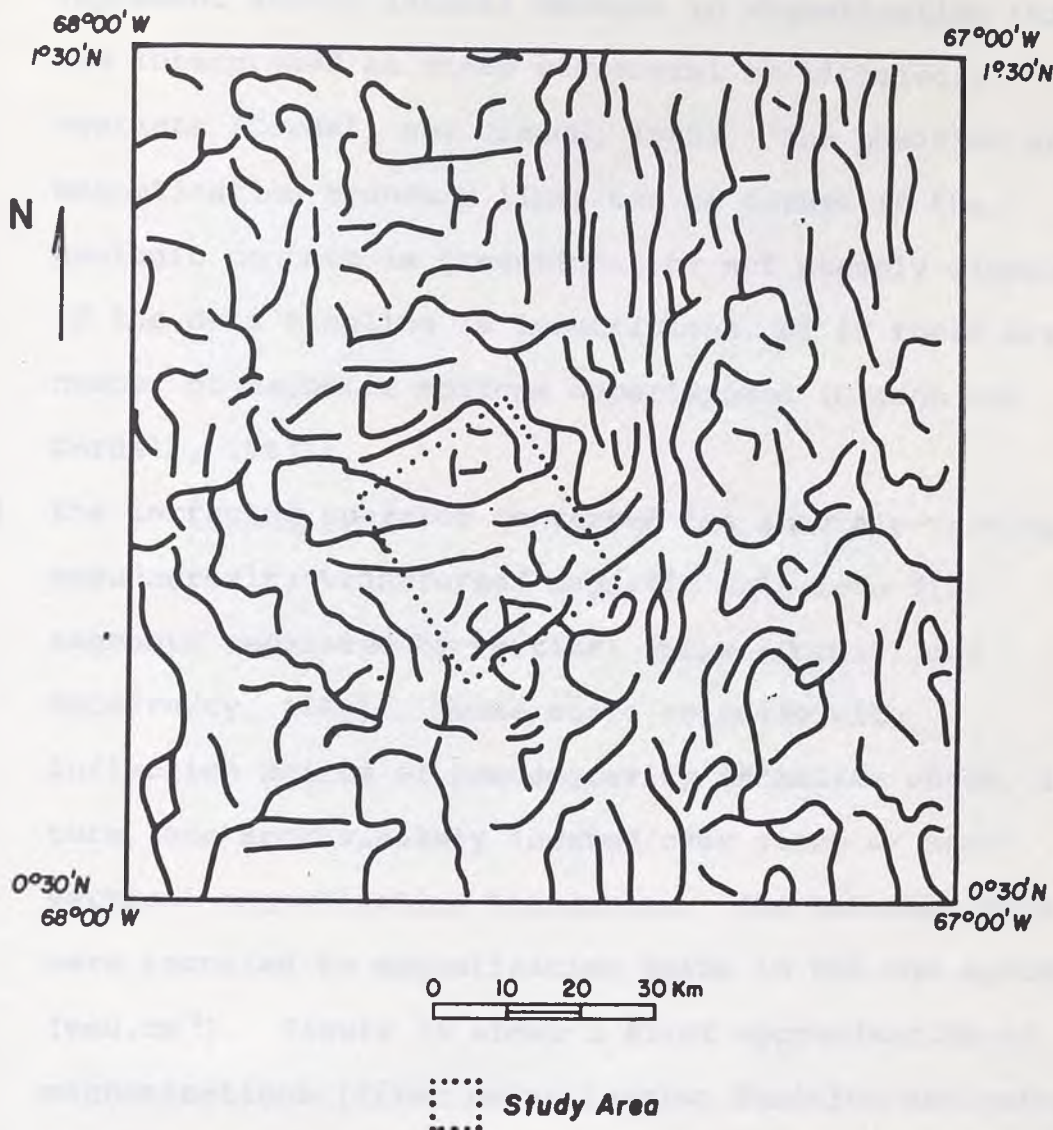


Figure 38. Magnetization boundary lines (maximum values of the horizontal gradient of the pseudogravity transform of the filtered second-order residual magnetic field). They are interpreted as magnetization boundaries at steep structural or lithologic contacts.



These maxima are designated as boundary lines and represent abrupt lateral changes in magnetization that are interpreted as steep structural or lithologic contacts (Cordell and Grauch, 1985). The position of magnetization boundary lines can be offset if the geologic contact is gradational or not steeply dipping, if the data sampling is insufficient, or if there are a number of magnetic sources superimposed (Grauch and Cordell, 1987);

- (5) the terracing operator converted the smoothly-varying, pseudogravity-transformed magnetic data into flat segments separated by vertical steps (Cordell and McCafferty, 1989). These steps coincide with inflection points of pseudogravity anomalies which, in turn, are approximately located over steep or near-vertical magnetization boundaries. The terraced data were rescaled to magnetization units in the cgs system ( $\text{emu.cm}^{-3}$ ). Figure 39 shows a first approximation of magnetizations (first magnetization function estimate).
- (6) the magnetic field of Figure 40 was calculated from the first magnetization function estimate (Figure 39) using the programs FFTFIL (Hildenbrand, 1983) and FFT\_MAG (L. Cordell, U.S. Geological Survey, unpublished program). The forward-calculation of the magnetic field was

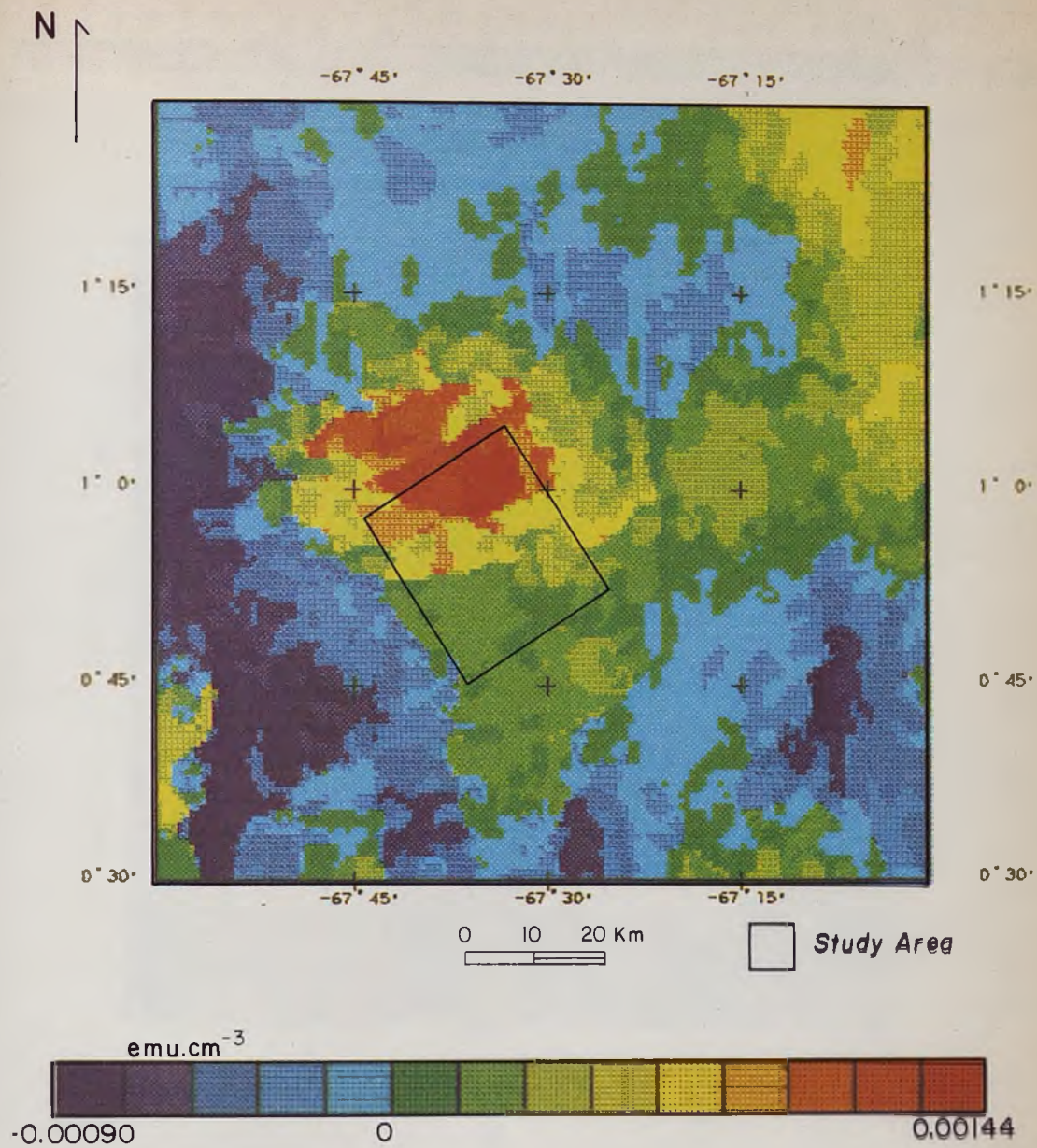


Figure 39. Terraced pseudogravity transform of the filtered second-order residual magnetic field rescaled to cgs units of magnetization ( $\text{emu.cm}^{-3}$ ). This is the first magnetization function estimate. Color level interval is  $0.00018 \text{ emu.cm}^{-3}$ .

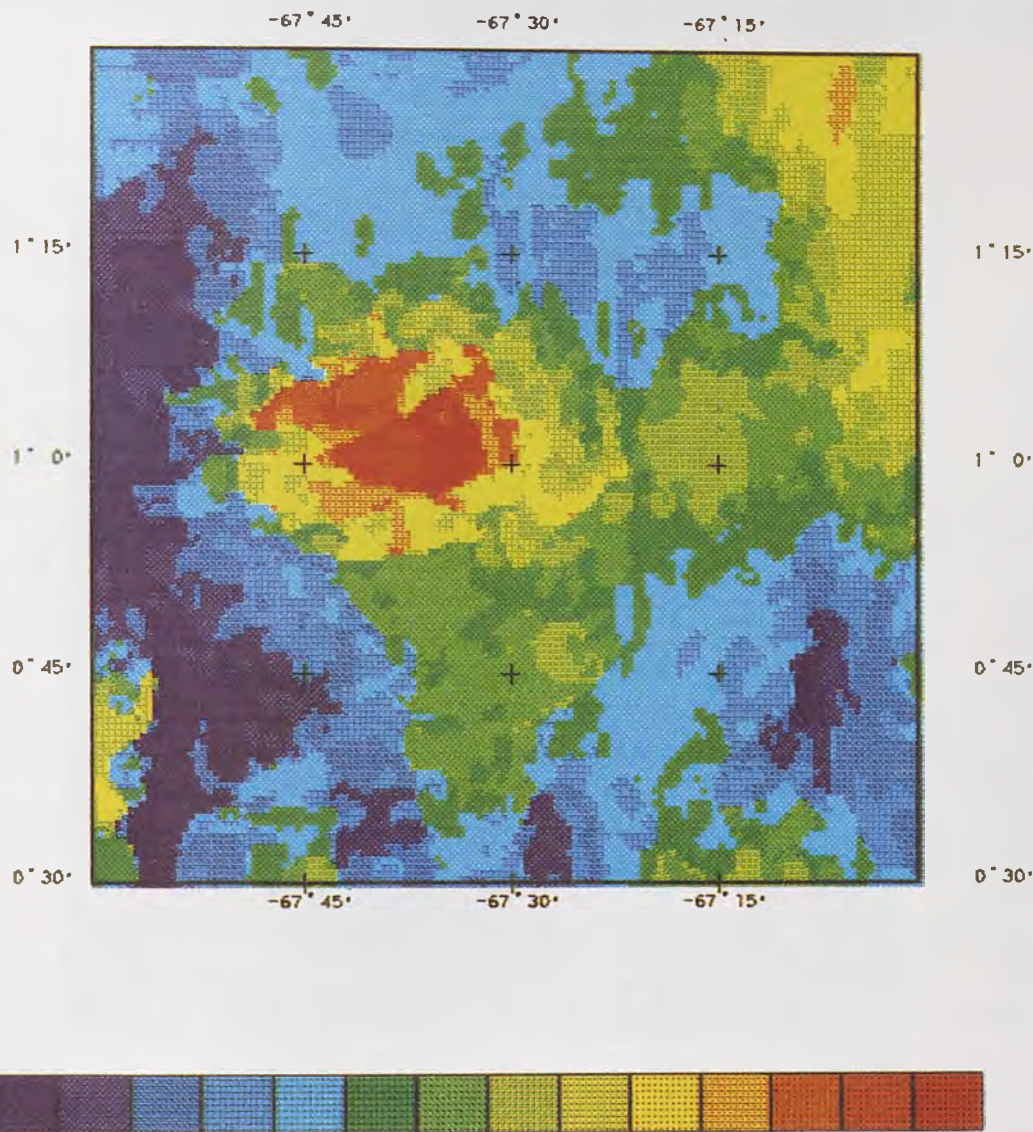


Figure 39. Terraced pseudogravity transform of the filtered second-order residual magnetic field rescaled to cgs units of magnetization ( $\text{emu.cm}^{-3}$ ). This is the first magnetization function estimate. Color level interval is  $0.00018 \text{ emu.cm}^{-3}$ .

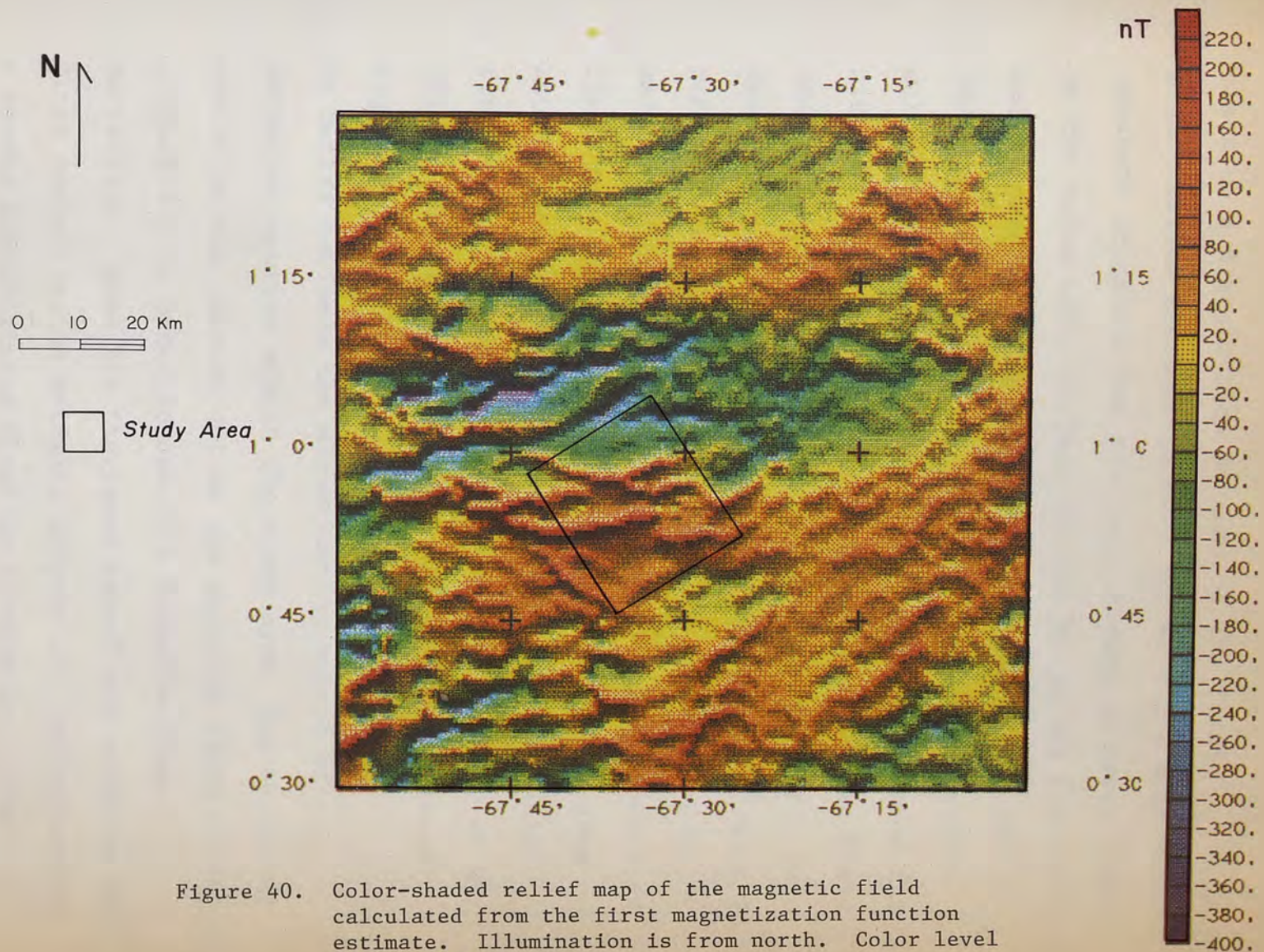


Figure 40. Color-shaded relief map of the magnetic field calculated from the first magnetization function estimate. Illumination is from north. Color level interval is 20 nT.

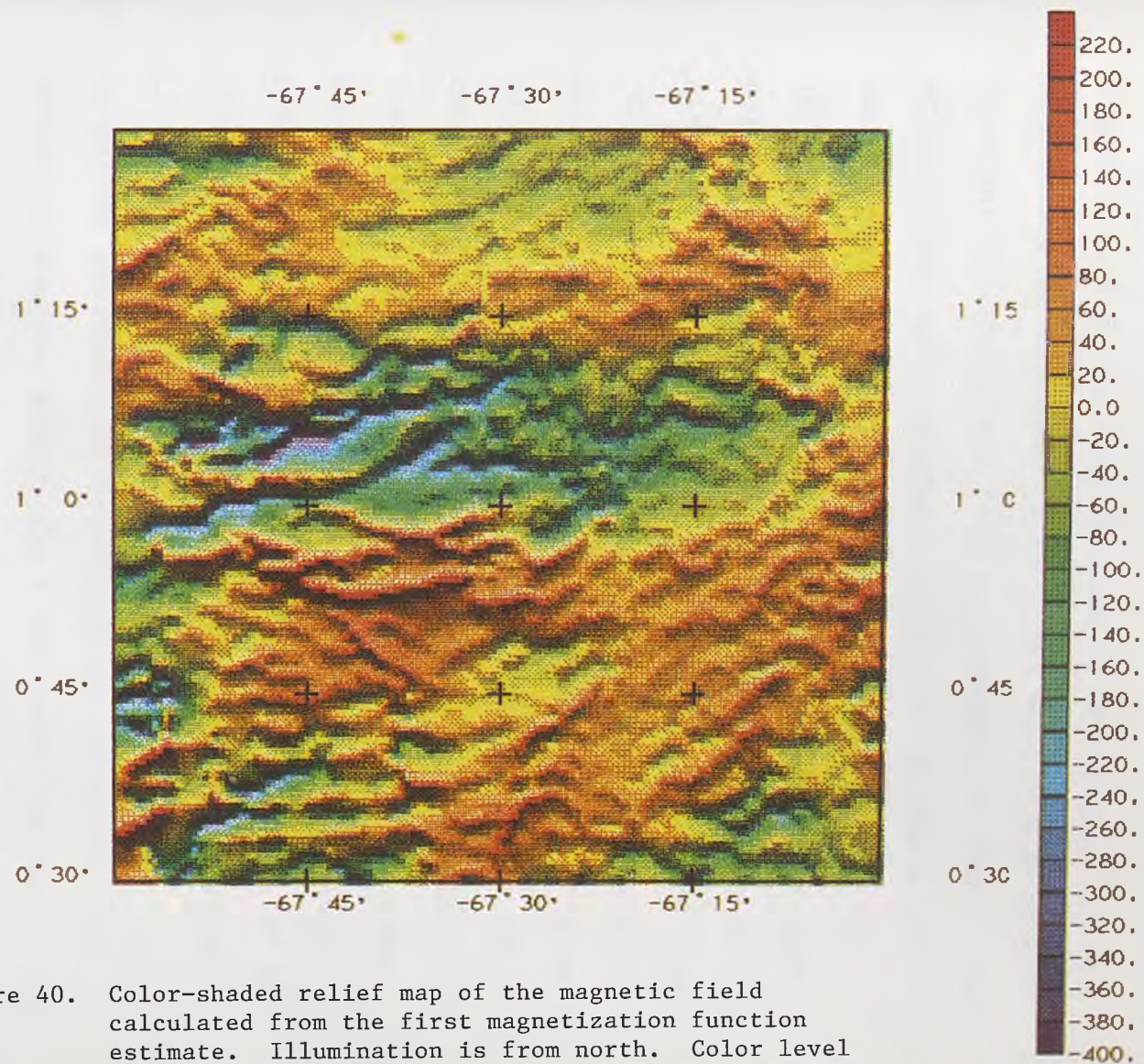


Figure 40. Color-shaded relief map of the magnetic field calculated from the first magnetization function estimate. Illumination is from north. Color level interval is 20 nT.

based on a distribution defined by the first magnetization function (Figure 39) within a slab with constant thickness and flat top, having an upper limit at the topographic surface (0.15km below the aircraft) and a lower bounding surface at a depth of 5.0 km (determined by trial and error). The first forward-calculated magnetic field showed a moderately good fit with the filtered second-order residual magnetic field (compare Figures 40 and 36). The goodness-of-fit is demonstrated by the magnetic field error map (Figure 36 minus Figure 40; see Figure 41). The error map was calculated by subtracting the first forward calculated field from the second order residual field (program ADDGRD, Branch of Geophysics, 1989). The magnetic field error is generally in the range -40 nT to 40 nT (Figure 41), except for areas of prominent magnetic highs and lows;

- (7) to better estimate the magnetization values of causative sources within the study area, the terracing operation was carried out on the magnetic field error (Figure 41) in order to obtain a magnetization correction. When the "terraced error" was added to the first magnetization estimate (Figure 39), this provided a second magnetization function (Figure 42). The magnetic field calculated from the second magnetization

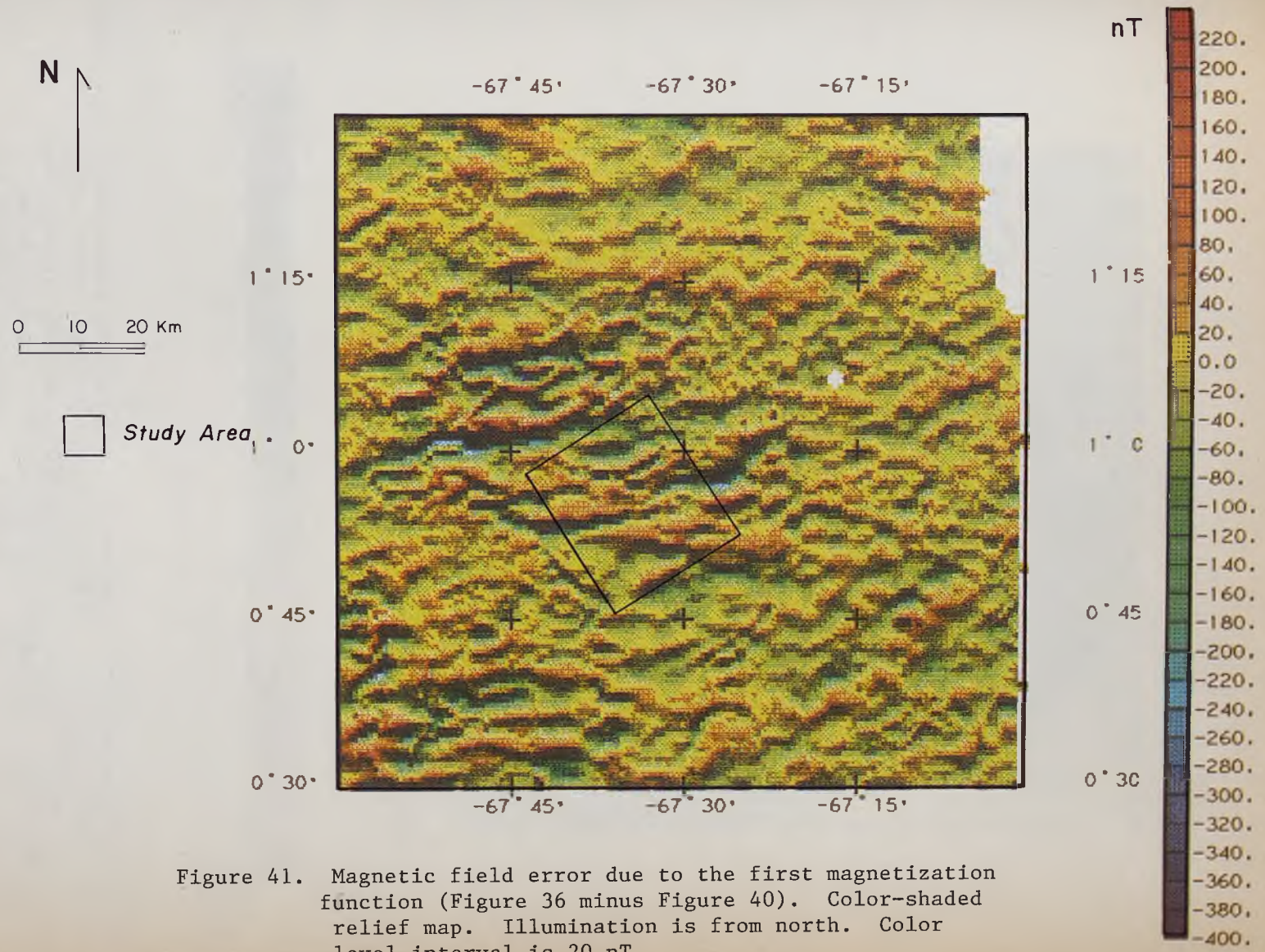


Figure 41. Magnetic field error due to the first magnetization function (Figure 36 minus Figure 40). Color-shaded relief map. Illumination is from north. Color level interval is 20 nT.

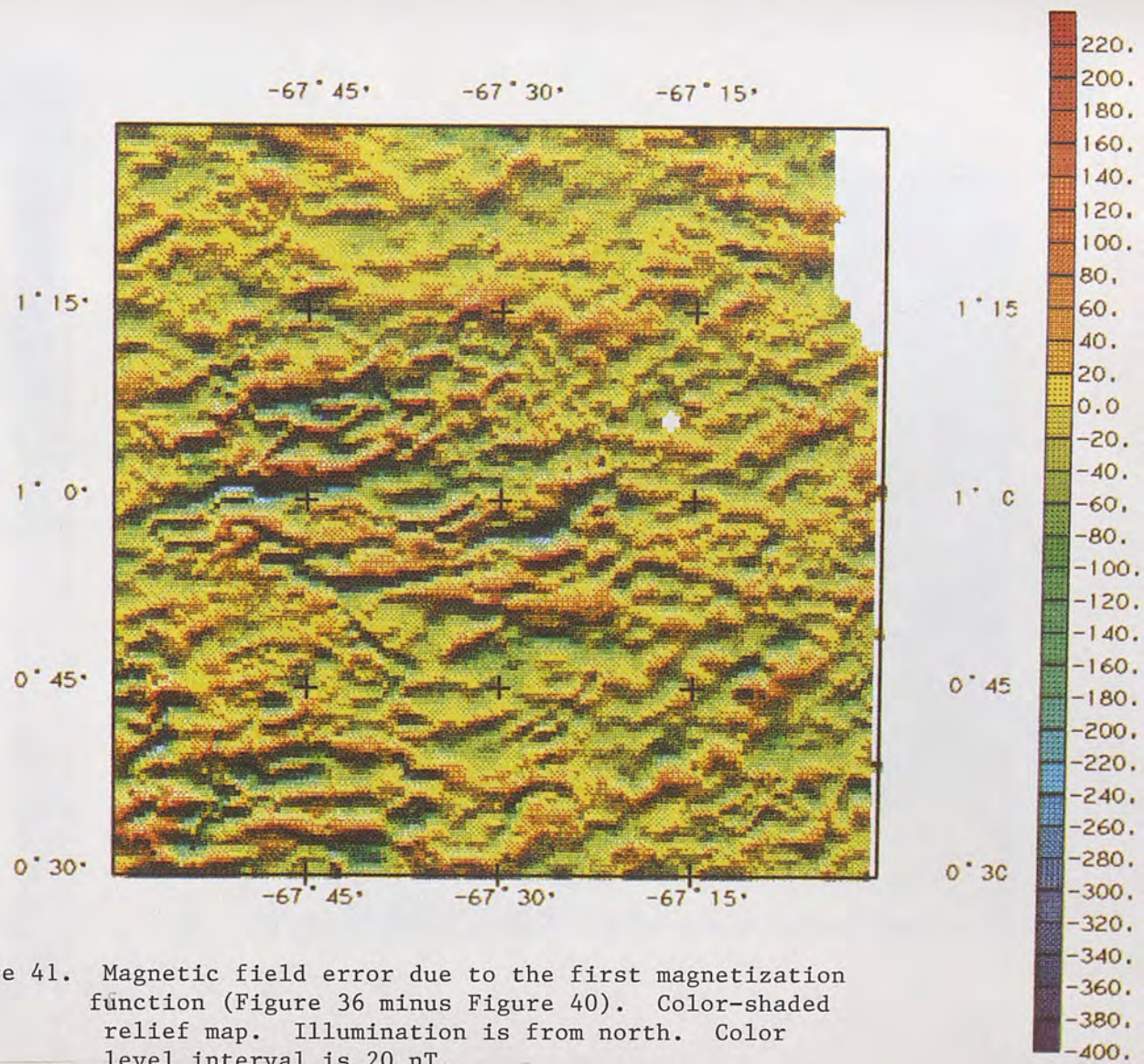


Figure 41. Magnetic field error due to the first magnetization function (Figure 36 minus Figure 40). Color-shaded relief map. Illumination is from north. Color level interval is 20 nT.



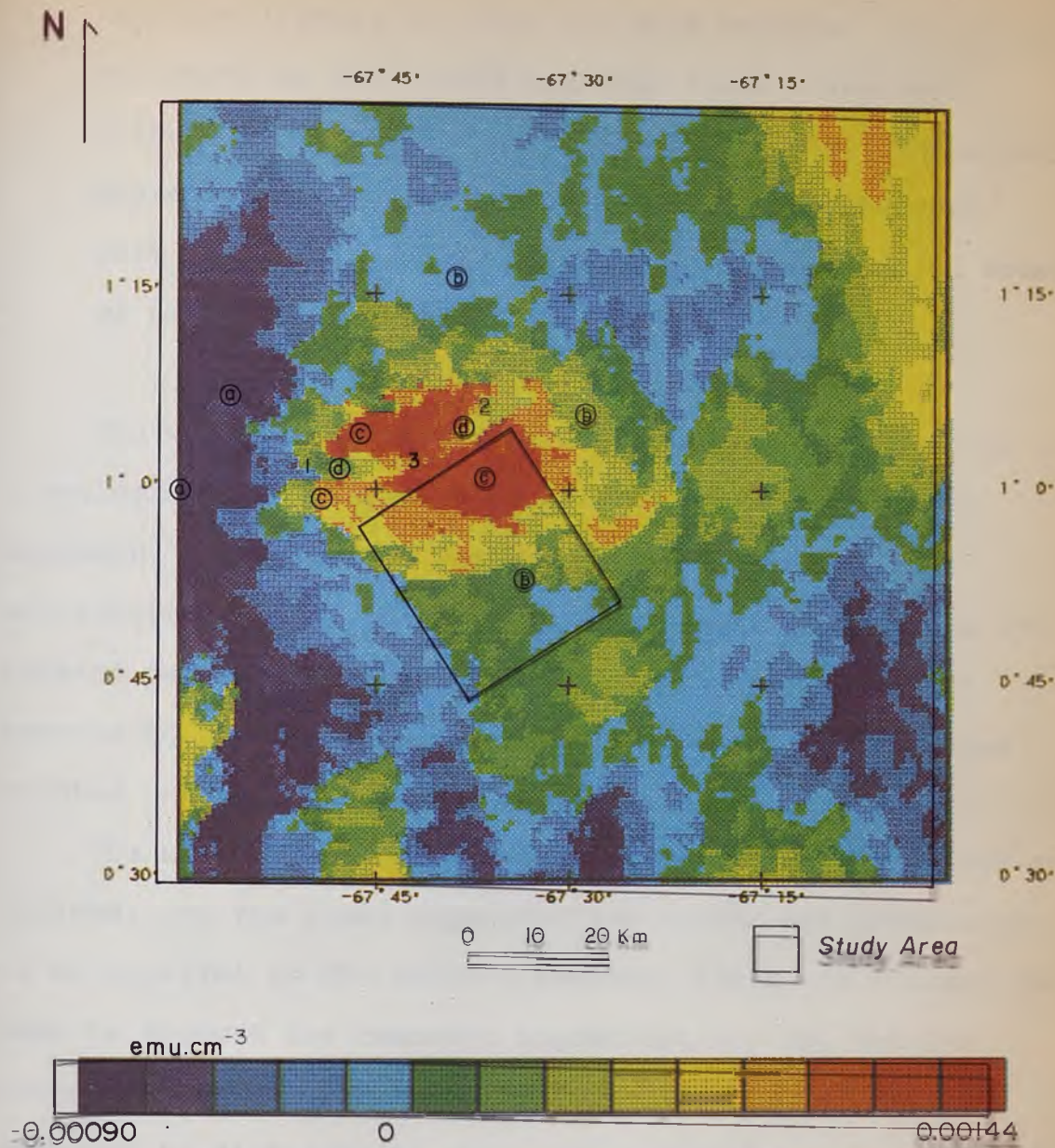


Figure 42. Second magnetization function estimate (terrace-magnetization map). Color level interval is  $0.00018 \text{ emu.cm}^{-3}$ . Magnetic patterns identified on the grey-scale magnetic image (a, b, c, and d; Plate 1) are located for comparison. See text for explanation about 1, 2 and 3.

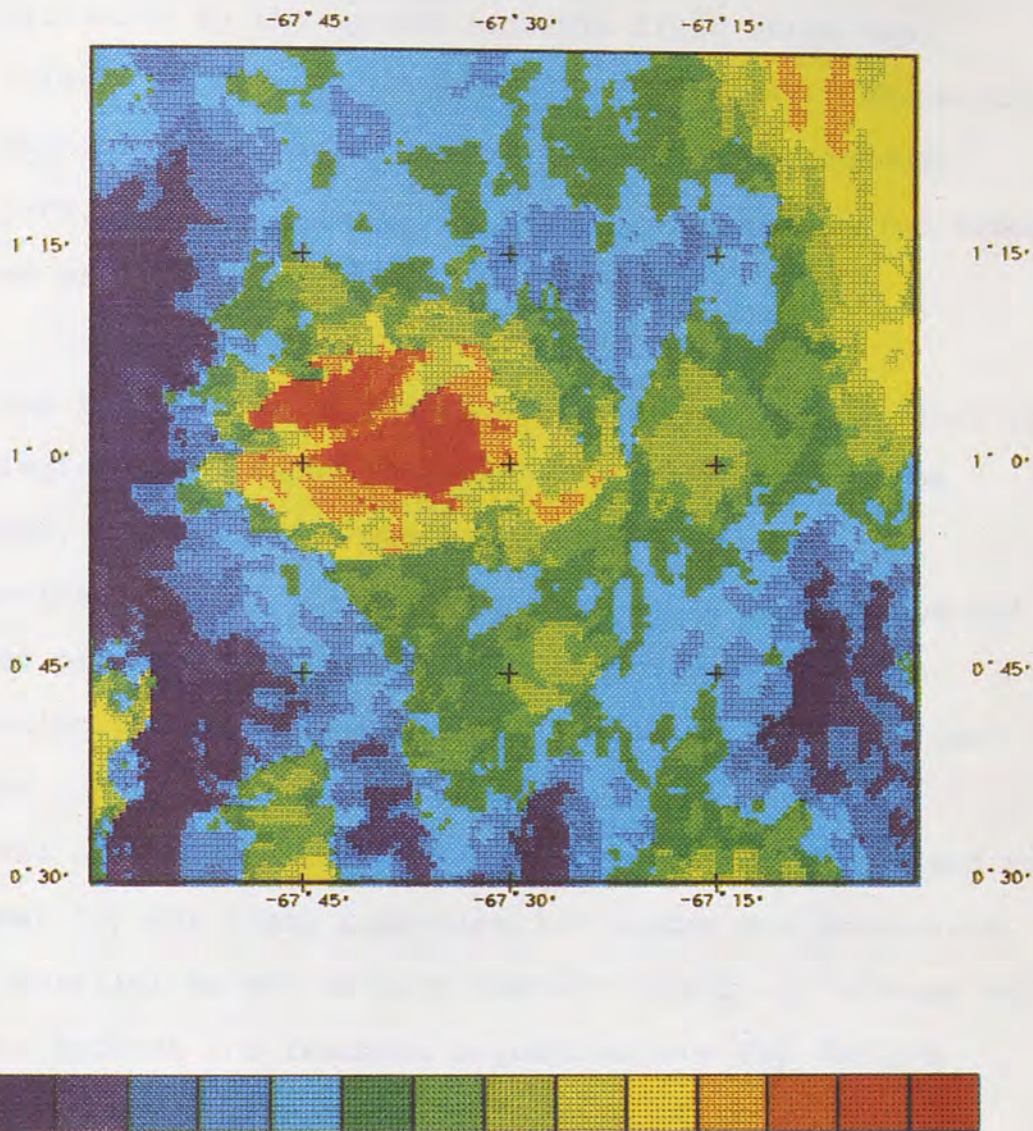


Figure 42. Second magnetization function estimate (terrace-magnetization map). Color level interval is  $0.00018 \text{ emu.cm}^{-3}$ . Magnetic patterns identified on the grey-scale magnetic image (a, b, c, and d; Plate 1) are located for comparison. See text for explanation about 1, 2 and 3.

function (Figure 43) fits the data somewhat better, as evidenced by the second magnetic field error map (Figure 36 minus Figure 43; see Figure 44). The second magnetic field error is now situated, for the most part, in the range of -20 nT to 20 nT (except for areas of prominent magnetic highs and lows);

The terrace map of Figure 42 is roughly proportional to a geologic map of magnetic rocks within the crystalline basement. This product was not obtained in a totally subjective fashion, in the sense that basic assumptions and related parameters were defined a priori, whereas data-processing procedures were objective and reproducible (as pointed out by Cordell and McCafferty, 1989).

The assumptions used in this research are summarized as follows: (a) the total magnetization vector was considered to be parallel to the Earth's magnetic field, no attempt was made to account for remanent magnetization; (b) the 2-D magnetization distributions of Figures 39 and 42 were expanded to fill a thick slab. Magnetization values varied laterally across domains but not vertically within domain boundaries; (c) Magnetic sources were assumed to be relatively close to the topographic surface and therefore a flat surface was used in the forward calculation. A slab thickness of 5.0 km was chosen for the model because this

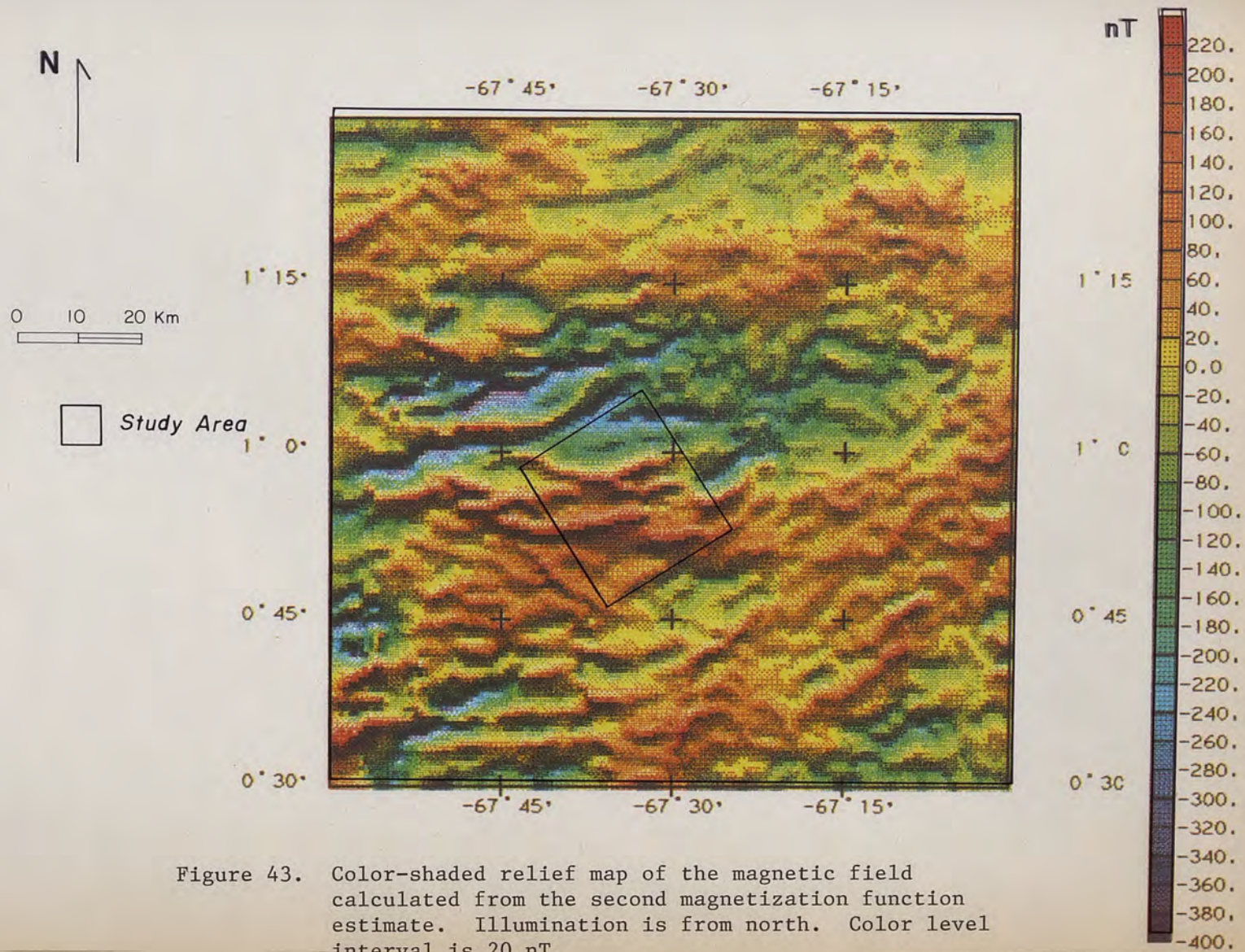


Figure 43. Color-shaded relief map of the magnetic field calculated from the second magnetization function estimate. Illumination is from north. Color level interval is 20 nT.

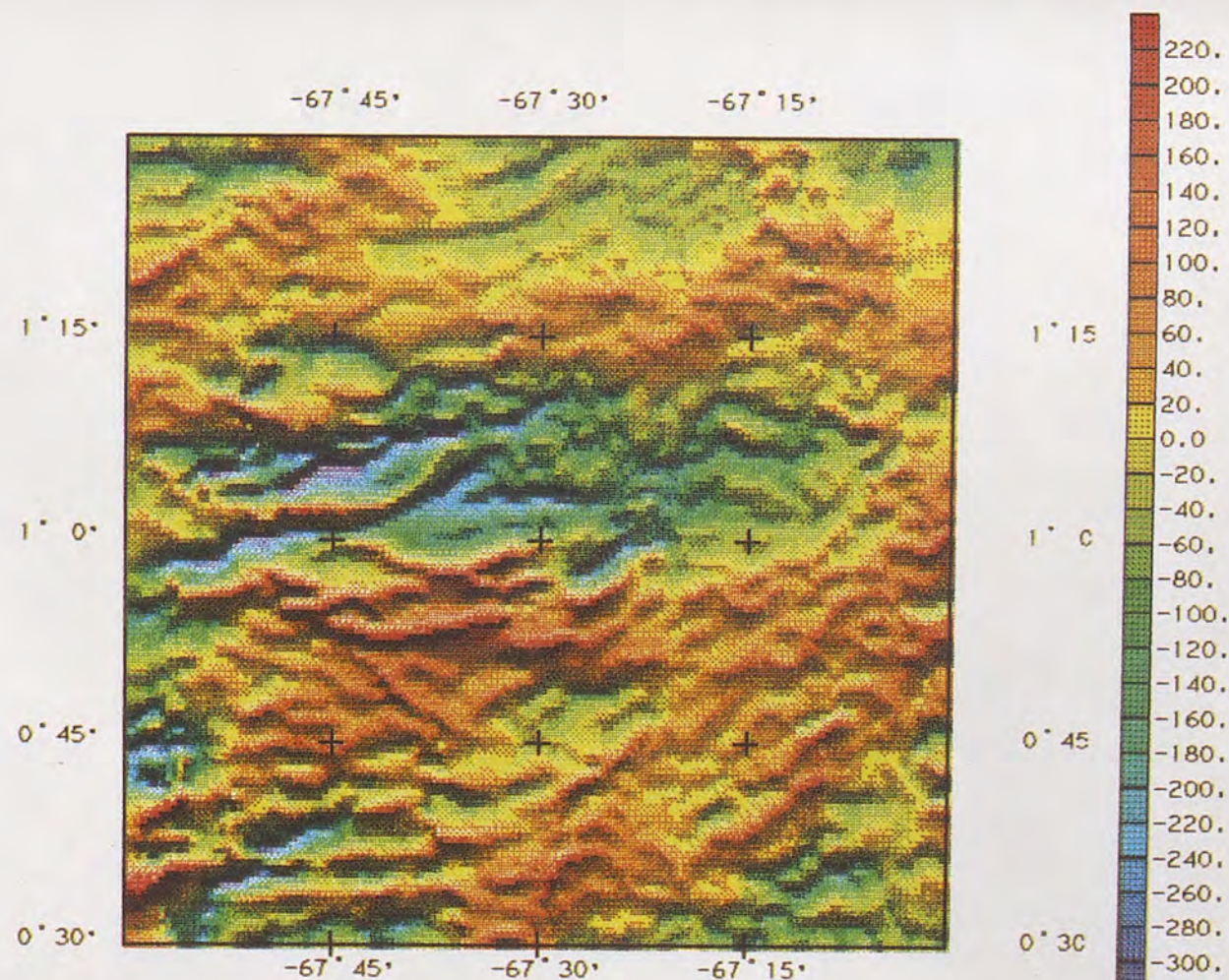


Figure 43. Color-shaded relief map of the magnetic field calculated from the second magnetization function estimate. Illumination is from north. Color level interval is 20 nT.

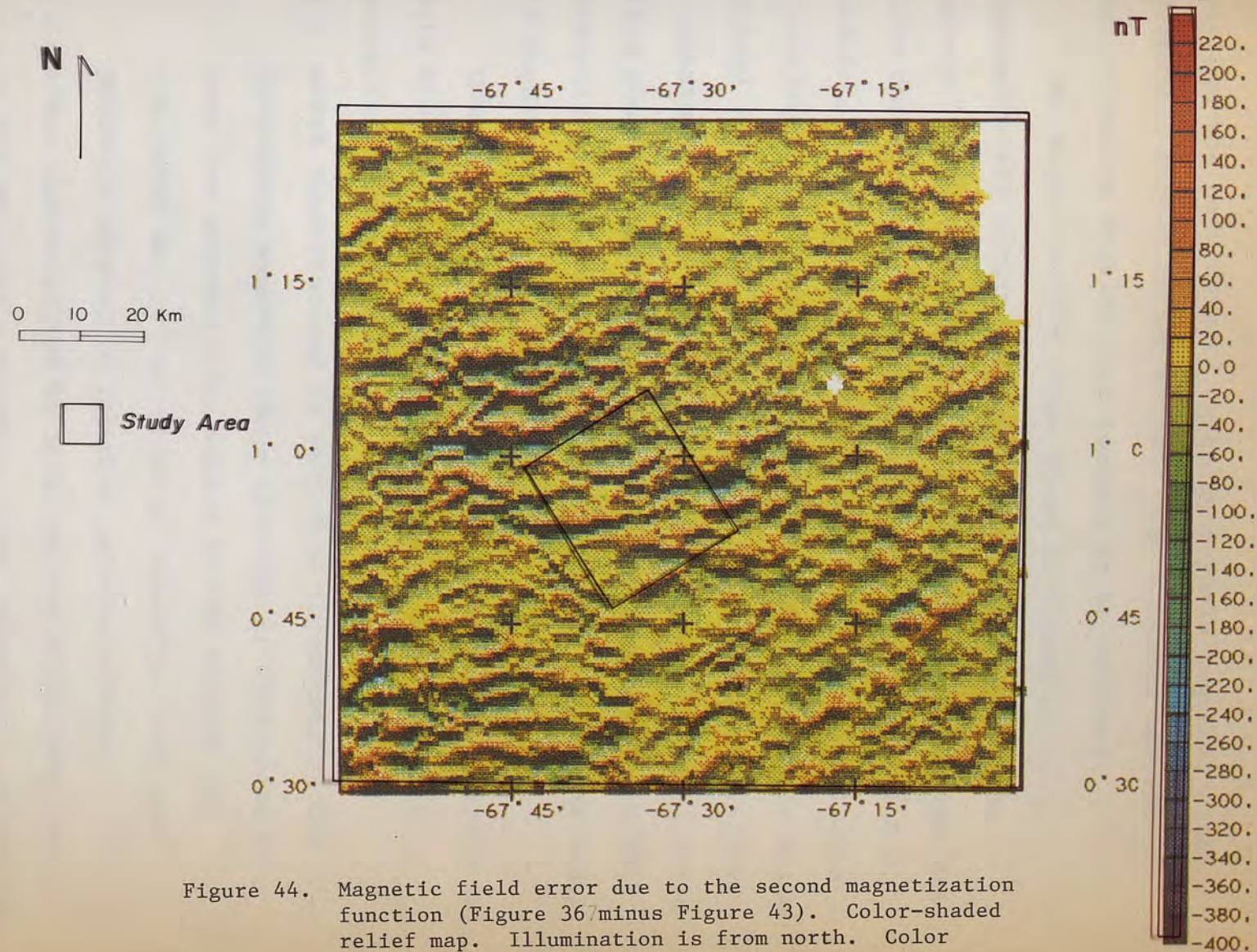


Figure 44. Magnetic field error due to the second magnetization function (Figure 36 minus Figure 43). Color-shaded relief map. Illumination is from north. Color level interval is 20 nT.

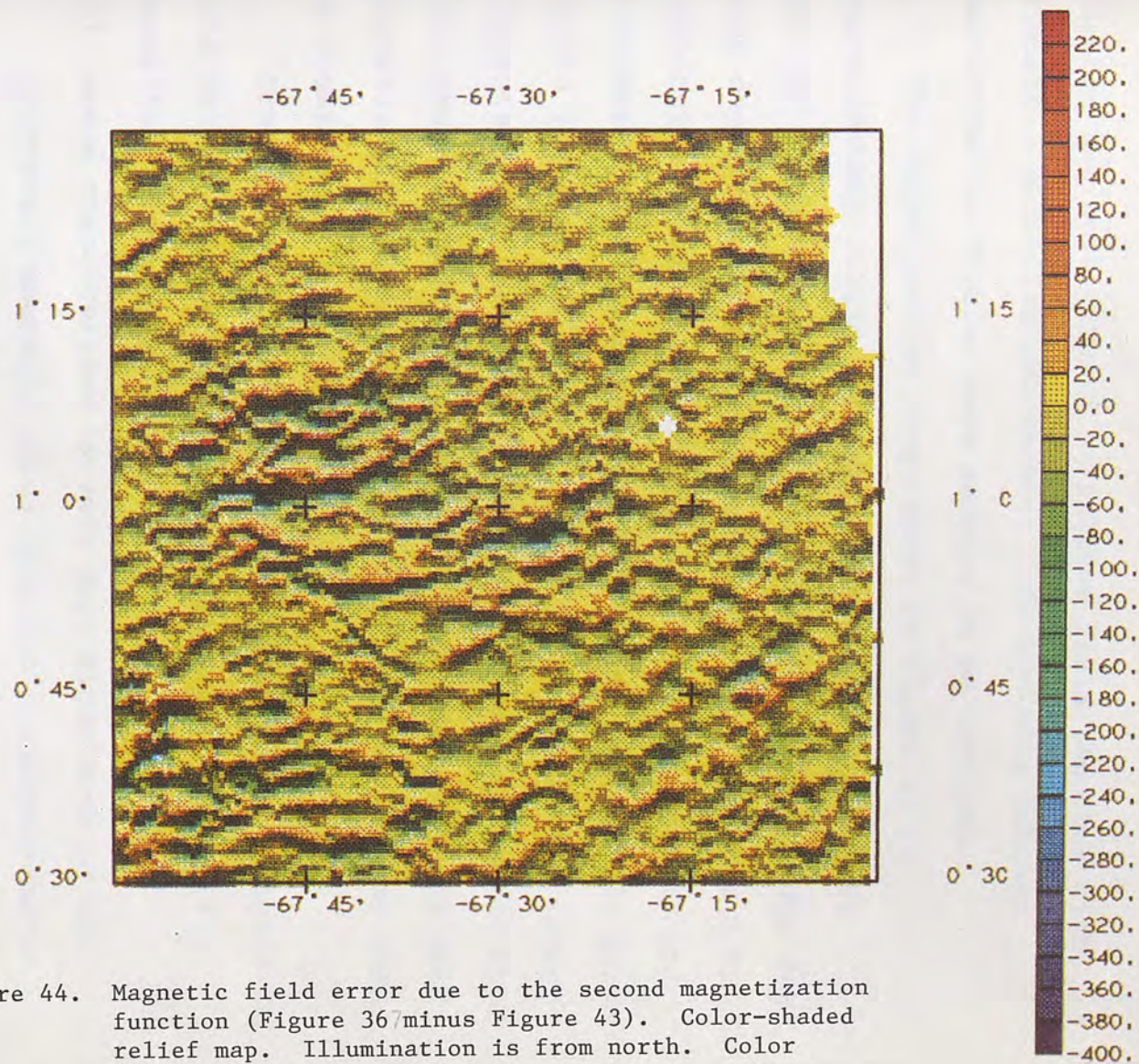


Figure 44. Magnetic field error due to the second magnetization function (Figure 367 minus Figure 43). Color-shaded relief map. Illumination is from north. Color level interval is 20 nT.

yielded the best forward calculated field together with plausible magnetization values; (d) contacts between magnetization domains were assumed to be vertical.

The magnetization range shown in Figure 42 is approximately within one order of magnitude ( $-0.00090$  emu.cm<sup>-3</sup> to  $0.00144$  emu.cm<sup>-3</sup>). A similarly narrow range has been observed in terrace-magnetization maps from the U.S. Midcontinent region (McCafferty et al., 1989; Cordell and McCafferty, 1989) and from the Venezuelan part of the Guiana Shield (Wynn et al., 1990). Cordell and McCafferty (1989) suggested that (a) geologic units may have a characteristic bulk magnetization at map scale, and (b) variation of bulk magnetization among most geologic units is within one order of magnitude.

Comparison of the terrace-magnetization map (Figure 42) with the grey-scale image of reduced-to-pole magnetic anomalies (Plate 1) revealed that:

- (1) areas characterized by very dark signatures on the grey-scale magnetic image (pattern a) correspond to very low magnetization values on the terrace map ( $-0.00090$  emu.cm<sup>-3</sup> to  $-0.00018$  emu.cm<sup>-3</sup>). They are probably related to two-mica granite plutons;
- (2) areas characterized by intermediate brightness levels on the grey-scale magnetic image (pattern b) correspond to low to intermediate magnetization values on the



terrace map ( $-0.00018 \text{ emu.cm}^{-3}$  to  $0.00090 \text{ emu.cm}^{-3}$ ).

They are probably related to gneisses;

- (3) magnetically high areas characterized by very bright signatures on the grey-scale image (pattern c) correspond to high terrace-magnetization values (greater than  $0.00090 \text{ emu.cm}^{-3}$ ). They are probably related to magnetic granites;
- (4) the dike-like magnetic feature (pattern d) cross-cutting pattern c on the grey-scale image (Plate 1) is also expressed on the terrace magnetization map (Figure 42). It is probably related to a discordant intrusive body. Magnetization values are lower westward (about  $0.00018 \text{ emu.cm}^{-3}$ ; point 1 on Figure 42) than eastward (about  $0.00072 \text{ emu.cm}^{-3}$ ; point 2). Terrace-magnetization values are as high as  $0.00108 \text{ emu.cm}^{-3}$  in the center of this feature (point 3).

A map of magnetization units (Figure 45) was developed based on the information derived from the grey-scale image and the terrace map. The magnetization units were tentatively defined as follows:

- magnetization unit 1: values ranging from  $-0.00090 \text{ emu.cm}^{-3}$  to  $-0.00018 \text{ emu.cm}^{-3}$ ; magnetic pattern a on Plate 1;

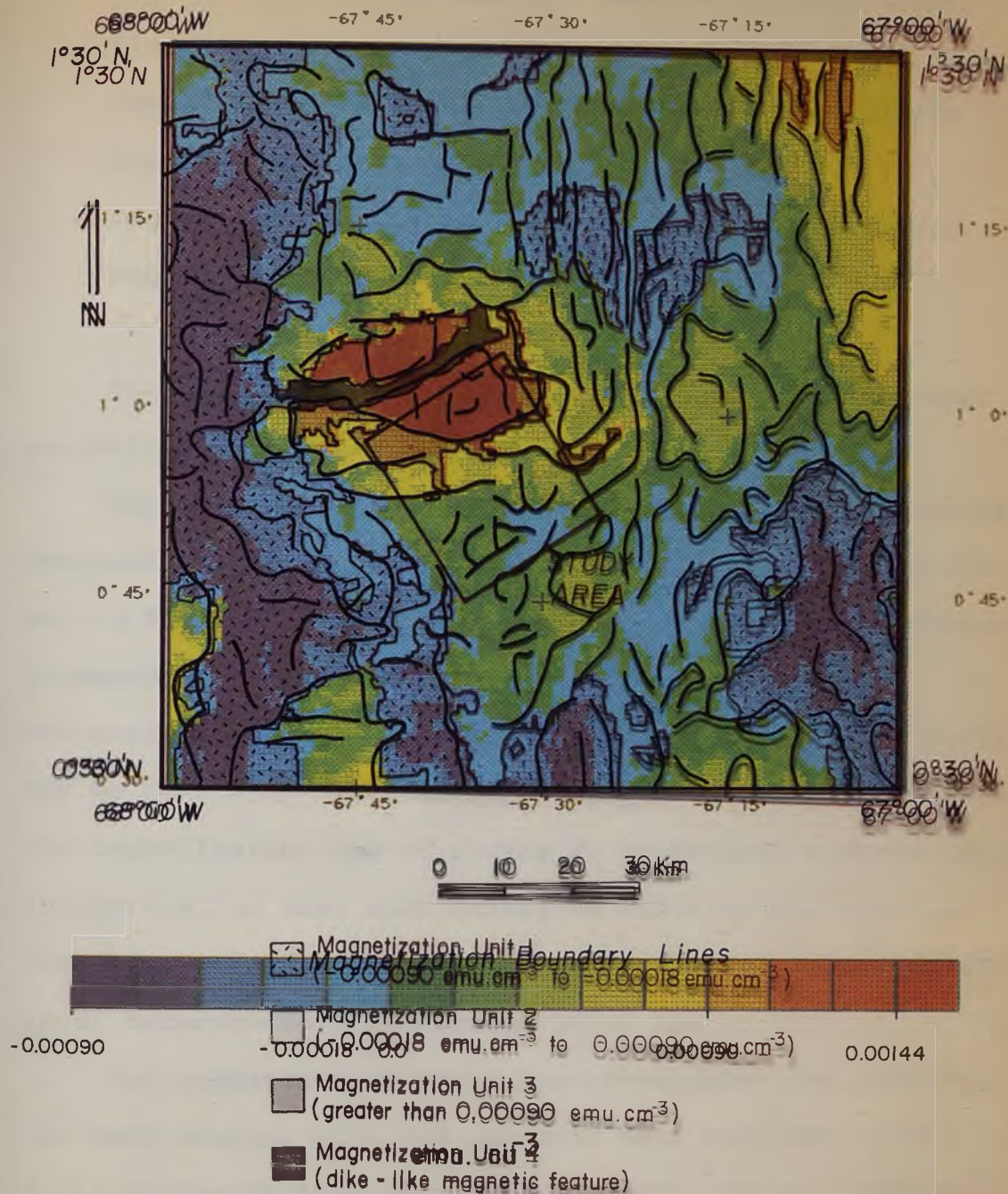


Figure 45. Map of magnetization units. Boundary lines of Figure 38 are superimposed for comparison.

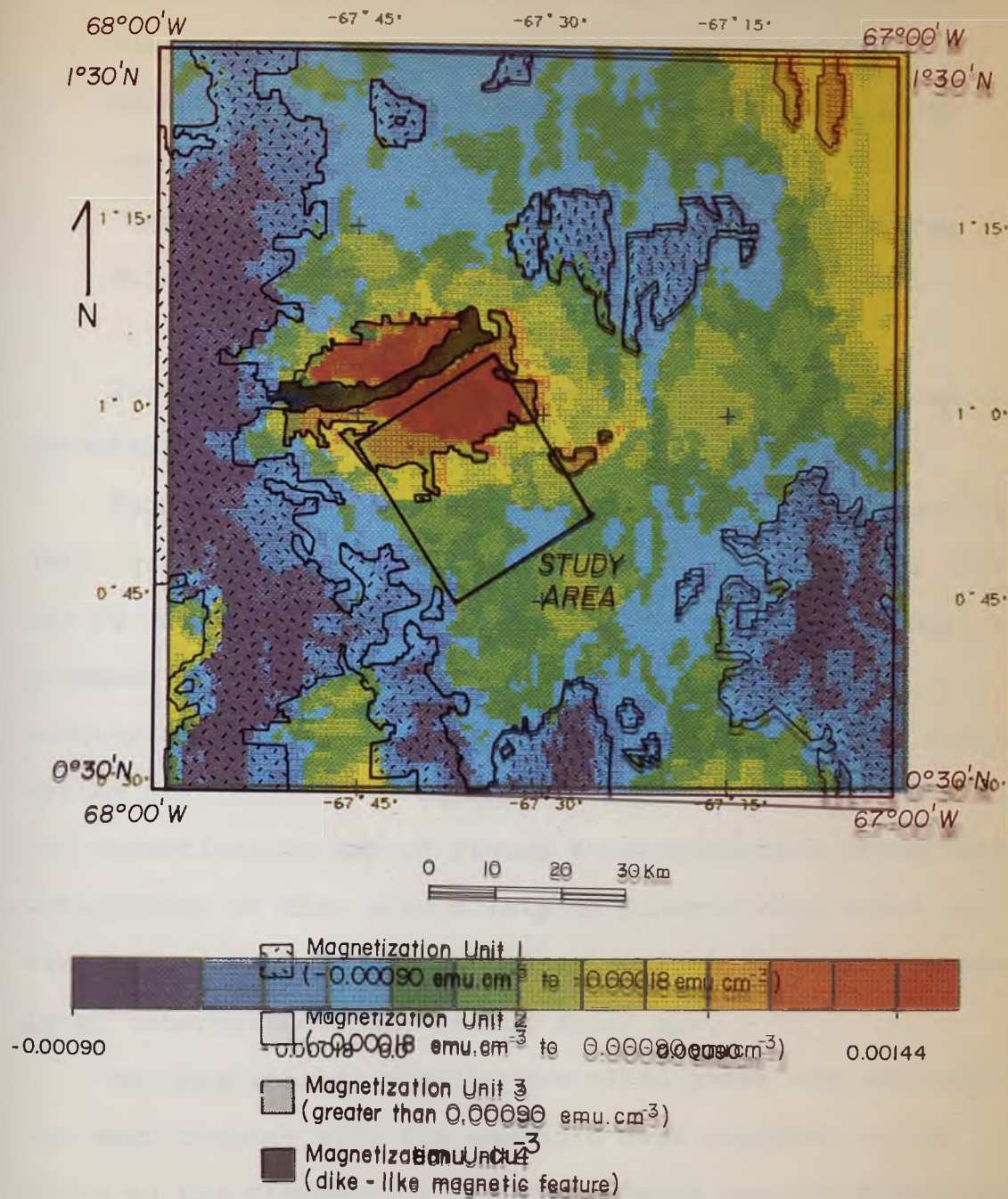
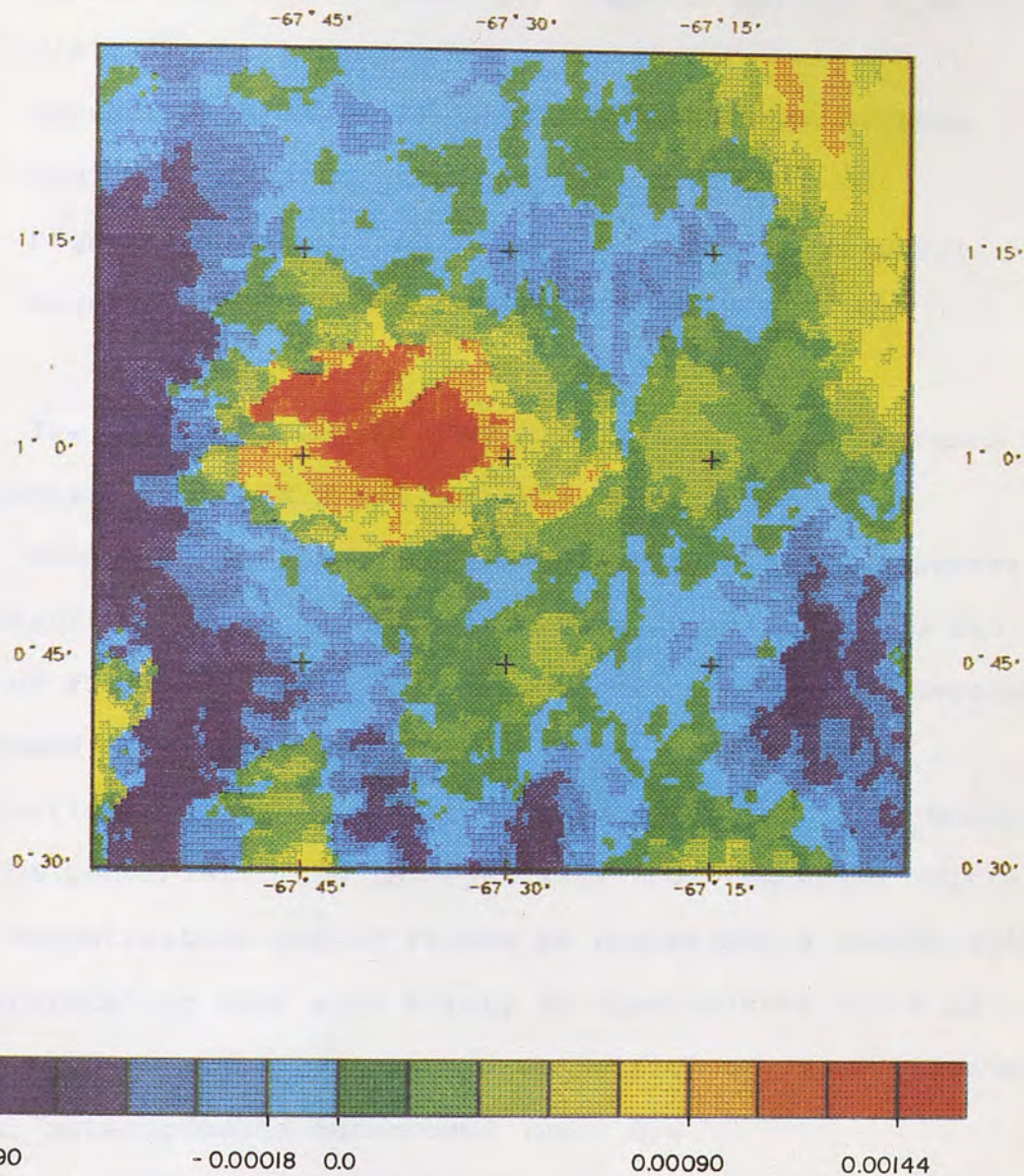


Figure 45. Map of magnetization units. Boundary lines of Figure 38 are superimposed for comparison.



emu. cu<sup>-3</sup>

Figure 45. Map of magnetization units. Boundary lines of Figure 38 are superimposed for comparison.

- magnetization unit 2: values ranging from  $-0.00018$   $\text{emu.cm}^{-3}$  to  $0.00090$   $\text{emu.cm}^{-3}$ ; magnetic pattern b on Plate 1;
- magnetization unit 3: values greater than  $0.00090$   $\text{emu.cm}^{-3}$ ; magnetic pattern c on Plate 1;
- magnetization unit 4: dike-like magnetic feature; magnetic pattern d on Plate 1.

The area of study is characterized by the occurrence of magnetization units 2 and 3 (Figure 45).

Magnetization boundaries determined by the horizontal-gradient-of-pseudogravity method were superimposed to the map of Figure 45. Many boundaries coincide with borders of proposed magnetization units. However, many other boundaries suggest that further subdivision of those units may be possible. This is especially true regarding unit 2. The magnetization map of Figure 45 represents a conservative interpretation that aims solely to discriminate areas of very high and very low magnetization from an intermediate-level heterogeneous background (unit 2).

The magnetization units described above are compared in the next chapter with the geologic data acquired in the field by the RADAMBRASIL Project. Broad terrane categories were delineated for the first time as a result of this comparison. In addition, areas of agreement between

magnetization boundary lines (Figure 38) and SIR-B linear features (Figure 31) were interpreted as geologic structures in the magnetic basement having topographic expression. None of these features have been previously reported by the RADAMBRASIL Project.

The magnetic basement is composed of igneous and metamorphic rocks of the Precambrian and Paleoproterozoic eras. The magnetic basement is characterized by the presence of magnetite and hematite minerals. The magnetic basement is also characterized by the presence of linear features, which are interpreted as geologic structures. The magnetic basement is also characterized by the presence of magnetization boundary lines, which are interpreted as geologic structures. The magnetic basement is also characterized by the presence of SIR-B linear features, which are interpreted as geologic structures.

CONDICIONES DE SIR-B EN EL AREA ESTUDIADA

Las condiciones de SIR-B en el área estudiada son las siguientes: (1) la presencia de magnetita y hematita en el sustrato magnético; (2) la presencia de estructuras geológicas lineales; (3) la presencia de líneas de límite de magnetización; (4) la presencia de características lineales SIR-B.

## CHAPTER VI

RECONNAISSANCE GEOLOGIC MAP DERIVED FROM  
SPACEBORNE RADAR AND AEROMAGNETIC INFORMATION

This chapter presents the reconnaissance geologic map derived from the integrated analysis of spaceborne radar (SIR-B) and aeromagnetic information. The steps involved in the production of such a map were (a) comparison of SIR-B linear features with the terrace map and magnetization boundary lines in order to identify magnetic basement structures having topographic expression; (b) comparison of terrace-magnetization units with geologic data acquired in the field by the RADAMBRASIL Project in order to delineate broad terrane categories; (c) integration of the information generated in steps (a) and (b) in order to outline the geologic framework of the study area.

COMPARISON OF SIR-B LINEAR FEATURES WITH THE  
TERRACE MAP AND MAGNETIZATION BOUNDARY LINES

Magnetic basement structures having topographic expression were identified in the study area by comparing SIR-B linear features (Figure 31) to the terrace map (Figure 42) and magnetization boundary lines (Figure 38). These structures were recognized according to the following criteria:

- (1) the horizontal-gradient method of Cordell and Grauch

- (1985) assumes that magnetic boundaries with geologic significance can be piecewise approximated as single, near-vertical, sharp contacts. Maximum values of the horizontal gradient of pseudogravity are located directly over these near-vertical contacts. These maxima define the position of magnetization boundary lines;
- (2) SIR-B linear features may represent the intersection of structural discontinuities in the magnetic basement with the topographic surface;
  - (3) SIR-B linear features coinciding with magnetization boundary lines are interpreted as the trace on the topographic surface of near-vertical structural discontinuities within the magnetic basement;
  - (4) SIR-B linear features offset from magnetization boundary lines indicate that magnetic contacts are not well represented by near-vertical geologic structures. Alternative interpretations are (a) geologic structures are not steeply dipping, (b) geologic contacts are gradational, (c) magnetic sources are superimposed, (d) several geologic boundaries are close together (Grauch and Cordell, 1987);
  - (5) SIR-B linear features truncating magnetization boundary lines are interpreted as the surface expression of geologic structures cutting zones of abrupt lateral



changes in magnetization.

Figure 46 shows SIR-B linear features and magnetization boundary lines overlaid to the terrace-magnetization map of the study area. Examination of this illustration indicates that:

- (1) SIR-B linear feature O strikes N80W and coincides with a magnetization boundary line (MBL-1 on Figure 46). It is interpreted as the trace of a near-vertical fault on the topographic surface;
- (2) SIR-B linear feature P strikes E-W and is aligned with feature O. It approximately coincides with a magnetization boundary line (MBL-2) and is considered to be the trace of a near-vertical fault on the topographic surface;
- (3) SIR-B linear features F and G strike E-W and are offset from magnetization boundary line MBL-3. This indicates that magnetization boundaries in this area are not well represented by near-vertical geologic structures. The same interpretation can be applied to feature H, which is subparallel to the course of the Piraiuara River and is significantly offset from MBL-3. Lacking geologic constraints, features F, G, and H are tentatively considered as the surface expression of non-vertical geologic structures affecting the magnetic basement;

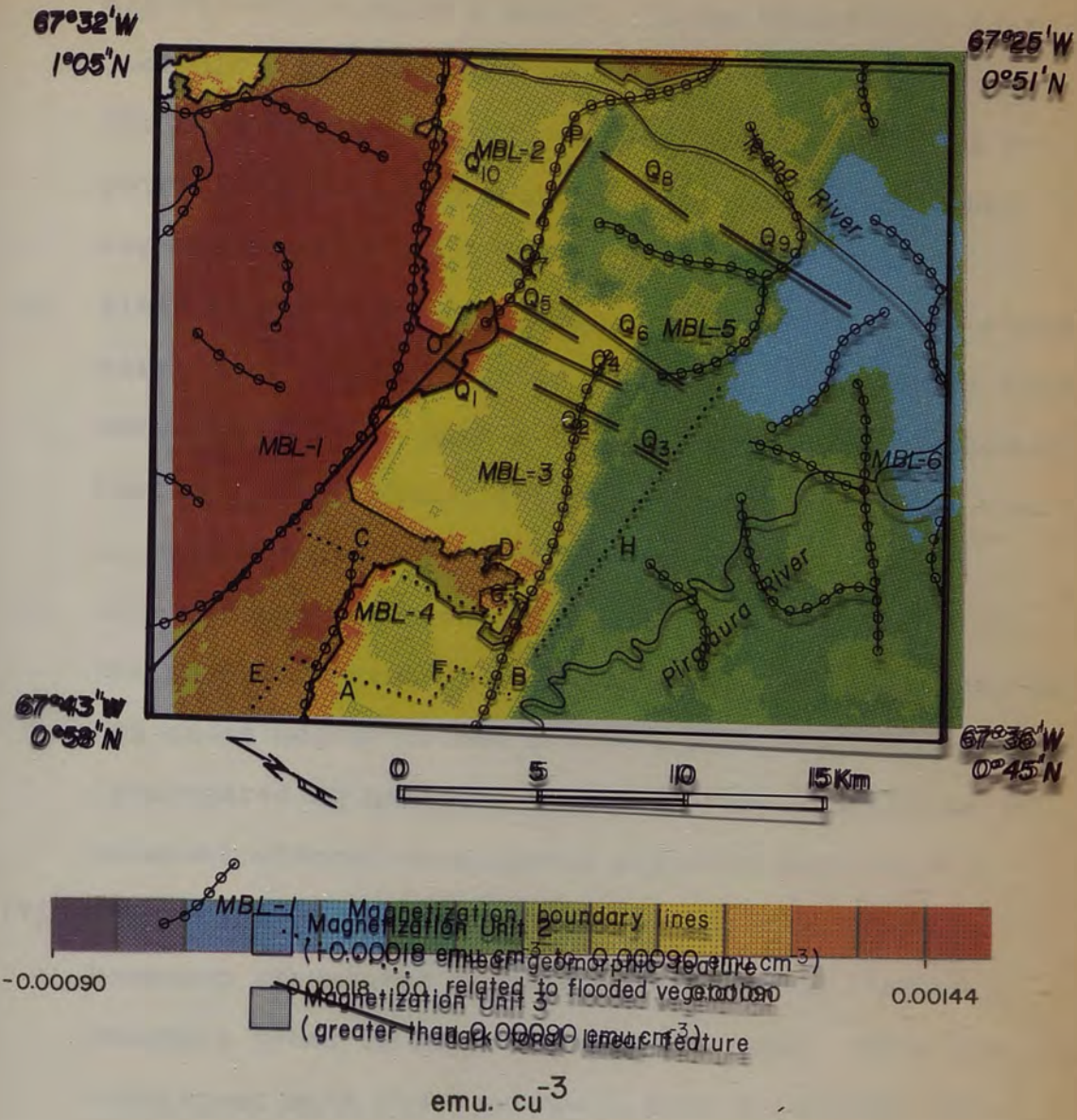


Figure 46. SIR-B linear features and magnetization boundary lines overlaid to the terrace-magnetization map of the study area.

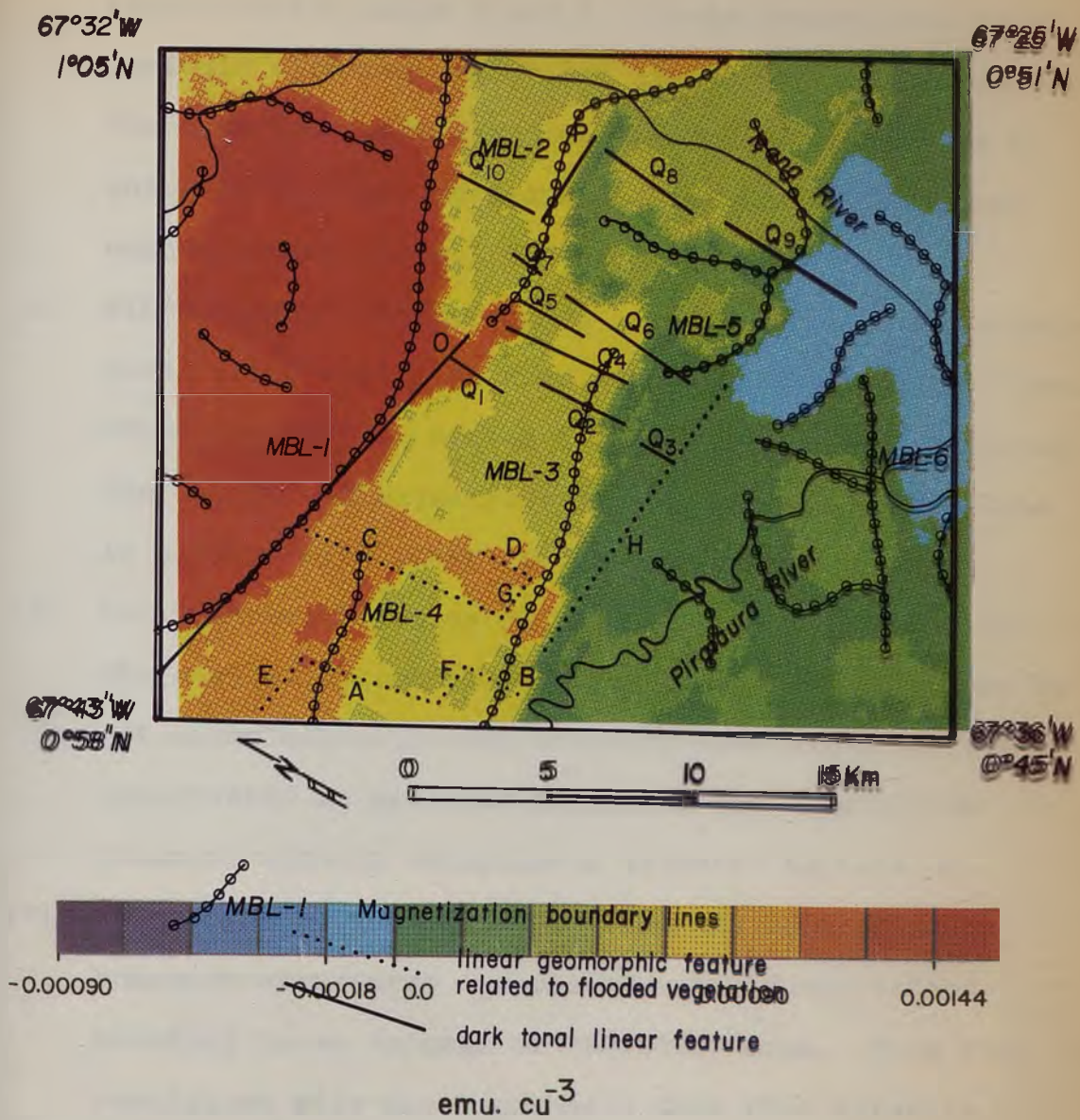


Figure 46. SIR-B linear features and magnetization boundary lines overlaid to the terrace-magnetization map of the study area.

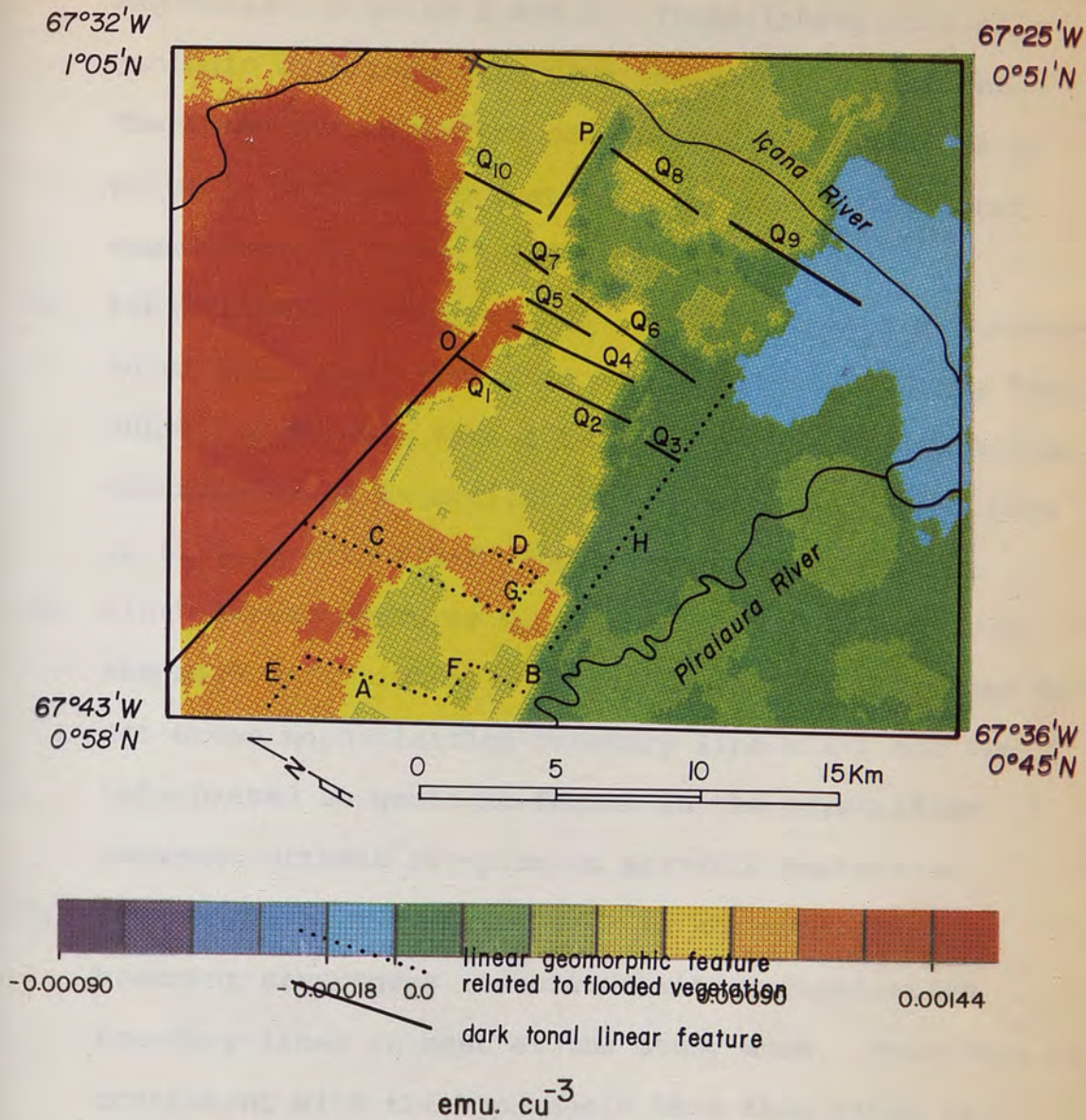
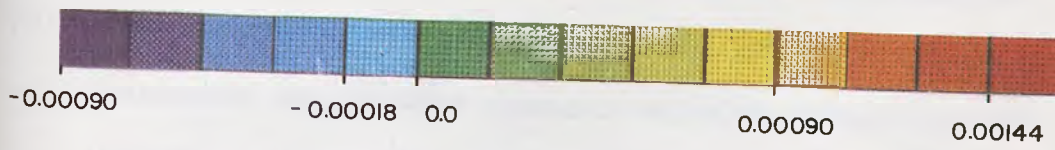
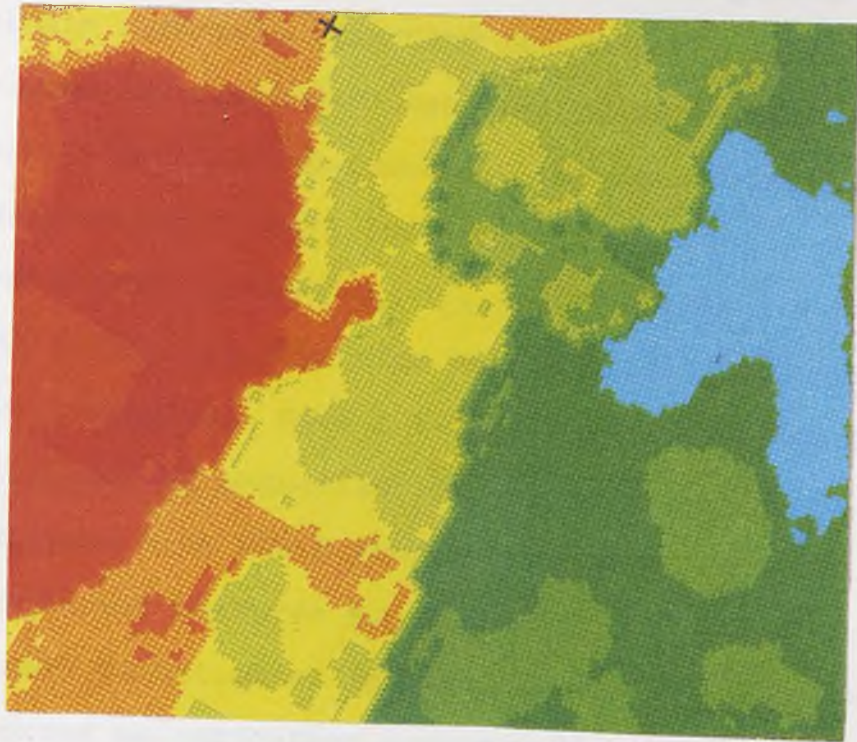


Figure 46. SIR-B linear features and magnetization boundary lines overlaid to the terrace-magnetization map of the study area.



emu. cu<sup>-3</sup>

Figure 46. SIR-B linear features and magnetization boundary lines overlaid to the terrace-magnetization map of the study area.

- (4) SIR-B linear feature C truncates magnetization boundary line MBL-4 and is coincident with the limit between magnetization units 2 and 3. It is interpreted as a geologic structure affecting the magnetic basement. The same interpretation can be applied to feature D, which is parallel to feature C and also delimitates magnetization units 2 and 3;
- (5) SIR-B linear features  $Q_4$ ,  $Q_5$ , and  $Q_6$  define a N-S structural trend that truncates magnetization boundary lines MBL-3 and MBL-5. Such a trend is in turn truncated by the segment of magnetization boundary line MBL-2 that is aligned with SIR-B linear feature O;
- (6) SIR-B linear features  $Q_7$ ,  $Q_8$ , and  $Q_{10}$  are oriented in the same direction of features  $Q_4$ ,  $Q_5$ , and  $Q_6$ . They do not cross magnetization boundary line MBL-2 and are interpreted as geologic faults in the crystalline basement without conspicuous magnetic expression;
- (7) the course of the Içana River is not controlled by basement structures associated with magnetization boundary lines in most of the study area. This fact is consistent with the hypothesis that this river is actively downcutting the bedrock as a result of the southward tilting of the Rio Branco-Rio Negro Pediplane. MBL-6 is an exception to this behavior, since it controls the location of a prominent meander in the

Içana River. This magnetization boundary line is considered to be associated with a geologic fault expressed at the surface as a subtle topographic high striking N55E. This was not identified as a SIR-B linear feature because it is parallel to the radar illumination direction (N57E);

- (8) SIR-B linear features A, B, E, Q<sub>1</sub>, Q<sub>2</sub>, Q<sub>3</sub>, and Q<sub>9</sub> show no evident relationship with magnetization boundary lines. Consequently, they are not considered in this study as the surface expression of basement geologic structures having magnetic expression.

The geologic structures with both topographic and magnetic expression identified through the comparison of SIR-B linear features, terrace map, and magnetization boundary lines were included in the reconnaissance geologic map of the study area.

COMPARISON OF TERRACE-MAGNETIZATION UNITS  
WITH GEOLOGIC DATA ACQUIRED IN THE FIELD  
BY THE RADAMBRASIL PROJECT

The comparison of terrace-magnetization units with geologic data acquired in the field by the RADAMBRASIL Project allowed the definition of broad terrane categories in the surroundings of the study site. Figure 47 shows terrace-magnetization units and magnetization boundary lines

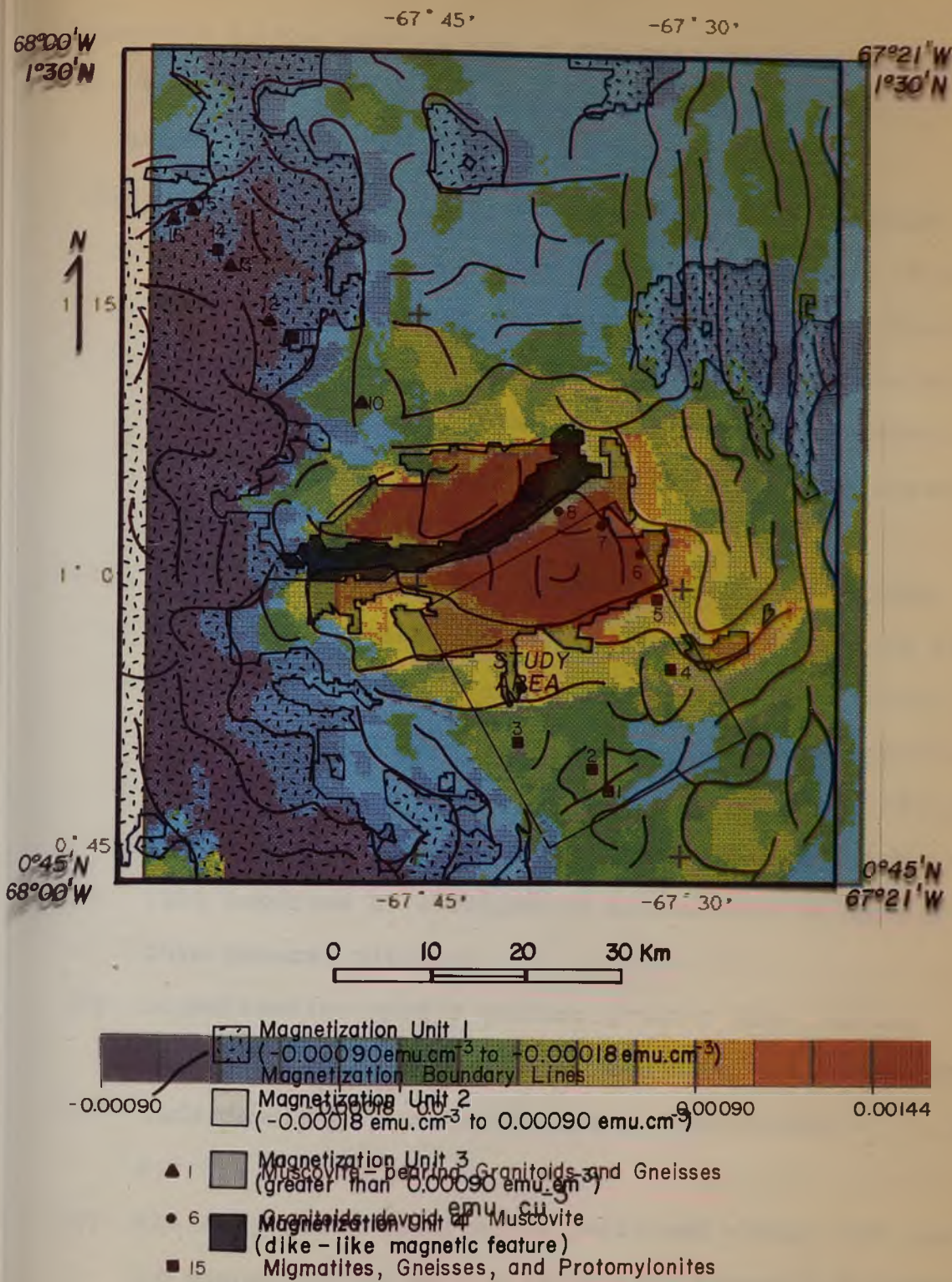


Figure 47. Terrace-magnetization units and magnetization boundary lines overlaid to the terrace-magnetization map of the area depicted in Figure 8.



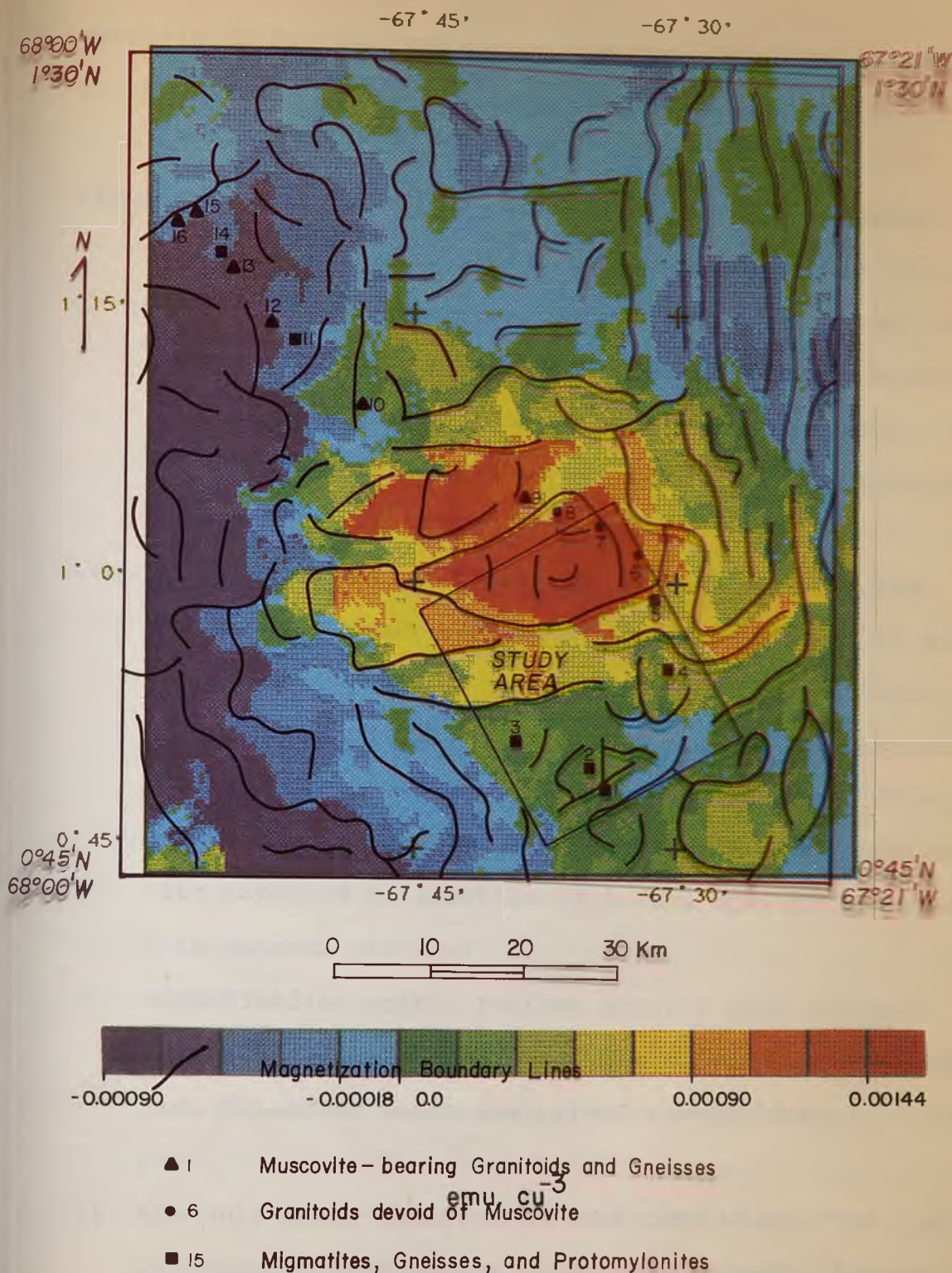


Figure 47. Terrace-magnetization units and magnetization boundary lines overlaid to the terrace-magnetization map of the area depicted in Figure 8.

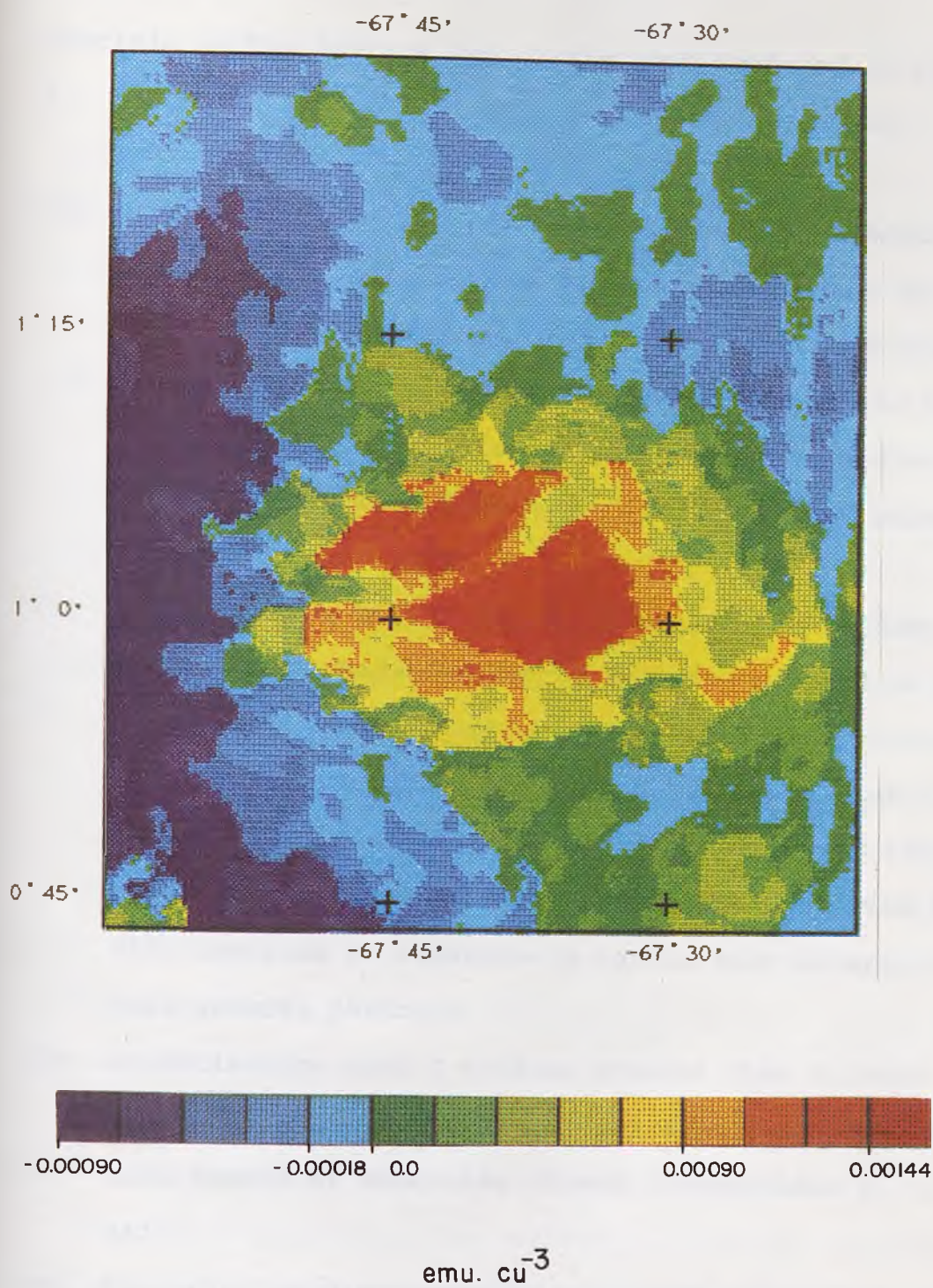


Figure 47. Terrace-magnetization units and magnetization boundary lines overlaid to the terrace-magnetization map of the area depicted in Figure 8.

overlaid to the terrace map of the area depicted in Figure 8. Examination of this illustration indicates that:

- (1) magnetization unit 1 ( $-0.00090 \text{ emu.cm}^{-3}$  to  $-0.00018 \text{ emu.cm}^{-3}$ ) is characterized by the predominance of muscovite-bearing granitoids and gneisses (field observations 12, 13, 15 and 16). The protomylonitic biotite-granite of location 14 is the only rock devoid of muscovite reported within the limits of this magnetization unit;
- (2) magnetization unit 2 ( $-0.00018 \text{ emu.cm}^{-3}$  to  $0.00090 \text{ emu.cm}^{-3}$ ) is characterized by the predominance of metamorphic rocks devoid of muscovite such as gneisses (field observations 3 and 5) and protomylonites (field observations 4 and 11), as well as migmatites (field observations 1 and 2). The biotite-granite with muscovite reported at location 10 is the only exception to this general pattern;
- (3) magnetization unit 3 (values greater than  $0.00090 \text{ emu.cm}^{-3}$ ) is characterized by the occurrence of granitoids devoid of muscovite (field observations 6, 7, and 8);
- (4) the only field observation performed within the limits of magnetization unit 4 (dike-like magnetic feature) is the muscovite-biotite granite reported at location 9.

From the discussion above, broad terrane categories of differing magnetization-intensity levels were defined in the vicinities of the study site (Figure 47): (a) areas characterized by very low values on the terrace map (magnetization unit 1) correspond to muscovite-bearing granitoids and gneisses; (b) areas characterized by low to intermediate values on the terrace map (magnetization unit 2) correspond to migmatites and metamorphic rocks devoid of muscovite; (c) areas characterized by high values on the terrace map (magnetization unit 3) correspond to granitoids devoid of muscovite; (d) the dike-like magnetic feature (magnetization unit 4) was interpreted as an intrusive body cross-cutting granitoids devoid of muscovite (magnetization unit 3). Such a feature may be an apophysis of a larger intrusive body represented by muscovite-bearing granitoids (magnetization unit 1). This interpretation is consistent with the fact that the only field observation performed within the limits of magnetization unit 4 was a muscovite-biotite granite.

A comparison of the broad terrane categories defined in this research with the geologic knowledge already existing in the Guiana Shield allowed the establishment of the following relationships:

- (1) field samples corresponding to locations 2 (migmatite) and 3 (amphibole-biotite gneiss) on Figure 47 have been

radiometrically dated. They are included in the  $1640 \pm 26$  m.y. Rb-Sr isochron obtained by Dall'Agnol and Abreu (1976) for sphene and amphibole-bearing biotite granitoids and gneisses in northwestern Brazil. The low  $Sr^{87}/Sr^{86}$  initial value for these rocks ( $0.703 \pm 0.001$ ) indicates a primary deep-seated origin, possibly a mantle derivation. Tassinari (1981) considered the sphene and amphibole-bearing biotite granitoids and gneisses to be part of the Rio Negro-Juruena magmatic arc (1.75-1.50 b.y.). In this study, the migmatites and metamorphic rocks corresponding to magnetization unit 2 were related to such a tectonic province;

- (2) a field sample corresponding to location 16 (biotite-muscovite gneiss with sillimanite) on Figure 47 has been radiometrically dated. It is included in the  $1225 \pm 23$  m.y. Rb-Sr isochron obtained by Dall'Agnol and Abreu (1976) for two-mica granitoids and gneisses in northwestern Brazil. The high  $Sr^{87}/Sr^{86}$  initial value for these rocks ( $0.713 \pm 0.002$ ) is consistent with an origin by melting of previously existing crustal material. Tassinari (1981) considered the two-mica granitoids to be the result of anorogenic plutonism taking place in the Rio Negro-Juruena Province. This event was contemporaneous with the development of the neighboring Rondonian mobile belt (1.45-1.25 b.y.). Rocks composed of

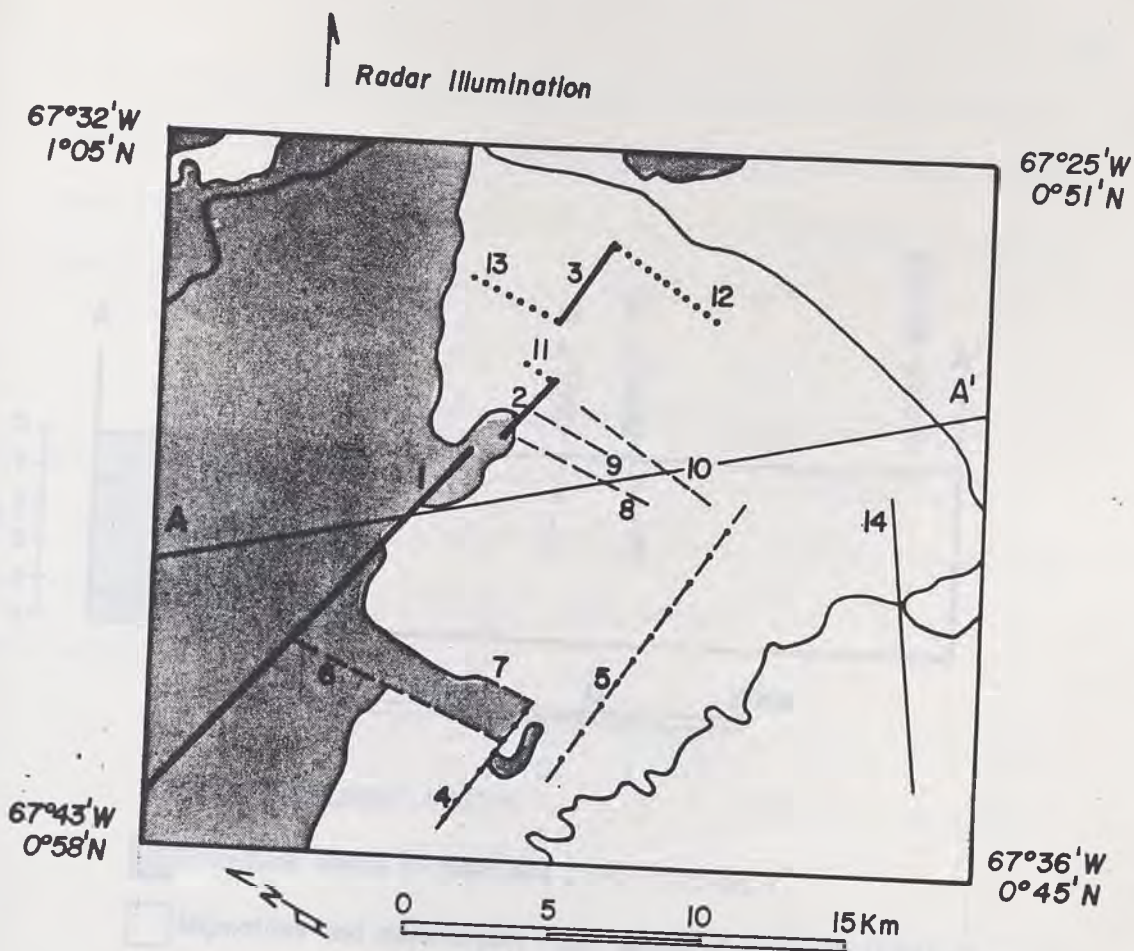
biotite, muscovite, quartz, and sillimanite (e.g., location 16) probably represent metasedimentary inclusions in the two-mica granitoids (as suggested by Dall'Agnol et al., 1987). In this research, the muscovite-bearing granitoids and gneisses corresponding to magnetization unit 2 were related to the  $1225 \pm 23$  m.y. anorogenic rocks of the Rio Negro-Juruena Province. The dike-like feature corresponding to magnetization unit 4 was considered to be an apophysis of such a middle Proterozoic intrusive body;

- (3) No radiometric age determinations are available for the granitoids devoid of muscovite (magnetization unit 3). However, they are clearly discordant to migmatites and metamorphic rocks devoid of muscovite (magnetization unit 2), whose age is  $1640 \pm 26$  m.y. In addition, they are intruded by a dike-like feature (magnetization unit 4), which was considered to be an apophysis of an anorogenic, muscovite-bearing granitic body ( $1225 \pm 23$  m.y.). These cross-cutting relationships suggest that the granitoids devoid of muscovite (magnetization unit 3) were emplaced sometime between 1.64 to 1.23 b.y. ago. A possible interpretation is that they are related to the anorogenic plutonism contemporaneous with the development of the Rondonian mobile belt. In this case, the age range of these rocks would be 1.45-1.25 b.y.



## DEVELOPMENT OF A RECONNAISSANCE GEOLOGIC MAP

The reconnaissance geologic map presented in this section (Figure 48) was derived through the integration of information derived from spaceborne radar (SIR-B) and aeromagnetic data. Lithologic descriptions and radiometric age determinations acquired by the RADAMBRASIL Project were also utilized. A schematic geologic cross section is shown on Figure 49. Geologic units shown in such a map are:



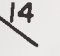
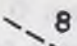
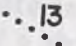
- (1) Migmatites and metamorphic rocks devoid of muscovite: they correspond to magnetization unit 2 and are characterized by intermediate brightness levels on the grey-scale magnetic image and by low to intermediate magnetization values on the terrace map ( $-0.00018 \text{ emu.cm}^{-3}$  to  $0.00090 \text{ emu.cm}^{-3}$ ). They are interpreted as part of the Rio Negro-Juruena magmatic arc. Rb-Sr whole-rock isochrons show an age of  $1640 \pm 26 \text{ m.y.}$  for field samples collected by the RADAMBRASIL Project within the limits of this unit;
- (2) Granitoids devoid of muscovite: they correspond to magnetization unit 3 and are characterized by very bright signatures on the grey-scale magnetic image and by high magnetization values (greater than  $0.00090 \text{ emu.cm}^{-3}$ ) on the terrace map. No radiometric age determinations are available for these rocks. Cross-cutting relationships suggest an age range of 1.45-1.25



**GEOLOGIC UNITS**

-  Granitoids devoid of muscovite (1.45-1.25 b.y.?)
-  Migmatites and metamorphic rocks devoid of muscovite (1.64 b.y.)

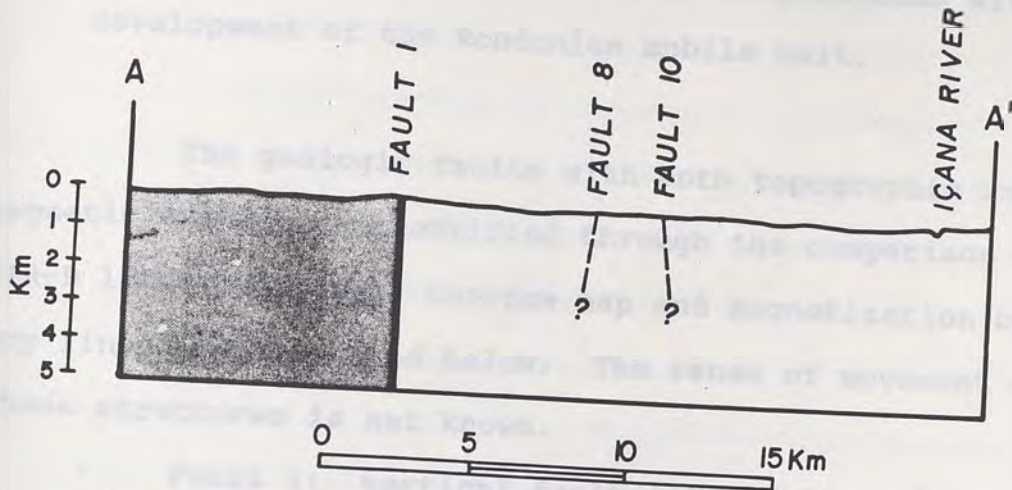
**GEOLOGIC STRUCTURES WITH BOTH TOPOGRAPHIC AND MAGNETIC EXPRESSION**

-  Vertical faults
-  Non-vertical faults
-  Magnetization boundary line aligned with SIR-B illumination direction
-  8 Faults cutting zones of abrupt lateral changes in magnetization
-  13 Faults without conspicuous magnetic expression

A-A' - Schematic geologic cross section (Figure 49).

Figure 48. Reconnaissance geologic map of crystalline basement terranes in the study area.





**GEOLOGIC UNITS**

- Granitoids devoid of muscovite (1.45 - 1.25 b.y.?)
- Migmatites and metamorphic rocks devoid of muscovite (1.64 b.y.)

**GEOLOGIC STRUCTURES WITH BOTH TOPOGRAPHIC AND MAGNETIC EXPRESSION**

- Vertical faults
- Faults cutting zones of abrupt lateral changes in magnetization

**COMMENT :** The 2-D magnetization distribution obtained with the terracing operator was expanded to fill a slab 5.0Km thick

Figure 49. Schematic geologic cross section (see Figure 48 for location).

b.y. This unit is tentatively related to the anorogenic plutonism that took place in the Rio Negro-Juruena Province. This event was contemporaneous with the development of the Rondonian mobile belt.

The geologic faults with both topographic and magnetic expression identified through the comparison of SIR-B linear features, terrace map and magnetization boundary lines are described below. The sense of movement of these structures is not known.

- Fault 1: vertical fault (SIR-B linear feature O coincident with magnetization boundary line MBL-1; see Figure 46);
- Fault 2: vertical fault (segment of magnetization boundary line MBL-2 that is aligned with SIR-B linear feature O);
- Fault 3: vertical fault (SIR-B linear feature P approximately coincident with a segment of magnetization boundary line MBL-2);
- Fault 4: non-vertical fault (SIR-B linear features F and G offset from magnetization boundary line MBL-3). It truncates the granitoids devoid of muscovite;
- Fault 5: non-vertical fault (SIR-B linear feature H subparallel to the course of the Piraiuara

River and significantly offset from magnetization boundary line MBL-3);

- Faults 6 and 7: faults cutting zones of abrupt lateral changes in magnetization (SIR-B linear feature C truncates magnetization boundary line MBL-4 and separates migmatites and metamorphic rocks from granitoids devoid of muscovite; SIR-B linear feature D is parallel to feature C and also separates these geologic units);
- Faults 8, 9, and 10: faults cutting zones of abrupt lateral changes in magnetization (SIR-B linear features Q<sub>4</sub>, Q<sub>5</sub>, and Q<sub>6</sub> truncate magnetization boundary lines MBL-3 and MBL-5);
- Faults 11, 12, and 13: faults without conspicuous magnetic expression (SIR-B linear features Q<sub>7</sub>, Q<sub>8</sub>, and Q<sub>10</sub> do not cross magnetization boundary line MBL-2);
- Fault 14: fault defined by a magnetization boundary line (MBL-6) controlling the location of a prominent meander of the Içana River. It was not identified as a SIR-B linear feature because it is parallel to the radar illumination direction (N57E).

Examination of Figure 48 demonstrates that E-W to WNW-ESE structures (faults 1, 2, 3, and 4) are truncating N-S

ones (faults 6, 7, 8, 9, 10, 11, 12, and 13). With the exception of fault 6, N-S structures do not affect granitoids devoid of muscovite (which are interpreted as being 1.45 to 1.25 b.y. old). Conversely, E-W to WNW-ESE structures clearly truncate this geologic unit (see faults 1, 2, and 4 on Figure 48). These cross-cutting relationships suggest that E-W to WNW-ESE structural trends were active sometime after 1.25 b.y. in the study area.

Comparison of Figures 8 and 48 show that there are no E-W to WNW-ESE faults mapped in the investigated site by the RADAMBRASIL Project. This demonstrates how strong is the effect of radar illumination azimuth in the detection of structural trends. Recall that RADAMBRASIL imagery was acquired by north-south aircraft flights using a westward looking direction. Therefore, N70E to N70W linear features were suppressed on the images, introducing a serious bias in the structural interpretation. This fact emphasizes the importance of using the complementary capabilities of digital aeromagnetic and spaceborne radar data in the geologic mapping of heavily-forested, deeply dissected crystalline regions such as the Guiana Shield.

## CHAPTER VII

## SUMMARY AND CONCLUSIONS

This final chapter presents a summary of the general experimental approach utilized in the research as well as the conclusions drawn from the analysis of spaceborne radar (SIR-B) and aeromagnetic data. Chapter 1 includes a list of the major science questions addressed by this study, to which the reader is referred.

## RESULTS OBTAINED WITH THE ANALYSIS OF SPACEBORNE RADAR (SIR-B) DATA

SIR-B image analysis was performed prior to the interpretation of aeromagnetic data and without any knowledge of the surface geology of the study area. Therefore, results obtained with such a remote sensing data set were not biased by any ancillary geologic or geophysical information.

Within the study area (23.5 km by 28.0 km), vegetation and water were the cover types that influenced the backscattered energy measured by the SIR-B antenna. The topography is predominantly flat as a result of extensive erosion, hence modulation of the radar backscatter by slope effects was negligible. Vegetation units were visually distinguished on the SIR-B image as groups of pixels with similar digital number (DN) values over extended areas. They were designated as dense vegetation, open vegetation, and flooded

vegetation. Water was included as an additional surface cover type.

Water constitutes smooth surfaces of mostly specular reflection. It consists of very low DN values on the SIR-B image. Backscatter from dense vegetation was considered to be predominantly diffuse. The relatively thinner and more sparse canopy of the open vegetation was assumed to produce lower levels of diffuse backscatter (and therefore lower DN levels than dense vegetation). Flooded vegetation presents the stronger backscatter in the investigated area. In fact, the SIR-B scene shows that brighter image tones outline the floodplains of some streams. This happens due to the presence of standing water below the canopy in the floodplains, which strongly reinforces radar return at L-band, HH polarization images. Such an effect is reported to occur in other heavily forested regions of the world (see review paper of Hess et al., 1990).

Data sets for semivariogram calculations were extracted from selected portions of the SIR-B image considered to be representative of water and specific vegetation units. Results obtained indicate that each cover type in the study area has a distinctive semivariogram. Consequently, the application of geostatistical classification techniques to this data set is feasible, since significantly distinct cover types presented unique semivariograms. The semivario-

gram textural classifier (STC) was then employed to discriminate and map flooded vegetation and water, which were considered the key cover types for the recognition of subtle topographic relief (up to 8.0 m) in the study area. The objective of such a procedure was to display landscape patterns indicative of subtle structural features in the crystalline terranes of the Guiana Shield.

Geomorphologic information derived from the STC-mapped landscape patterns was utilized in the definition of linear geomorphic features in the study area. The examination of the spatial distribution of flooded vegetation was particularly important in this analysis. In addition, tonal linear features were identified on the SIR-B image using a contrast stretching technique (trackball linear mapping; TLM). A final map was developed including both STC-discriminated and TLM-enhanced features. These linear features were compared with the information derived from aeromagnetic data. Areas of agreement were interpreted as geologic structures in the magnetic basement having topographic expression.

The most relevant aspects of the results obtained with the analysis of SIR-B data can be briefly described as follows:

- (1) the ability of the SIR-B system to remotely sense water beneath a forest canopy was crucial for the recognition of flooded vegetation in the study area. This cover

type is indicative of subtle differences in relief in the deeply dissected crystalline terranes of the Guiana Shield. Linearly arranged floodplains were interpreted as linear geomorphic features;

- (2) this study demonstrated that each cover type in the study area has a distinctive semivariogram signature. Such a result was the motivation for the development of the semivariogram textural classifier (MacDonald et al., 1990). Application of this technique to the Guiana Shield SIR-B data allowed vegetation units and water to be discriminated and mapped. The semivariogram textural classifier (STC) was also successfully employed for vegetation mapping using SIR-B data of the rainforest region of Borneo (Miranda et al., 1990). This indicates that the STC is a valuable tool for mapping rainforest environments using L-band, HH polarization spaceborne radars. In the first half of the 1990s, the Japanese Earth Resources Satellite (JERS-1) will include a radar system with characteristics similar to SIR-B. The analysis of such a global data set using the STC may provide the geologic community with important information about remote and perennially cloud-covered tropical regions of the world;
- (3) a simple contrast stretching technique referred to as



TLM (trackball linear mapping) was effective in enhancing tonal features on the SIR-B image for structural mapping purposes. Spatial radiometric patterns identified on the TLM-stretched SIR-B image can be described as (a) linear stream channels associated with flooded vegetation, and (b) dark linear features developed on an uniform background. Attempts to perform directional filtering in order to highlight tonal features with specific orientations were not as successful;

(4) examination of the map of SIR-B linear features allowed the establishment of cross-cutting relationships. They suggest that E-W to WNW-ESE structures are systematically truncating N-S ones in the study area. Such a geologic hypothesis was further tested when information derived from SIR-B and aeromagnetic data was integrated with pre-existing lithologic and radiometric data obtained in the field by the RADAMBRASIL Project (Pinheiro et al., 1976).

#### RESULTS OBTAINED WITH THE ANALYSIS OF AEROMAGNETIC DATA

The availability of digital aeromagnetic data in the Guiana Shield allowed the development of a variety of products that are useful to geologic mapping. These include grey-scale aeromagnetic images, horizontal-gradient and terrace-magnetization maps. The analysis of these products

was performed in a  $1^{\circ} \times 1^{\circ}$  area encompassing the study site.

The aeromagnetic survey was performed by a Brazilian contractor (ENCAL S/A Consultoria e Aerolevantamentos). Data reduction included diurnal variation correction, leveling of magnetic profiles, and removal of the International Geomagnetic Reference Field (IGRF). Gridded data obtained with the minimum-curvature interpolation technique (Webring, 1981) provided the database for digital data manipulation.

A grey-scale image depicted reduced-to-pole aeromagnetic data in 256 brightness levels ranging from black (the lowest value of 0) to white (the highest value of 255). It provided a qualitative representation of spatial variations in the magnetic properties of the upper levels of the crust. Examination of such a product enabled the identification of distinct magnetic patterns in the surroundings of the study area.

The computer program BOUNDARY (Blakely and Simpson, 1986) was used to produce a map showing the location of maximum values of the pseudogravity horizontal gradient. These maxima are designated as magnetization boundary lines and represent abrupt lateral changes in magnetization that are interpreted as steep structural or lithologic contacts (Cordell and Grauch, 1985).

A quantitative approach to resolve how magnetization domains are distributed in the study area was given by the

terracing operator (Cordell and McCafferty, 1989). This technique converted the smoothly-varying, pseudogravity transformed magnetic data into flat segments separated by vertical steps. These steps are approximately located over steep or near-vertical magnetization boundaries. The terraced data were rescaled to magnetization units in the cgs system ( $\text{emu}\cdot\text{cm}^{-3}$ ). The assumptions used in the production of the terrace-magnetization map are: (a) the total magnetization vector was considered to be parallel to the Earth's magnetic field (i.e., no attempt was made to account for remanent magnetization). This was done due to the lack of information concerning remanent magnetism in rocks of the study area; (b) the 2-D magnetization distribution obtained with the terracing operator was expanded to fill a thick slab. Magnetization values varied laterally across domains but not vertically within domain boundaries; (c) magnetic sources were assumed to be relatively close to the flat topographic surface. Therefore, the slab was considered to have a flat top at the terrain level. A slab thickness of 5.0 km was chosen for the model because this yielded the best forward calculated field together with plausible magnetization values; (d) contacts between magnetization domains were assumed to be vertical.

As expected, magnetization values on the terrace map showed good correlation with brightness levels on the grey-

scale aeromagnetic image. For example, areas with very bright signatures on the grey-scale image were always magnetization highs on the terrace map. The simultaneous analysis of these products was useful to establish the range of terrace-magnetization values corresponding to each of the magnetic patterns identified on the grey-scale image. Magnetization units were subsequently defined with the purpose of discriminating areas of very high and very low magnetization from an intermediate-level heterogeneous background.

The most relevant aspects of the results obtained with the analysis of aeromagnetic data can be briefly described as follows:

- (1) the automatic location of maximum horizontal gradients of pseudogravity-transformed aeromagnetic data (Blakely and Simpson, 1986) was an effective tool for the definition of magnetization boundaries in the Guiana Shield;
- (2) the terracing operator (Cordell and McCafferty, 1989) successfully delineated relatively large domains (up to 30 km in width) characterized by homogeneous magnetization properties and sharp boundaries. The terrace map, crudely proportional to a geologic map of magnetic rocks within the crystalline basement, was not obtained in a totally subjective fashion. Basic assumptions

were defined a priori, whereas data-processing procedures were objective and reproducible. The total magnetization range obtained in the Guiana Shield is approximately within one order of magnitude ( $-0.00090 \text{ emu.cm}^{-3}$  to  $0.00144 \text{ emu.cm}^{-3}$ ). A similarly narrow range has been observed in terrace maps from the U.S. Midcontinent region (McCafferty et al., 1989; Cordell and McCafferty, 1989) and from the Venezuelan part of the Guiana Shield (Wynn et al., 1990). Results in the study area are consistent with the hypothesis that variation in bulk magnetization at map scale among most geologic units is within one order of magnitude (as proposed by Cordell and McCafferty, 1989);

- (3) A map of magnetization units was developed based on the information derived from the grey-scale image and the terrace map. Such a map refers to a  $1^\circ \times 1^\circ$  area encompassing the study site. The range of magnetization corresponding to each of these units was defined as follows: (a) unit 1: values ranging from  $-0.00090 \text{ emu.cm}^{-3}$  to  $-0.00018 \text{ emu.cm}^{-3}$ ; (b) unit 2: values ranging from  $-0.00018 \text{ emu.cm}^{-3}$  to  $0.00090 \text{ emu.cm}^{-3}$ ; (c) unit 3: values greater than  $0.00090 \text{ emu.cm}^{-3}$ ; (d) unit 4: dike-like magnetic feature with magnetization values lower eastward ( $0.00018 \text{ emu.cm}^{-3}$ ) than westward ( $0.00072 \text{ emu.cm}^{-3}$ ); values as high as  $0.00108 \text{ emu.cm}^{-3}$

are found in the center of such a feature. These magnetization units were compared with the geologic data acquired in the field by the RADAMBRASIL Project. Broad terrane categories were delineated for the first time as a result of this comparison.

#### IMPLICATIONS FOR RECONNAISSANCE GEOLOGIC MAPPING IN THE GUIANA SHIELD AND CONTRIBUTION TO THE GEOLOGIC KNOWLEDGE OF NORTHWESTERN BRAZIL

A reconnaissance geologic map of the study area (23.5 km by 28.0 km) was produced involving two major steps: (a) comparison of SIR-B linear features with the terrace map and magnetization boundary lines map in order to identify magnetic basement structures having topographic expression; (b) comparison of terrace-magnetization units with geologic data acquired in the field by the RADAMBRASIL Project in order to delineate broad terrane categories.

Magnetic basement structures having topographic expression were recognized according to the following criteria: (a) SIR-B linear features coinciding with magnetization boundary lines were interpreted as the trace on the topographic surface of vertical geologic faults within the magnetic basement; (b) SIR-B linear features offset from magnetization boundary lines indicate that magnetic contacts are not well represented by vertical geologic structures. In such a case, SIR-B linear features were tentatively

interpreted as the surface expression of non-vertical geologic faults affecting the magnetic basement; (c) SIR-B linear features truncating magnetization boundary lines were interpreted as the surface expression of geologic faults cutting zones of abrupt lateral changes in magnetization. The sense of movement of these structures is not known.

Broad terrane categories of differing magnetization-intensity levels were defined in the  $1^{\circ} \times 1^{\circ}$  region embracing the investigated site. Areas characterized by very dark signature on the grey-scale image and by very low values on the terrace map (magnetization unit 1) correspond to muscovite-bearing granitoids and gneisses. Areas characterized by intermediate brightness levels on the grey-scale image and by low to intermediate values on the terrace map (magnetization unit 2) are related to migmatites and metamorphic rocks devoid of muscovite. Areas characterized by very bright signatures on the grey-scale image and by high values on the terrace map (magnetization unit 3) correspond to granitoids devoid of muscovite. The dike-like magnetic feature expressed on both the grey-scale image and terrace map (magnetization unit 4) was interpreted as an intrusive body cross-cutting granitoids devoid of muscovite (magnetization unit 3). Such a feature may be an apophysis of a larger intrusive body represented by muscovite-bearing granitoids (magnetization unit 1).

The area of study is characterized by the occurrence of migmatites and metamorphic rocks devoid of muscovite (magnetization unit 2) and granitoids devoid of muscovite (magnetization unit 3). These are the terrane categories included in the reconnaissance geologic map obtained through the integration of spaceborne radar (SIR-B) and aeromagnetic information. Such a geologic framework was established taking into account lithologic descriptions performed in the field by the RADAMBRASIL Project.

The most relevant geologic results achieved in the study area are described below:

- (1) middle Proterozoic crystalline rocks of the Guianense Complex (Pinheiro et al., 1976) were individually recognized as distinct geologic units in the investigated site for the first time. Migmatites and metamorphic rocks devoid of muscovite correspond to magnetization unit 2 and are characterized by intermediate brightness levels on the grey scale magnetic image and by low to intermediate magnetization values on the terrace map ( $-0.00018 \text{ emu.cm}^{-3}$  to  $0.00090 \text{ emu.cm}^{-3}$ ). They are interpreted as part of the Rio Negro-Juruena magmatic arc (1.75-1.50 b.y.; Tassinari, 1981). Rb-Sr whole rock isochrons show an age of  $1640 \pm 26 \text{ m.y.}$  for field samples collected by the RADAMBRASIL Project within the limits of this unit (Dall'Agnol and Abreu,



1976). Granitoids devoid of muscovite correspond to magnetization unit 3 and are characterized by very bright signatures on the grey-scale magnetic image and by high magnetization values (greater than  $0.00090 \text{ emu.cm}^{-3}$ ) on the terrace map. No radiometric age determinations are available for these rocks. Cross-cutting relationships suggest an age of 1.45-1.25 b.y. This unit is tentatively related to the anorogenic plutonism that took place in the Rio Negro-Juruena Province. According to Tassinari (1981), this event was contemporaneous with the development of the Rondonian mobile belt;

- (2) Geologic faults with both topographic and magnetic expression were identified through the comparison of SIR-B linear features, terrace map, and magnetization boundary lines. The sense of movement of these structures is not known. However, it was possible to demonstrate that E-W to WNW-ESE structures are truncating N-S ones. With one exception, N-S structures do not affect granitoids devoid of muscovite (which are interpreted as being 1.45 to 1.25 b.y. old). Conversely, E-W to WNW-ESE structures clearly truncate this geologic unit. These cross-cutting relationships suggest that E-W to WNW-ESE structural trends were active sometime after 1.25 b.y. in the study area;

- (3) this study showed that the integrated analysis of digital aeromagnetic and spaceborne radar data facilitates the development of geologic information in heavily forested and deeply dissected terranes of Precambrian age. The availability of global spaceborne radar coverage in the first half of the 1990s and the large number of already existing digital aeromagnetic surveys in northwestern Brazil indicate that this approach can be potentially useful for reconnaissance geologic mapping elsewhere in the Guiana Shield.

## REFERENCES

- Aymard, W.H., and J.A. MacDonald, 1990, Spectral and textural classification of GER 63 channel data for vegetation cover mapping in northeastern Minnesota: Proceedings of the IGARSS'90 Conference, Washington, D.C., p.1617.
- Barnes, J.W., 1981, Basic geological mapping: Milton Keynes (Buckinghamshire): Open University Press, New York: Halsted Press, 112p.
- Bates, R.L., and J.A. Jackson, 1987, Glossary of geology: American Geological Institute, Alexandria, Virginia, 788p.
- Blakely, R.J., and R.W. Simpson, 1986, Locating edges of source bodies from magnetic or gravity anomalies: Geophysics, v.51, no.7, p.1494-1498.
- Branch of Geophysics, 1989, Potential-field geophysical programs for VAX-7xx computers: U.S. Geol. Surv. open-file rep. 89-115, 21p.
- Carr, J.R., and D.E. Myers, 1984, Application of the theory of regionalized variables to the spatial analysis of Landsat data: I.E.E.E. Proceedings of the PECORA 9 Spatial Information Technologies for Remote Sensing Today and Tomorrow, p.55-61.
- Cimino, J.B., B. Holt, and A.H. Richardson, 1988, The Shuttle Imaging Radar B (SIR-B) experiment report: California Institute of Technology, JPL Publication 88-2, 218 p.
- Cordani, U.G., and B.B. Brito Neves, 1982, The geologic evolution of South America during the Archean and early Proterozoic: Rev. Bras. Geoc., v.12, p.78-88.
- Cordell, L., 1985, A stripping filter for potential-field data: Society of Exploration Geophysicists, Abstracts Annual Meeting, p.217.
- Cordell, L., and V.J.S. Grauch, 1985, Mapping basement magnetization zones from aeromagnetic data in the San Juan Basin, New Mexico. In: Hinze, W.J. ed., The utility of regional gravity and magnetic anomaly maps: Soc. Expl. Geophys., p.181-197.

- Cordell, L., and D.H. Knepper, 1987, Aeromagnetic images: fresh insight to the buried basement, Rolla quadrangle, southeast Missouri: *Geophysics*, v.52, no.2, p.218-231.
- Cordell, L., and A.E. McCafferty, 1989, A terracing operator for physical property mapping with potential field data: *Geophysics*, v.54, no.5, p.621-634.
- Correa, A.C., 1979, Geologic mapping in jungle terrain - a challenge to side-looking radar: paper presented at the NASA/JPL Radar Geology Workshop, Snowmass, Colorado, July 16-20, 1979.
- Curran, P.J., 1988, The semivariogram in remote sensing: an introduction: *Remote Sensing of Environment*, v.24, p.493-507.
- Curran, P.J., and J.L. Dungan, 1989, Estimation of signal-to-noise: a new procedure applied to AVIRIS data: *I.E.E.E. Transactions on Geoscience and Remote Sensing*, v.27, no.5, p.620-628.
- Dall'Agnol, R., and A.S. Abreu, 1976, Características petrográficas e petrológicas do Complexo Guianense na Folha NA.19 Pico da Neblina. *Anais XXIX Congr. Bras. Geol.*, Ouro Preto, Soc. Bras. Geol., v.2, p.321-350.
- Dall'Agnol, R., J.S. Bettencourt, X.S. Jorge-João, H. Medeiros, H.T. Costi, and M.J.B. Macambira, 1987, Granitogenesis in the northern Brazilian region: a review: *Rev. Bras. Geoc.*, v.17, no.4, p.382-403.
- Dobrin, M.B., and C.H. Savit, 1988, *Introduction to geophysical prospecting*: McGraw-Hill, Inc., New York, 867p.
- Elachi, C., J.B. Cimino, and M. Settle, 1986, Overview of the Shuttle Imaging Radar-B preliminary scientific results: *Science*, v.232, p.1511-1516.
- Engheta, N., and C. Elachi, 1982, Radar scattering from a diffuse vegetation layer over a smooth surface: *I.E.E.E. Transactions on Geoscience and Remote Sensing*, v.GE-20, no.2, p.212-216.
- Ford, J.P., 1980, Seasat orbital radar imagery for geologic mapping: Tennessee-Kentucky-Virginia: *Amer. Assoc. Petroleum Geologists Bulletin*, v.64, p.2064-2094.

- Ford, J.P., R.G. Blom, M.L. Bryan, M.I. Daily, T.H. Dixon, C. Elachi, and E.C. Xenos, 1980, Seasat views North America, the Caribbean, and western Europe with imaging radar: California Institute of Technology, JPL Publication 80-67, 141p.
- Ford, J.P., J.B. Cimino, and C. Elachi, 1983, Space Shuttle Columbia views the world with imaging radar: the SIR-A experiment: California Institute of Technology, JPL Publication 82-95, 179p.
- Ford, J.P., and R. da Cunha, 1985, Shuttle radar images for geologic mapping in tropical rainforest: Proceedings of the Environmental Research Institute of Michigan, 4th Thematic Conference: Remote Sensing for Exploration Geology, San Francisco, California, p.669-676.
- Ford, J.P., and F.F. Sabins, Jr., 1986, Satellite radars for geologic mapping in tropical regions: Proceedings of the Environmental Research Institute of Michigan, 5th Thematic Conference: Remote Sensing for Exploration Geology, Reno, Nevada, p.307-316.
- Ford, J.P., J.B. Cimino, B. Holt, and M.R. Ruzek, 1986, Shuttle imaging radar views the Earth from Challenger: the SIR-B experiment: California Institute of Technology, JPL Publication 86-10, 135p.
- Ford, J.P., and D.S. Casey, 1988, Shuttle radar mapping with diverse incidence angles in the rainforest of Borneo: International Journal of Remote Sensing, v.9, no.5, p.927-943.
- Fu, L.L., and B. Holt, 1982, Seasat views oceans and sea ice with Synthetic Aperture Radar: California Institute of Technology, JPL Publication 81-120, 200p.
- Glass, C.E., J.R. Carr, H.M. Yang, and D.E. Myers, 1988, Application of spatial statistics to analyzing multiple remote sensing data sets: Geotechnical Applications of Remote Sensing Data and Remote Data Transmission, ASTM STP 967, A.I. Johnston and C.B. Peterson, Eds., American Society for Testing and Materials, Philadelphia, p.138-150.
- Grauch, V.J.S., and L. Cordell, 1987, Limitations of determining density or magnetic boundaries from the horizontal gradient of gravity or pseudogravity data: Geophysics, v.52, no.1, p.118-121.

- Hess, L.L., J.M. Melack, and D.S. Simonett, 1990, Radar detection of flooding beneath the forest canopy: a review: *International Journal of Remote Sensing*, v.11, no.7, p.1313-1325.
- Hildenbrand, J.D., R.W. Pieren, and J. Lourenço, 1987, Projeto Extremo Noroeste do Brasil - Levantamento Aeromagnético e Aerogamaespectrométrico: ENCAL S/A Consultoria e Aerolevantamentos, Relatório final de aquisição de dados, 52p.
- Hildenbrand, T.G., 1983, FFTFIL: A filtering program based on two-dimensional Fourier analysis: U.S. Geol. Surv. open-file rep. 83-237, 29p.
- Hildenbrand, T.G., R.P. Kucks, and R.E. Sweeney, 1983, Digital colored magnetic-anomaly map of the Basin and Range Province: U.S. Geol. Surv. open-file rep. 83-189, 12p.
- Hoffer, R., D.F. Lozano-Garcia, D.D. Gillespie, P.W. Mueller, and M.J. Ruzek, 1986, Analysis of multiple incidence angle SIR-B data for determining forest stand characteristics: 2nd Space-Borne Imaging Radar Symposium, Pasadena, CA, California Institute of Technology, JPL Publication 86-26, p.159-164.
- Imhoff, M.L., M. Story, C. Vermillion, F. Khan, and F. Polcyn, 1986, Forest canopy characterization and vegetation penetration assessment with spaceborne radar: I.E.E.E. Transactions on Geoscience and Remote Sensing, v.GE-24, no.4, p.535-542.
- Imhoff, M.L., and D.B. Gesch, 1990, The derivation of a sub-canopy digital terrain model of a flooded forest using synthetic aperture radar: *Photogrammetric Engineering and Remote Sensing*, v.56, no.8, p.1155-1162.
- Jordan, C.F., 1985, Soils of the Amazon rainforest. In: Prance, G.T. and T.E. Lovejoy, eds., *Key environments: Amazonia*, Pergamon Press, U.K., p.83-94.
- Journel, A.G., and C.J. Huijbregts, 1978, *Mining geostatistics*: Academic Press, London, 600p.
- Jupp, D.L.B., A.H. Strahler, and C.E. Woodcock, 1988, Autocorrelation and regularization in digital images: I. Basic theory: I.E.E.E. Transactions on Geoscience and Remote Sensing, v.26, no.4, p.463-473.

- Jupp, D.L.B., A.H. Strahler, and C.E. Woodcock, 1989, Autocorrelation and regularization in digital images: II. Simple image models: I.E.E.E. Transactions on Geoscience and Remote Sensing, v.27, no.3, p.247-258.
- Kearey, P., and M. Brooks, 1984, An introduction to geophysical exploration: Blackwell Scientific Publications, Oxford, 296p.
- Koppen, W., 1948, Climatologia; con un estudio de los climas de la tierra: version de Pedro H. Hendrichs, Mexico, Fondo de Cultura Economica, 478p.
- Krohn, M.D., N.M. Milton, and D.B. Segal, 1983, Seasat Synthetic Aperture Radar (SAR) response to lowland vegetation types in eastern Maryland and Virginia: Journal of Geophysical Research, v.88, no.C3, p.1937-1952.
- Lowman, P.D., Jr., J. Harris, P.M. Masuoka, V.H. Singhroy, and V.R. Slaney, 1987, Shuttle Imaging Radar (SIR-B) investigations of the Canadian Shield: initial report: I.E.E.E. Transactions on Geoscience and Remote Sensing, v.GE-25, no.1, p.55-66.
- MacDonald, H.C., W.P. Waite, and J.S. Demarcke, 1980, Use of Seasat satellite radar imagery for the detection of standing water beneath forest vegetation: Proceedings of ASP Technical Papers, American Society of Photogrammetry and American Congress of Surveying and Mapping Fall Technical Meeting, Niagara Falls, NY, RS-3-B-1-12.
- MacDonald, J.A., and J.R. Carr, 1989, Applications of geostatistics to image analysis: Proceedings of the IGARSS'89 Conference, Vancouver, B.C., p.2409-2411.
- MacDonald, J.A., F.P. Miranda, and J.R. Carr, 1990, Textural image classification using variograms: paper presented at SPIE's 1990 Technical Symposium on Optical Engineering and Photonics in Aerospace Sensing, 16-20 April 1990, Orlando, Florida.
- Masuoka, P.M., J. Harris, P.D. Lowman, Jr., and H.W. Blodget, 1988, Digital processing of orbital radar data to enhance geologic structure: examples from the Canadian Shield: Photogrammetric Engineering and Remote Sensing, v.54, no.5, p.621-632.
- Matheron, G., 1963, Principles of geostatistics: Economic Geology, v.58, p.1246-1266.

- McCafferty, A.E., L. Cordell, and R.E. Bracken, 1989, Geophysical maps and interpretation of basement terrane in the Harrison 1° x 2° quadrangle, Missouri and Arkansas: U.S. Geol. Surv. miscellaneous field studies map 1994-B, scale: 1:500,000.
- McCafferty, A.E., 1991, Aeromagnetic map and terrace-magnetization map centered on the Idaho batholith and Challis volcanic field and vicinities, Lat. 42° - 47° N., Long. 110° - 118° W.: U.S. Geol. Surv. geophysical investigation map GP/994, scale: 1:1,000,000, 17p.
- Miranda, F.P., and J.A. MacDonald, 1989, A variogram study of SIR-B data in the Guiana Shield, Brazil: Proceedings of the Image Processing '89 Conference, American Society for Photogrammetry and Remote Sensing, Sparks, Nevada, p.66-77.
- Miranda, F.P., J.A. MacDonald, and J.R. Carr, 1990, Application of the semivariogram textural classifier (STC) to SIR-B data of Borneo: paper presented at the Airborne Geoscience Workshop: AIRSAR, 7-8 June 1990, Jet Propulsion Laboratory, Pasadena, California, in press.
- Mueller, P.W., and R.N. Hoffer, 1989, Low-pass spatial filtering of satellite radar data: Photogrammetric Engineering and Remote Sensing, v.55, no.6, p.887-895.
- NASA, 1987, SAR, Synthetic Aperture Radar, Earth Observing System: Instrument Panel Report, v.IIf., 233p.
- Nascimento, D.A., and M. Prates, 1976, Geomorfologia. In: MME Projeto RADAMBRASIL, Levantamento de Recursos Naturais, Folha NA.19 - Pico da Neblina, DNPM, Rio de Janeiro, v.11, p.141-189.
- Ormsby, J.P., B.J. Blanchard, and A.J. Blanchard, 1985, Detection of lowland flooding using active microwave systems: Photogrammetric Engineering and Remote Sensing, v.51, no.3, p.317-328.
- Phillips, J.D., 1990, TERRACE: A terracing procedure for gridded data, with FORTRAN programs, and VAX command procedure and Unix C-shell implementations: U.S. Geol. Surv. open-file rep., in press.



- Pinheiro, S.S., P.E.C.A. Fernandes, E.R. Pereira, E.G. Vasconcelos, A.C. Pinto, R.M.G. Montalvão, R.S. Issler, R. Dall'Agnol, W. Teixeira, and C.A.C. Fernandes, 1976, Geologia. In: MME Projeto RADAMBRASIL, Levantamento de Recursos Naturais, Folha NA.19 - Pico da Neblina, DNPM, Rio de Janeiro, v.11, p.17-137.
- Place, J.L., 1985, Mapping of forest wetland: use of Seasat radar images to complement conventional sources: Professional Geographer, v.37, no.4, p.463-469.
- Ramstein, G., and M. Raffy, 1989, Analysis of the structure of radiometric remotely-sensed images: International Journal of Remote Sensing, v.10, no.6, p.1049-1073.
- Richards, J.A., P.W. Woodgate, and A.K. Skidmore, 1987, An explanation of enhanced radar backscattering from flooded forests: International Journal of Remote Sensing, v.8, no.7, p.1093-1100.
- Roessing, H.M., J.P. Neves Filho, R.N. Peres, and A.M.R. da Costa, 1976, Pedologia - Levantamento Exploratório de Solos. In: MME Projeto RADAMBRASIL, Levantamento de Recursos Naturais, Folha NA.19 - Pico da Neblina, DNPM, Rio de Janeiro, v.11, p.201-249.
- Rubin, T., 1989, Analysis of radar image texture with variograms and other simplified descriptors: Proceedings of the Image Processing'89 Conference, American Society for Photogrammetry and Remote Sensing, Sparks, Nevada, p.185-195.
- Sabins, F.F., Jr., 1983, Geologic interpretation of Space Shuttle radar images of Indonesia: Amer. Assoc. Petroleum Geologists Bulletin, v.67, p.2076-2099.
- Sabins, F.F., Jr., 1987, Remote sensing: principles and interpretation: W. H. Freeman and Company, New York, N.Y., 449p.
- Sieber, A.J., 1985, Statistical analysis of SAR images: International Journal of Remote Sensing, v.6, no.9, p.1555-1572.
- Silva, F.C.F., A.G. Ribeiro, R.R. dos Santos, H.C. Ferreira, and W. N. da Fonseca, 1976, Vegetação. In: MME Projeto RADAMBRASIL, Levantamento de Recursos Naturais, Folha NA.19 - Pico da Neblina, DNPM, Rio de Janeiro, v.11, p.271-344.

- Skolnik, M.I., 1980, Introduction to radar systems: McGraw-Hill Book Co., New York, 581p.
- Tassinari, C.C.G., 1981, A evolução geotectônica da Província Rio Negro-Juruena na região amazônica (M.Sc. thesis): São Paulo, SP, Inst. Geoc. Univ. São Paulo, 101 p.
- Teixeira, W., C.C.G. Tassinari, U.G. Cordani, and K. Kawashita, 1989, A review of the geochronology of the Amazonian Craton: tectonic implications: *Precambrian Res.*, v.42, p.213-227.
- Telford, W.M., L.P. Geldart, R.E. Sheriff, and D.A. Keys, 1986, Applied geophysics: Cambridge University Press, Cambridge, 860p.
- VAX-IDIMS Functional Guide, 1987, ESL Incorporated, Sunnyvale, California.
- Waite, W.P., H.C. MacDonald, V.H. Kaupp, and J.S. Demarcke, 1981, Wetland mapping with imaging radar: I.E.E.E. - IGARSS'81, Washington, D.C., Digest, v.2, p.794-799.
- Wald, L., 1989, Some examples of the use of structure functions in the analysis of satellite images of the ocean: *Photogrammetric Engineering and Remote Sensing*, v.55, no.10, p.1487-1490.
- Webring, M.W., 1981, MINC: A gridding program based on minimum curvature: U.S. Geol. Surv. open-file rep. 81-1224, 11p.
- Woodcock, C.E., A.H. Strahler, and D.L.B. Jupp, 1988a, The use of variograms in remote sensing: I. Scene models and simulated images: *Remote Sensing of Environment*, v.25, p.323-348.
- Woodcock, C.E., A.H. Strahler, and D.L.B. Jupp, 1988b, The use of variograms in remote sensing: II. Real digital images: *Remote Sensing of Environment*, v.25, p.349-379.
- Wynn, J.C., A.E. McCafferty, and E. Salazar, 1989, Geologic information derived from digital aeromagnetic data: Proceedings Volume, Simposia Cogeodata Sud America, Mtg April, 1989 Caracas, 18p.